Dissertation
for
Addressing Spectrum Congestion by Spectrally-Cooperative Radar Design

By

Peng Seng Tan

Submitted to the Department of Electrical Engineering & Computer Science and the
Graduate Faculty of the University of Kansas
in partial fulfillment of the requirements for the degree of
Doctor of Philosophy

Committee members

Dr. James Stiles, Chairperson

Dr. Shannon Blunt

Dr. Christopher Allen

Dr. Lingjia Liu

Dr. Tyrone Duncan

Date defended: _____

The Dissertation Committee for Peng Seng Tan certifies
that this is the approved version of the following dissertation :

Dissertation
for
Addressing Spectrum Congestion by Spectrally-Cooperative Radar Design

Dr. James Stiles, Chairperson

Date approved: _____

Abstract

This dissertation attempts to address a significant challenge that is encountered by the users of the Radio Frequency (RF) Spectrum in recent years. The challenge arises due to the need for greater RF spectrum by wireless communication industries such as mobile telephony, cable/satellite and wireless internet as a result of growing consumer base and demands. As such, it has led to the issue of spectrum congestion as radar systems have traditionally maintain the largest share of the RF spectrum. To resolve the spectrum congestion problem, it has become even necessary for users from both radar and communication systems to coexist within a finite spectrum allocation. However, this then leads to other problems such as the increased likelihood of mutual interference experienced by all systems that are coexisting within the finite spectrum.. In order to address this challenge, the dissertation will seek to resolve it via a two-step approach that are described as follows.

For the first step of this approach, it will present a structured and meticulous approach to design a sparse spectrum allocation optimization scheme that will lead to the release of valuable spectrum previously allocated to radar applications for reallocation to other players such as the wireless video-on-demand and telecommunication industries while maintaining the range resolution performance of these radar applications. This sparse bandwidth allocation scheme is implemented using an optimization process utilizing the Marginal Fisher information (MFI) measure as the main metric for optimization. Although the MFI approach belongs to the class of greedy optimization methods that cannot guarantee global convergence, the results obtained indicated that this approrach is able to produce a locally optimal solution.

For the second step of this approach, it will present on the design of a spectral efficient waveform that can be used to ensure that the allocated spectrum limits will not be violated due to poor spectral emission containment. The design concept of this waveform is based on the joint implementation of the first and higher orders of the Poly-phase coded Frequency Modulated (PCFM) waveform that expands previous research on first order PCFM waveform. As any waveform generated using the PCFM framework possesses good spectral containment and is amenable to high power transmit operations such as radar due to its constant modulus property, thus the combined-orders of PCFM waveform is a very suitable candidate that can be used in conjunction with the sparse bandwidth allocation scheme in the first step for any radar application such that the waveform will further mitigate the issue of interference experienced by other users coexisting within the same band.

Acknowledgements

I will like to thank my advisor, Prof. Stiles for his invaluable guidance in my research in Sparse Array design as well as its close analogy to the domain of Compressive Sensing. I will also like to thank him for his insights and guidance in the domain of Adaptive Filtering Theory, especially on Bayesian estimation. I will also like to thank my co-advisor, Prof. Blunt for introducing me to the amazing world of Radar Waveform Design as well as applications of Adaptive Signal Processing and Optimization principles. Over the course of my PhD research, both of them have trained me tirelessly on having the proper approach and mentality to tackle any research problem as well as presenting the findings in a coherent and unambiguous manner. Coming from a background of working in the industry for more than 16 years, having a good research mentality is especially important for me when there are so many more things to learn from in these domains.

Next, I will like to thank Prof. Allen, Prof. Liu and Prof. Duncan who have agreed to be in my committee. Now, having taking two graduate level courses under Prof. Liu and auditing an advanced Radar Systems course under Prof. Allen has exposed myself to the field of Wireless Communications and Advanced Radar Signal Processing techniques which helped me to be a more knowledgeable person in these domains of research. I am thankful to both of them for their enthusiasm and helpful advice shown to me in these classes. I will also like to thank Prof. Duncan for always providing a friendly face and kind words to me whenever I met him in Nichols

Hall. I also enjoyed our small exchange and greetings in Chinese with him during these occasions.

Thirdly, I will also like to thank my wife and children for supporting me throughout the course of my PhD degree pursuit. This is especially after I have spent so little time with them during these 6 years, being in KU in the day most of the times and missing many important family events that meant a lot to them. At the same time, coming to America with me has required my family to have very large adjustments to their daily lives which they have taken in their stride.

Fourthly, I will like to thank my fellow EECS graduate students, Patrick McCormick, John Jakabosky, Lumumba Harnett, Jonathan Owen, Gerald Brandon Ravenscroft, Eli Symm, Rubayet Shafin, Siddharth Gangadhar, Yuanwei Wu, Lei Yang, Sushil Bharati, Justin Dawson, Paul Kline and Brad Torrence for their conversations and companionship, be it related to my PhD research work, Teaching Assistant responsibilities or in the daily routines or cultures of our lives. They have certainly enhanced my overall experience here in America.

Finally, I will like to thank GOD who has given me the ability to be able to acquire new skills and knowledge as well as enjoying the process of learning and the satisfaction of obtaining the end results. Without HIM, I will not even be in America to pursue my dream of obtaining the highest formal level of education, a PhD degree, in this temporal time span that I have with my life.

Contents

List of Figures

List of Tables

Chapter 1

Introduction

1.1 Motivation

The ever increasing demand of Radio Frequency (RF) spectrum for wireless communication applications has become a regular occurrence in the last decade. The main driver behind the push for more efficient spectrum bandwidth allocation and usage has been the boom of commercial wireless video/audio industries in conjunction with the huge market demand for smart mobile devices. Nowadays, the millennial and post-millennial generations are spending much more time and energy on acccesing entertainment applications on mobile devices than their predecessors such as having conversations on FaceTime and Skype for instances, as well as sending video clips to one other using popular applications like Snapchat and Instagram. Thus, this has resulted in the push towards several major research directions, such as investigation of the performance degradation between radar and wireless communications when both systems are coexisting in operations ([1]-[2]). In addition, there are efforts to develop sophisticated radar waveforms that are either spectrally well contained or efficient ([3]-[4]), or able to support joint radar/wireless communications systems operating within the same spectrum band, i.e. under a spectrum sharing mode of operation. In fact, the focus on Spectrum Efficiency has in the recent years become a very important feature in defining new wireless mobile communication protocols in 5th Generation (5G) mobile

networks.

Traditionally, large chunks of the RF spectrum in the region from UHF band starting at 300 MHz and up to 100 GHz are dominated by government and military based radar applications from terrestrial, airborne to even space-borne remote sensing operations. However, this preferential status is increasing being challenge by technological advances and developments made in telecommunication and mobile industries around the world. With the advent of wireless internet such as IEEE 802.11a\b\g\n\ac and 802.11ah, complex cellular network protocols like 5G networks cum the increasing popularity of accessing Demand on video or social media platforms like Facebook on smart mobile devices, the dominant status enjoyed by the radar community in spectrum allocation is a luxury that can no longer be enjoyed by just the radar community. In recent years, due to the rise of networking technologies associated with the Internet of Things (IOT), new demands on spectrum allocation have also been placed extensively by the construction, manufacturing, agricultural and consumer electronics industries.

Currently, for any development of new wireless communication protocols, being spectral efficient is almost one of the important criteria. Also, a general definition of Spectrum Efficiency picked out from the internet that is readily applicable to cellular networks is " Optimized use of spectrum or bandwidth so that maximum amount of data can be transmitted with the fewest transmission errors." Now, in the context of radar, one definition of the term Spectrum Efficiency can be described as the goal of using the minimal/optimal bandwidth budget to achieve a performance result that is comparable with minimal degradation as compared to using a original larger bandwidth budget. This will then free up the unused spectrum from the original budget to be taken up by other users or applications. At the same time, this definition of Spectrum Efficiency is aligned with the efforts to enable Spectrum Sharing between radar and wireless communication systems by various government/commercial bodies around the world.

Next, a second definition of Spectrum Efficiency in radar context can be the goal of containing

the RF emissions from the radar antenna strictly within its allocated bandwidth so that there will not be stray emissions that leaked out into the spectrum bands of other applications as interference signals. As the transmission power of an active radar application is typically much stronger compared to that of wireless communication, thus containing the radar emissions within its bandwidth will be of utmost importance.

In the next two sections of this Chapter, a brief description of the two-step approach that is adopted in this dissertation will be provided. The two-step approach, which for simplicity has been named as Part 1 and Part 2 of this dissertation, will aim to address the two definitions of Spectrum Efficiency as mentioned in the paragraph above in the context of radar. The detailed description of each part will be greatly expanded in the subsequent Chapters. Also, the final section of this Chapter will provide the overview for the remaining Chapters in the dissertation.

1.2 Proposed Approach

A Defense Advanced research Projects Agency (DARPA) program known as Shared Spectrum Access for Radar and Communications (SSPARC) was initiated in 2014 to address the issue of spectrum congestion between radar and wireless communication below the 6 GHz frequency band, especially at the L band and S band operating frequencies. The primary objective of SSPARC is to enable bandwidth sharing in two ways: between military radars and communications, and between military radars and commercial communications. Last year, the program has moved into the Phase 2 Stage and DARPA has awarded the company Leidos a contract worth 7.9 millons USD to focus the feasibility study on sharing in the S-band which is in the range of 2 GHz to 4 GHz.

In the DARPA program and all other government/commercial initiatives such as the recent explosion of the technologies behind the Internet of Things (IOT) that extends the spectrum demands to the millimter wave regions, the main technical efforts to address the issues of band congestion due to coexistence of radar and wireless communication systems are concentrated into 3 category

approaches [5], namely:

- Time and Spatial domain multiplexing between radar and wireless communication operations through cooperative measures cum deployment of advanced spectrum sensing algorithm by at least one party [Category 1]

- Robust radar system that encompass designs (predominantly waveform) that will mitigate the interference to/from the communication party when both systems are utilizing within or nearby spectral band [Category 2]

- Joint design of both radar and wireless communication systems to cooperatively mitigate the amount of interference to each other. This objective is achieved via the use of MIMO architecture cum specialized transmit waveforms such as multi-modal OFDM waveform design for both radar and wireless communication [Category 3]

With this broad categorization of the approaches, Part 1 of this dissertation that is can loosely be grouped under the 2nd category in which an optimal spectrum allocation scheme is applied to the original allocated bandwidth of a radar application such that the unused portion after optimization is released to another application such as a communication system. Similarly, Part 2 of the dissertation can also be grouped under the 2nd category as well. In this case, the design of a transmit radar waveform with good spectral containment will help to reduce the interference to communication users in the nearby spectral bands.

1.2.1 Sparse Spectrum Allocation

In any radar application, an increase of available spectral bandwidth will translate into an improvement in the radar's resolution of two separate entities, regardless of whether it is operating in the range or Doppler domain. Corresponding, a decrease in the available bandwidth will translate to a degradation of the radar's resolution performance. Now, when considering the possibility of spectrum sharing between radar and communication systems, one suggestion is to trade-off radar

resolution with lower bandwidth based on the target scattering characteristics such that the remaining bandwidth can be released to the communication system, i.e. in the case of a multi-modal radar. This approach will be feasible if the target scattering characteristics are indeed changing significantly over the areas of interest being surveyed by the radar.

Consider a contiguous RF spectrum band bounded by a lower frequency f_1 and an upper frequency f_2. The picture that often comes to mind is that of contiguous frequency utilization for the entire band defined by $(f_2 - f_1)$. However, we can also view the spectrum as consisting of many distinct spectral lines as in a line spectrum commonly represented in optical spectroscopy. Using this analogy, the contiguous spectrum band can be defined by the generic expression:

$$s(w) = \sum_{n=1}^{N} s_n \delta(w - w_n) \tag{1.1}$$

In the above expression, $s(w)$ represents the original contiguous spectrum that has been defined to consist of a summation of N spectral lines with each spectral line defined by a Dirac-Delta function $\delta(w)$ offset at the frequency location w_n and weighted by the value s_n. When applied to a pulsed radar system transmitting at the Pulse Repetition Frequency PRF , the expression will be altered to that of:

$$s(w) = \sum_{n=1}^{N} s_n \delta(w - nw_{PRF}) \tag{1.2}$$

By examining the above equation, it can be seen that in a pulsed radar system, not all the frequency contents are utilized in the given contiguous spectral band as each spectral line is separated by the PRF interval. As such, there arises the question of whether the radar needs the full contiguous spectrum in order to achieve the desired range resolution. If not, then there exists the possibility of removing some of these spectral lines within the band in an optimal manner without having to degrade the range resolution, i.e. a form of spectral thinning. Meanwhile, the remaining

spectral lines do not necessary have to be spaced at integer multiples of the PRF value but can be any frequency interval so long this interval is lower than the PRF value so as to avoid range ambiguity. This effect will be analogous to the application of Pulse Repetition Interval (PRI) jittering in pulse radar [6]. Also, this approach is realizable if we first consider each i^{th} spectral line located at frequency wi to represent an individual narrow-band coherent transmitter/receiver. Subsequently, during each PRI, all the coherent transmitters will be simultaneously transmitting at their assigned frequencies for a pre-defined duty cycle within the PRI. As the effective bandwidth is maintained by jointly processed the returns from all receivers over an interval of time, range resolution will be maintained as well.

Thus, by using the above representation, the whole contiguous band can also be analogous to a uniform-spaced linear antenna array (ULA) in which each spectral line corresponds to an array element. Now, in the case of the ULA, it had been shown that when the ULA is not completely filled, i.e. some elements of the ULA have been removed such that the spacing between each element is no longer uniform, the modified ULA is still able to provide a comparable performance with the original ULA with some slight degradation. This degradation comes in the form of higher sidelobes [7] which translate to higher false alarms in detection due to higher Peak Sidelobes (PSL) or higher error variance in target parameter estimation due to the increase in Integrated Sidelobes (ISL). Also, the degree of degradation is proportional to the number of elements that have been removed from the ULA.

By using the perspective between the spectrum band and the ULA, this then opens the possibility of applying techniques developed for optimal design of sparse antenna array or array thinning into the spectrum thinning problem mentioned above. For instance, we can now view the problem from the perspective of allocating sufficient frequency contents (minimal redundancy) such that the radar range resolution is maintained with some side-lobe performance degradation but with lesser frequency contents as compared to utilizing the whole contiguous band with the tradeoff being a degraded side-lobe performance. This viewpoint is analogous to the concept of the Minimum

Redundancy Linear Array [45] or MRLA within the antenna array communities. Moreover, the frequency band occupied by the removed frequency samples can now be utilized by another application. Thus, this is the motivation for the Sparse Spectrum/Bandwidth Allocation (SSA/SBA) optimization scheme that forms Part 1 of the dissertation.

In the SSA scheme, the process of removing the frequency sample locations (akin to Array Thinning) is determined via a metric known as the Marginal Fisher Information or MFI in short. Now, from the theory of Statistical Estimation [8], it is known that the error variance of an unbiased estimator is bounded by the Cramer-Rao Lower Bound (CRLB) which is the inverse of the Fisher Information of the measurements. If we are to view all the frequency samples as measurements in the frequency domain, then it will be possible to compute the Fisher Information for the entire spectrum band. By using a iterative search approach, whenever one or more contiguous groups of frequency samples is removed, the SSA scheme will compute the difference in Fisher Information between that of the entire spectrum band versus that of the remaining samples and this difference will be the MFI. Thus, the SSA scheme will release the frequency band/bands corresponding to the group/groups of frequency samples that produces the lowest decrease of MFI to be used for other applications. This process will continue until the results have reached convergence.

1.2.2 Waveform Design with Good Spectral Containment

The coexistence of radar and wireless communication systems in a Congested Spectrum will inevitably lead to an increase of interference being present in the received signals of both systems when they are jointly operating in time and space. As such, it is of utmost importance by each system to generate transmit waveforms that do not spill over to the adjacent spectrum bands. As a result, it has fueled the motivation to research into transmit waveforms that provide good spectral containment and various designs have appeared in the literature over these years.

Now, it is known among the researchers that waveforms designed using the Continuous Phase

Modulation (CPM) framework [9] has the desirable properties of being both constant modulus and good spectral containment or spectrally efficient as defined under the radar context. Both properties are desirable as the constant modulus feature will translate into the maximum transmission of energy while the spectral efficiency feature will ensure minimal interference to adjacent spectral users such as other radars or communication systems. In the radar domain, the adaptation of the CPM framework has also been successfully demonstrated in ([4],[10]-[11]) in the form of Polyphase Coded Frequency Modulated (PCFM) waveforms. Furthermore, it is also observed that the PCFM waveforms is able to achieve low autocorrelation sidelobes relative to time-bandwidth (BT) product where B is the 3 dB bandwidth. Also, in [4], it is observed that the phase of the PCFM waveform can be viewed as a first-order hold as compared to the zeroth-order hold phase representation in phase-coded waveforms like the Barker or P3 codes. In addition, by examining the relatioship between the frequencies versus chirp rate of this first-order hold representation of PCFM waveform in [12], it can be seen that the frequency variation with time follows the laws of Nonlinear Frequency Modulation (NLFM).

Next, by viewing the PCFM waveform as a first-order hold phase function, there lies the possibility of generalizing the implementation of PCFM waveform to higher-order hold phase representations that will still retain the desirable properties of being both constant modulus and spectrally efficient. By drawing inspiration from the polynomial phase functions proposed by Doerry ([13]-[14]), Part 2 of the dissertion will cover the development of higher-order hold PCFM waveforms that will also opens up the possibility to combine multiple orders to obtain even lower autocorrelation sidelobes. At the same time, the framework for generating the optimized first-order PCFM waveforms as described in [15] will be expanded for the design of these higher-order PCFM waveforms as mentioned above.

1.3 Overview of Dissertation

The remaining chapters of this dissertation will be organized as follows. In Chapter 2, the findings obtained from the literature review of the existing techniques that had been developed for addressing the issues of spectrum congestion and sharing will be presented. This then set the stage for discussing the research work that is described in part 1 & 2 of the dissertation which will increase the extent of research covered by the reviewed existing techniques.

In Chapter 3 that addresses Part 1 of the research, detailed derivations of the theory and principle behind the design of the Sparse Spectrum Allocation (SSA)algorithm will be presented. Next, the chapter will then describs about the various adaptations of the SSA algorithm that are grouped under two different perpspectives of sparse array design versus array thinning. At the same time, all the accompanying simulation results for each of these adaptations under the two perspectives will also be provided and examined in details.

In Chapter 4 that addresses Part 2 of the research, detailed derivations of the steps needed for waveform design of the higher-order waveform under the PCFM framework will be presented along with all accompanying simulation results for different implementations of these higher-order PCFM waveforms either as single-order waveform configuration or as multi-order waveform configuration. This chapter will also delve into the insights between the interations among different orders of implementation as well as the theoretical limits for the code values in each respective order of implementation.

In Chapter 5, the first section will illustrate the feasibility of using the results obtained from the Sparse Spectrum Allocation algorithm to generate the corresponding PCFM waveforms by providing several examples of the these waveform implementations. In the second section of this chapter, a radar target range profile estimation application example will be provided to illustrate the viability of applying the Sparse Spectrum Allocation algorithm results to this important radar

application.

Finally, in Chapter 6, the dissertation will provide the summaries to all the research that are reported in this dissertation. Some recommendations for continuing with the further stages of this research will be discussed in the this Chapter as well.

Chapter 2

Literature Review

In this Chapter, a brief overview of the approaches adopted to address the challenge of Spectrum Congestion will be provided with the focus of these approaches on the coexistence and spectrum sharing between the radar and wireless communication systems.

2.1 Spectrum Sharing between Radar and Communication

As previously mentioned, in recent years, it has become even more necessary for radar systems to co-exist with wireless communication systems in some form of spectrum sharing scheme within the same spectrum of usage. Now, the main direction for seeking feasible solutions for spectrum sharing between radar and wireless communicated can be grouped into 3 categories [5] that are described in more details in the following sections.

2.1.1 Category 1: Design of Cognitive Radio

In this category, the primary user of the spectrum is assumed to be the radar system whereas the secondary user is assumed to be the communication system and the focus is on spectrum sharing via time/spatial/frequency domain resources multiplexing. Therefore, based on the above assumption, the onus to ensure an effective sharing of the above resources is usually on the secondary user

which is the communication system. As such, this added responsibility will require the communication system to function as a form of cognitive radio that will utilize advanced sensing capabilities to detect the presence of the signals emitted by a radar system and perform suitable adjustment to its operations accordingly. Also, unlike conventional spectrum sensing approaches that are based on energy detection, an example of a newer spectrum sensing method is based instead on detecting the entropy of the received signals by utilzing the information that a stochastic signal with Gaussian probability density has the maximum entropy. Examples of research that are performed under Category 1 are listed in ([16]-[17]).

For example, in [17], the authors started with the description on difference between *white space* approach in which the secondary device/user will only transmit when the radar system is so far away such that it is undetectable versus the *gray space* approach at which the secondary device is allowed to transmit in vicinity of the radar system but with a transmit power that will not cause harmful interference to the radar system. As such, the characteristics of the transmit power from the secondary device will vary over time based on the properties of the radar signals that it has sensed during its operation. For the research reported in [16], the example radar system chosen is a rotating radar that can be used for weather monitoring or Air Traffic Control (ATC).

2.1.2 Category 2: Design of Cognitive Radar

In this category, the focus is on a robust radar system which will minimize interference signals to/fro the communication when both systems are utilizing within or nearby spectral band. For a start, the primary requirement will be the design of radar waveforms that are spectrally well contained without its specified band limits so that energy from the radar signal will not spill over to nearby bands that may be utilized by other radar or communication systems. In addition, in instances when there are strong interfering signals from a communication system located within the spectrum band of the radar system, there are two possible approaches to mitigate this unwanted interference.

The first approach will be to design radar waveforms that are more tolerant to the higher clutter power transmitted from the communication system. Some examples of research reported in this approach are listed under ([18]-[22]). For example, in [18], the authors address this approach of waveform design using an information-theoretic perspective by maximizing the mutual-information between the radar's target response (which mimics the channel of traditional MIMO systems) and the radar received signals while constraining the spectrum to avoid a co-existing communication system. In addition, the waveform design also incorporates constraints that reduces interference to a communication system, avoid clutter returns and also satisfies the radar system design constraints such as maximum transmit power and peak-to-average-power ratio (PAPR).

The second approach will necessitate the design of transmit/receive waveforms with notches present in some frequency sub-bands of the contiguous spectrum band so that no energy will be transmitted/received in these sub-bands or "forbidden" bands ([23]-[30]). For instance, in [24], the authors achieve this objective of waveform design by introducing small modifcations to the phase modulations of a N-step radar pulse in order to create spectral nulls for either in-band or out-of-band RF interfering signals from other systems.

This approach thus leads to the popular concept of sparse frequency waveform for both transmit/receive function such that the interference to/from the communication system can be avoided during operation. In all cases, design of sparse frequency waveforms will necessitate many iterations in order to obtain the optimized results once convergence to these results is achieved. Also, due to the demands placed on the radar system in this category in terms of spectrum consideration, the radar system in this category can be classified as an intelligent or cognitive radar in the spectral sense.

2.1.3 Category 3: Joint Design of Cognitive Radio/Radar

In this category, the focus is on joint design of both radar and wireless communication systems to cooperatively mitigate the amount of interference to each other and again there are multiple

approaches to achieve this objective. The first approach may be to define a multi-objective optimization criteria so as to obtain the most efficient usage of the bandwidth shared by both radar and communication systems. One example of this joint optimization framework can be the design of a multi-modal radar in which its allocated bandwidth can be reduced in accordance to the scattering characteristics of the current active target scenario at hand so that the unused bandwidth can be utilized by the communication system.

Another approach may be to combine the operations of both cognitive radio and cognitive radar in a cooperative manner such that both systems possess advanced spectrum sensing capabilities as well as sharing information of the operating environment of both the communication and radar environments so as to achieve the most effective usage of the shared bandwidth. Also, some examples of research that are performed under this category are listed in ([31]-[33]). For instance in [31], the authors explores a collocated overlapped multiple-input multiple-output (MIMO) antenna architecture and a spectrum sharing algorithm via null space projection (NSP) for enabling the coexistence of both radar and communications systems. In their proposed overlapped-MIMO architecture, the transmit array of a collocated MIMO radar is partitioned into a number of subarrays that are allowed to overlap. Each of the antenna elements will also be tarnsmitting signals orthogonal to others in the same subarray and to the other subarrays. At the same time, the radar-centric spectrum sharing scheme then projects the radar signal onto the null space of the communications system's interference channel so as to avoid the communication system receiving interference from the radar.

The third approach is achieved by using the OFDM waveforms as a design tool. From simulations, it has been shown that it is possible to design a set of OFDM transmit waveforms that can be allocated for usage by both radar and communication systems. Some recent examples of waveforms that falls into this category are the Multi-modal OFDM waveform as reported in [34]. In this paper, the authors achieve this objective by appropriately allocating the OFDM sub-carriers for both systems based on using the radar detection performance as well as the communication

channel capacity as the performance metrics for the allocation of these sub-carriers. To sum up, some examples of research that are performed under this category are listed in ([34]-[36]).

At this point, the brief overview of the 3 categories that are created to resolve the challenge of spectrum sharing between radar and wireless communication systems has been provided. Now, as mentioned in the introduction chapter, the solutions described under Part 1 and 2 of this dissertation to address the issues of spectrum congestion/sharing will fall mainly under the second category of a robust or intelligent radar. Although the first part of the proposal does not utilize the scheme of waveform design to fulfill sparsity of the radar spectrum usage of the contiguous spectrum, however, the goal of using a reduced amount of bandwidth is obtained via the design of an optimal spectrum/bandwidth allocation scheme derived from applying the principles of information and statistical estimation theory.

2.2 Sparse Spectrum Utilization by Radar

To date, almost all of the research performed on sparse spectrum usage from a contiguous spectrum band for radar applications is concentrated on the design of sparse waveforms with some exceptions of recent development on Sub-Nyquist radar system as reported in ([37]-[38]). For instance, in [37], the authors identified a small subset of spectrum groups/blocks for usage out of the contiguous spectrum by basing on a heuristic approach whose results mimic randomly distributed groups. Starting from the results obtained from the design of sparse frequency waveforms published by the author in [39] that provides the theoretical derivation of both complex digital transmit and receive ultra-wideband radar and communication waveforms that possess both excellent arbitrary frequency band suppression and range sidelobe minimization, it has lead to a host of publications by other authors with a snippet as listed in ([40]-[45]). At the same time, within the literature of design approach of sparse frequency waveform, this aspect of research can also be viewed in the context of thinned spectrum waveform design ([26],[43]). Thus, with the literature

survey results provided on sparse spectrum usage, the research that is described in Chapter 3 of this dissertation on identifying the best possible subset of frequency sub-bands from a contiguous band in terms of target estimation error performance and independent of waveform design can be considered a **novel** research direction in this aspect.

Now, as mentioned in section 1.2.1, the identification and selection of these best possible subset of frequency sub-bands from the perspective of target estimation error is obtained using a sparse spectrum allocation algorithm that mimics the design of sparse array akin to minimum redundancy linear array (MRLA) or low redundancy linear array (LRLA) utilized in antenna array design. Similarly, the sparse spectrum allocation algorithm can also be classified under the research category of array thinning in antenna array design. With that in mind, the literature review then focus on the research that have been reported in this domain.

Previous research on generating MRLA can be grouped into two categories, i.e. either non-statistical or statistical approaches. Now, for the non-statistical approach, some provided examples are such as those reported in ([48]-[53]) that are variant adaptations to Moffet [47] which is commonly recognized as the pioneer publication of this approach and is based on adopting the findings on deriving both unrestricted and restricted difference bases of integers as reported by Leech [46].

Next, for the statistical approach which is much more computational intensive in nature, it has gained much popularity over the last two decades due to the exponential increase in technology and power in Digital Computing and Very Large Scale Integrated (VLSI). As such, results obtained via numerous statistical techniques such as Simulated Annealing [54], Pattern Search algorithms [55], Particle Swarm Optimization [56] or the Genetic Algorithm [57] among others have been reported to be able to successfully generate arrays that either possess the qualities of the MRLA or LRLA.

However, one limitation that is common to all these approaches is the ability to produce either the MRLA or LRLA when the original array size to be thinned down is large, i.e. consisting of hundreds of array elements etc. Furthermore, the algorithms utilized in the statistical approach also

require large computation time to generate results for any sizable array dimension. To overcome the limitations from the above approaches, an alternative algorithm [58] that is designed based on a measure known as the Marginal Fisher's Information (MFI) was demonstrated to be able to generate a sparse/thinned array configuration in an optimal manner while using much lesser computation resources as compared to the statistical approach. In the paper it was shown that the coarray computed from the sparse array possess minimum or low redundancies that closely resembles the coarrays obtained from a MRLA or LRLA. Based on the good results as reported in [55], thus this algorithm is proposed to be used as the basis of the optimum spectrum allocation scheme by essentially performing the optimal selection of spectral lines within the full spectrum band while ensuring that the range resolution performance is maintained.

2.3 Spectral Containment via Higher-order PCFM waveforms

Due to the ever-increasing demands placed on the congested RF spectrum by the wireless communication industry, it has led to the push for greater design freedom, enhanced sensitivity within the radar communities ([59]-[60]) so as to allow for coexistence of both radar and communication systems. At the same time, new sensing modalities have also yielded myriad contributions to the burgeoning field of waveform design diversity ([61]-[64]).

Historically, Frequency modulation (FM) represents the original [65] and by far most widely used means of generating a radar waveform for use in pulse compression. After the establishment of the linear frequency modulated (LFM) chirp, the prospective benefits of nonlinear FM (NLFM) waveforms were realized (as further elaborated in the next paragraph), followed by a litany of important contributions (e.g. [66] - [74], and [90] - [93]). In short, FM waveforms are attractive because they can be generated with very wide bandwidths as well as possessing the characteristics of constant amplitude and good spectral containment and therefore they are readily amenable to high-power radar transmitters. In the case of LFM, this implementation also allows the use of stretch processing on receive [75].

A separate class of waveforms that has also attracted significant attention is that of phase-coded sequences (e.g. [76] - [79]), particularly with the emergence of waveform diversity ([61], [74]) and the prospect of incorporating dimensions of space, Doppler, polarization, etc. into the design process. While not directly implementable without distortion (refer to [4], [74]), phase codes are very important because they represent the means with which to parameterize the structure of a signal in a way that can be optimized.

While there has been considerable work on the design of radar codes (e.g. [64] and references therein) it has only recently be shown that a modified form of the continuous phase modulation (CPM) [9] scheme used in some communication application can be used to connect the mathematically attractive structure of phase codes to the physically realizable structure of FM waveforms. Denoted as Polyphase-coded FM (PCFM) [4], this framework can be used to convert an arbitrary polyphase code into an FM waveform that can be readily transmitted by a high-power radar. However, the more important benefit of this approach is that it facilitates the direct design of FM waveforms through optimization of the parameterized structure of codes [15]. In so doing, distortion-inducing effects of the transmitter (most notably the power amplifier) can be incorporated into the waveform design process ([15], [80]-[81]) and spatial and polarization degrees-of-freedom can be physically coupled to waveforms [[82] - [86]]. It has recently even been shown that the PCFM implementation enables a new form of radar-embedded communication [87] and the design of FM waveforms via gradient descent optimization of the coded parameters [88].

Now, the PCFM scheme that is described in[4] can be viewed as converting codes into FM waveforms in a manner akin to first-order hold in the phase domain of these waveforms since the use of a rectangular shaping filter produces piece-wise linear phase trajectories after the integration stage. In addition, the structure of PCFM itself has also been examined via the notion of "overcoding" [89] of the code values. Likewise, the well-known LFM waveform and waveforms constructed piecewise from LFM waveforms with different chirp-rates are examples of a second-order hold representation that correspond to quadratic phase trajectories. By using such a analogy,

it then provides the possibility of generalizing the PCFM framework of implementation to higher-order hold representations of the phase function. In essence, this generalization enables new ways and techniques in which to represent NLFM waveforms where, in theory, there are infinite possible continuous phase functions that may exist, even for a finite pulse width and bandwidth. Moreover, it is noted that many of these techniques ([68] - [79], and [91] - [94]) are based on the Principle of Stationary Phase, which as described in [61], states that the energy/power spectral density at a particular frequency of a NLFM signal is relatively large if the rate of change of the frequency at that time is relatively small. In essence, this implies a inverse relationship between the spectral density and the chirp rate at that frequency. Since it is also known that the autocorrelation function of a signal is equal to the fourier transform of the spectral density function, thus by selecting a predefined shape of the spectral density function, it will both determine the corresponding phase function of the signal as well as the sidelobe performance of the autocorrelation function of this signal.

To conclude, based on the literature review provided under this section, the desirable properties of the PCFM waveform as well as the possibility of generalizing the PCFM framework into another good underlying code representation for NLFM waveforms have been clearly emphasized. Thus, the objective of Part 2 of the two-step approach that is adopted in this dissertation will be focused on developing the second to higher-order PCFM representations. At the same time, the information provided below in Table 2.1 offers a general comparison between the different orders (1st and higher) and also includes polyphase codes themselves as a notional zero-order representation. It is hoped that based on the comparison shown in Table 2.1, the framework of the research into the higher-order PCFM representations in relation to the current implementation of NLFM waveforms will be understood in a clearer perspective.

Table 2.1: Waveform Representations

Waveform representation	**Equivalent approaches in radar waveform generation**
0th order	Discrete codes (e.g. P3); abrupt phase transitions
1st order	PCFM via [6]; linear phase transitions
2nd order	LFM and NLFM; quadratic phase trajectories
3rd order & Higher	Higher orders of NLFM

Chapter 3

Optimization Scheme for Sparse Spectrum Allocation

3.1 Theoretical Background

3.1.1 Radar Measurement Model

As described in the previous chapter, it is possible to view the contiguous RF spectrum for a radar system to be consisting of many spectral lines with each spectral line representing a physical coherent transmitter that transmits a waveform with constant amplitude at a frequency that corresponds to that spectral line. Also, the transmitter will be turned on/off with a finite duration during each period corresponding to the PRI. Thus, it is possible to define a radar measurement model in the frequency domain as in the time domain. For a start, we define the measurements received at the radar over the CPI duration by the following equation:

$$\mathbf{v} = \mathbf{H}\gamma \tag{3.1}$$

$$\mathbf{H} = [h_1, h_2, h_i, ...], i = 1...M \tag{3.2}$$

Where the symbol $\mathbf{v}$ is the $Kx1$ radar measurement vector in frequency, $\mathbf{H}$ is a KxM matrix that is the observation matrix or the sensing matrix for this model. Note that for the matrix $\mathbf{H}$, each element along the row dimension represents an observation associated with a unique and increasing frequency and each element along the column dimension represents an observation associated with a unique and increasing target distance from the radar receiver. Thus, $\mathbf{H}$ can also be represented by M column vectors $\mathbf{h}_i$ as shown in (3.2). Also, an analogy to the column vector $\mathbf{h}_i$ in (3.2) will be the array manifold vector corresponding to the physical angle θ_i in a direction finding problem. Finally, γ is an Mx1 vector with each element γ_i corresponding to the complex scattering coefficient of a target located at distance x meters away from the radar receiver.

Before going further, it must be emphasized that taking measurement samples in frequency is the dual problem of taking measurement samples in time. As it is well known that the temporal sampling rate will determine the sampling bandwidth in frequency, thus the corresponding frequency sampling interval between two frequency samples will also determine the temporal time-span in time corresponding to unambiguous target distance. In addition, while the total observation time T_0 for temporal sampling determines the frequency resolution $(1/T_0)$, so will the span of the frequency samples determines the temporal resolution, i.e. range cell resolution in meters.

Going further, (3.1) is further modified to include the complex measurement noise vector n such that the final radar measurement model in frequency is as follows:

$$\mathbf{v} = \mathbf{H}\gamma + \mathbf{n} \tag{3.3}$$

This form of this equation is what is popularly known in literature as the linear model. An additional note to take is that as there is a one-to-one mapping between the target distance x with the time delay τ_d to the receiver, the elements in vector γ can be viewed as a target delay spectrum of the time delay parameter τ_d.

3.1.2 Cramer Rao Bound and Marginal Fisher Information

By defining the radar measurements in frequency as a linear model given in (3.3), we can then proceed to examine the relationship between the amount of frequency measurements allocated in the vector v with that of the results obtained from the estimation of the vector γ that is denoted by the symbol $\tilde{\gamma}$. Note that the estimated $\tilde{\gamma}$ will not be identical to the actual γ but will contain estimation errors.

Now, the estimation error and its corresponding covariance matrix given by the following:

$$\varepsilon = \tilde{\gamma} - \gamma \tag{3.4}$$

$$\mathbf{K}_{\varepsilon} = E\{\varepsilon\varepsilon'\} \tag{3.5}$$

From [8], it is known that the lower bound of the error covariance is given by the Cramer-Rao Lower Bound (CRLB) which is equal the inverse of the Fisher Information matrix of the measurement vector which can be expressed by (3.6) below

$$\mathbf{J} = E\{[\bigtriangledown_{\gamma} \ln(f_{v|\gamma}(\mathbf{v})][\bigtriangledown_{\gamma} \ln(f_{v|\gamma}(\mathbf{v})]^{H}\} \tag{3.6}$$

where $\bigtriangledown_{\gamma}$ is the gradient operator and $f_{v|\gamma}(\mathbf{v})$ is the probability density function of $\mathbf{v}$ given γ as cited in [94].

At the same time, for the linear model defined in (3.3), when applying an efficient estimator such as the Minimum Mean Square Error (MMSE) estimator to the frequency measurements, the error covariance obtained for the estimated $\tilde{\gamma}$ will be equal to the CRLB. It is with this understanding that the Sparse Spectrum Allocation (SSA) algorithm based on Marginal Fisher Information (MFI) is derived. For a start, if we denote the Fisher Information matrix obtained from K number of frequency measurements in vector v as $\mathbf{J}_K$, and the Fisher Information matrix from $(K-1)$

frequency measurements as $\mathbf{J}_{K-1}$, the Marginal Fisher Information matrix obtained from the k^{th} frequency measurement is defined as the nonnegative definite matrix $\Delta J(K)$ given by:

$$\Delta \mathbf{J}(K) = \mathbf{J}_{K-1}^{-1} - \mathbf{J}_{K}^{-1} \tag{3.7}$$

From the MFI matrix $\Delta J(K)$ defined in (3.7), the MFI obtained from the k^{th} frequency measurement is defined as follows:

$$\begin{aligned} MFI &= \frac{1}{M} \times Tr\Big(\Delta \mathbf{J}(K)\Big) \\ &= \frac{1}{M} \times \Big[Tr\big(\mathbf{J}_{K-1}^{-1}\big) - Tr\Big(\mathbf{J}_{K}^{-1}\big)\Big] \\ &= \frac{1}{M} \times \Big[Tr\big(\mathbf{K}_{\varepsilon(K-1)}\big) - Tr\big(\mathbf{K}_{\varepsilon(K)}\big)\Big] \end{aligned} \tag{3.8}$$

where $Tr(.)$ is the trace operator and M is the number of elements (targets) in the vector γ.

In a way, the MFI is a measure of the new information that is obtained when adding the k^{th} frequency measurement to the original $(K-1)$ measurements. From the perspective of sparse array design, the MFI can be viewed as a "reduction in uncertainty" metric since adding the k^{th} frequency measurement may result in a non zero-valued $\Delta J(K)$ that indicates an increase in information to reduce the uncertainity/error in estimating the vector γ. Alternatively, it may also result in a zero-valued $\Delta J(K)$ when $\mathbf{J}_K$ is equal to $\mathbf{J}_{K-1}$ which indicates that no new information is provided from the k^{th} measurement. In the former case, this will correspond to a reduction of the error variances within $\mathbf{K}_\varepsilon$ of the estimated $\tilde{\gamma}$ due to this additional information provided by the k^{th} measurement. In the later case, this will not provide any reduction in the error variances within $\mathbf{K}_\varepsilon$.

Likewise, from the perspective of array thinning design starting from an initially fully filled array, the MFI can also be viewed as the amount of increase of the error variances within $\mathbf{K}_\varepsilon$ of $\tilde{\gamma}$ when the number of measurements in the vector $\mathbf{v}$ has been reduced by one from the initial N

measurements.

Next, when applying the MMSE estimator for the measurements expressed using the linear model, by removing the mean from the vector γ, the expression for this estimator as well as the estimated $\tilde{\gamma}$ are given by (3.9) and (3.10) as

$$\mathbf{W}_{MMSE} = \mathbf{K}_{\gamma}\mathbf{H}'(\mathbf{H}\mathbf{K}_{\gamma}\mathbf{H}' + \mathbf{K}_n)^{-1} \tag{3.9}$$

$$\tilde{\gamma} = \mathbf{W}_{MMSE}\mathbf{v} \tag{3.10}$$

where $\mathbf{K}_{\gamma}$ is the a priori target covariance matrix and $\mathbf{K}_n$ is the covariance matrix due to the measurement noise. Likewise, the error covariance matrix $\mathbf{K}_{\varepsilon}$ obtained for the estimated $\tilde{\gamma}$ when using the above Minimum Mean Square Error (MMSE) estimator is expressed as

$$\mathbf{K}_{\varepsilon} = \mathbf{K}_{\gamma} - \mathbf{K}_{\gamma}\mathbf{H}'(\mathbf{H}\mathbf{K}_{\gamma}\mathbf{H}' + \mathbf{K}_n)^{-1}\mathbf{H}\mathbf{K}_{\gamma} \tag{3.11}$$

However, from [8], it is seen that the above equation (3.11) can also be expressed as

$$\mathbf{K}_{\varepsilon} = (\mathbf{H}'\mathbf{K}_n^{-1}\mathbf{H} + \mathbf{K}_{\gamma}^{-1})^{-1} \tag{3.12}$$

As such, any reduction of the error variances due to an additional measurement can be computed by applying the trace operator to the error covariance matrix $\mathbf{K}_{\varepsilon}$ as defined in (3.12). Finally, as mentioned above, since the Fisher Information matrix $\mathbf{J}_K$ is equal to the inverse of $\mathbf{K}_{\varepsilon}$, by using (3.11), $\mathbf{J}_K$ is defined as

$$\mathbf{J}_K = (\mathbf{H}'\mathbf{K}_n^{-1}\mathbf{H} + \mathbf{K}_{\gamma}^{-1}) \tag{3.13}$$

Moreover, if $\mathbf{K}_{\gamma}$ and $\mathbf{K}_n$ are defined by the following equations

$$\mathbf{K}_\gamma = E\{\gamma\gamma'\} = \sigma_\gamma^2\mathbf{I} \tag{3.14}$$

$$\mathbf{K}_n = E\{nn'\} = \sigma_n^2\mathbf{I} \tag{3.15}$$

then (3.12) and (3.13) can be rewritten as

$$\mathbf{K}_\varepsilon = (\sigma_n^{-2}\mathbf{H}'\mathbf{H} + \sigma_\gamma^{-2}\mathbf{I})^{-1} \tag{3.16}$$

$$\mathbf{J}_K = (\sigma_n^{-2}\mathbf{H}'\mathbf{H} + \sigma_\gamma^{-2}\mathbf{I}) \tag{3.17}$$

From (3.17), we can also view the Fisher Information matrix $\mathbf{J}_K$ as the sum of two components $\mathbf{J}_v$ and $\mathbf{J}_\gamma$ where $\mathbf{J}_v$ represents the information obtained due to the measurement data in $\mathbf{v}$ and $\mathbf{J}_\gamma$ represents the information obtained due to prior knowledge of γ. Using these representations, (3.17) can simply be expressed as

$$\mathbf{J}_K = \mathbf{J}_v + \mathbf{J}_\gamma \tag{3.18}$$

3.1.3 Definition of Coarray versus Beampattern of Sparse Array

In [95], it is stated that for a thinned requlr array or sparse array, the coarray of this sparse array is defined as the autocorrelation of the element weights

$$c(l) = \sum_{m=0}^{N-|l|-1} w_m w_{m+|l|} \tag{3.19}$$

where $w_m \in \{0,1\}$ is the element weight and its value will indicate the presence or absence of the array element at location m. Also, N is the total number of elements in the fully-filled aperture. As such, for an N element linear array with element distance d, the coarray for this linear array is related to the beampattern $|W(k)|^2$ of the linear array as

$$|W(k)|^2 = \sum_{l=-(N-1)}^{N-1} c(l) exp(jkld) \tag{3.20}$$

where $k = 2\pi/\lambda$ is the wave-number (spatial frequency). Therefore, from (3.19), it can be seen that the beampattern of the linear array is equivalent to the Fourier Transform of its coarray. Likewise, the beampatterm can also be viewed as the Matched Filter Response of the linear array at the *zero delay* location. Also, due to the symmetry of the coarray, (3.20) can be rewritten as

$$|W(k)|^2 = c(0) + \sum_{l=1}^{N-1} 2c(l) cos(kld) \tag{3.21}$$

which is a superposition of cosines.

Next, the interpretation of the coarray element $c(l)$ is such that if $c(l) > 1$, then l is a redundant lag. Likewise, if $c(l) = 0$, then the coarray has a hole in l. In terms of array nomoclature, a perfect array is one that has a coarray that possesses no holes or redundancies except for lag zero. However, for a sparse array with number of elements n, there is no such perfect array for $n > 4$. Thus, this inspires the studies of approximate perfect arrays such as the Minimum Redundancy Linear Array (MRLA) or Minimum Holes Linear Arrays (MHLA).

Therefore, with the above descriptions provided for both the coarray and beampattern of a linear array, they will be used to evaluate the resulting sparse array obtained from the SSA algorithm that is implemented based on either from the perspective of sparse frequency array design or from the perspective of frequency array thinning design.

3.2 Implementation of SSA algorithm based on Sparse Array Design Perspective

In this section, the first perspective of sparse array design will be adopted to design the SSA algorithm. In the subsequent section of Chapter 3, the second perspective of array thinning starting from an initially fully filled array will then be adopted for the design of the SSA algorithm.

Now, under the perspective of sparse array design, the main objective of the SSA algorithm is to allocate the optimal locations for a K number of spectral lines/samples (corresponding to a fraction of the total spectrum) out of a N number of total spectral lines (corresponding to 100% of the spectrum usage) where $N > K$ and using the MFI as the optimization metric. Now, this objective can be achieved via two approaches. The first approach is carried out by determining the K frequency locations corresponding to K number of spectral lines one spectral line at a time during the optimization process. The first step of the second approach is to subgroup these K spectral lines into smaller P groups/blocks of frequency lines with Q number of frequency lines per group/block such that $(P \times Q) = K$. The second step is then to determine the starting frequency location of each of these P blocks of frequency lines one block at a time during the optimization process. The description for implementing the SSA algorithm using the first approach is described as follows and followed by that of the second approach.

For the first approach of insertion based on single frequency location, initially, the algorithm will allocate the first frequency measurement sample corresponding to the first spectral line, at the frequency location $(\frac{-BW}{2})$ where BW is the span of the contiguous spectrum band. Subsequently, the algorithm will use the MFI metric to determine the optimal spectral locations from the 2^{nd} to the k^{th} measurement sample using a greedy search method on a frequency sample by sample incremental basis. Also, note that for the identified location of the $(M+1)^{th}$ measurement that is to be added to a frequency array of M measurements, it is chosen as the candidate from out of $(N-M)$ possibilities that produces the largest reduction of the estimation error. This process

will go on until all K number of frequency locations have been determined. This will then be considered as the completion of the 1st iteration. Next, after all initial K frequency locations have been allocated from this first iteration, the iteration is then repeated again where the first frequency location is again to be determined out of the possibility of $(N-K+1)$ frequency locations. Once the second iteration is completed, the process will continue with the third iteration until the results have reached convergence.

For the second approach of insertion based on groups or blocks of frequency locations, as a start, the algorithm will allocate the first block of Q frequency samples with its starting spectral line, at the frequency location $(\frac{-BW}{2})$ which corresponds to one end of the available spectrum. Subsequently, the algorithm will use the MFI metric to determine the optimal spectral locations to insert the 2^{nd} block up to the p^{th} block of frequency samples using a greedy search method on a block by block basis. Again, note that for the identified location of the $(O+1)^{th}$ frequency sample block to be added to a frequency array of O blocks of measurements, it is chosen as the candidate from out of $(N-(O\times Q))$ possibilities that produces the largest reduction of the estimation error. This process will go on until all P blocks of frequency samples corresponding to K locations have been determined. This will then be considered as the completion of the 1st iteration. Next, after all initial K frequency locations have been allocated from this first iteration, the iteration is repeated again where the first block of frequency location is again to be determined out of the possibility of $(N-(P-1)\times Q)$ number of frequency locations. Once the second iteration is completed, the process will continue with the third iteration until the results have reached convergence.

3.2.1 Construction of Sparse Frequency Array model based on Single Frequency location insertion - first adaptation

In order to evaluate the performance of the proposed Sparse Spectrum Allocation (SSA) optimization algorithm described in the previous section in generating a sparse spectrum allocation, various modules were generated up in MATLAB so as to implement the SSA scheme via simulation as well as evaluating its performance. The script for generating the sparse array measurement model is set up using the following target scenarios assumed to be for a radar application with the parameters as shown in Table 3.1 as follows.

Table 3.1: Simulation Parameters for generating MFI frequency array

Parameter Type	**Parameter value**
Span of N frequency samples, BW	-10 kHz to 10 kHz
Unambiguous target range/delay T_0	0.01 second
Nyquist sampling requirement for T_0; $2*T_0$	0.02 second
Nyquist frequency sampling interval, F_s	$(\frac{1}{2*T_0}) = 50Hz$
Oversampling grid interval for frequency samples	5 Hz
Total number of frequency samples required for BW under Nyquist, N	$(\frac{BW}{F_s}) = 400$
Number of selected samples, K	100 (25% of spectrum) 200 (50% of spectrum)

Before discussing the results obtained from the above parameter values, note that the intent of the finer sampling grid size (5 Hz instead of 50 Hz) is meant to introduce more degrees of freedom for the MFI allocation algorithm in placing the locations of the K number of spectral lines such that the nonuniformity in the frequency spacing of these K locations need not to be constrained to be a mulitple of the Nyquist frequency sampling interval.

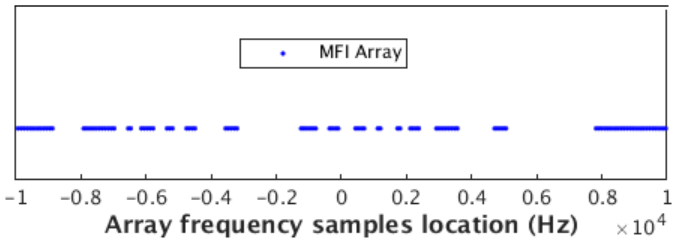

Figure 3.1: Frequency sample locations for MFI generated array for $K = 100$ (25% of total bandwidth)

As a start, the plot for the frequency sample locations for $K = 100$ samples (25% utilization of total bandwidth that is denoted as the first scenario) obtained using the MFI based algorithm is shown in Fig.3.1 above. By examining this figure, the first observation is that the minimum frequency spacing between the samples generated using the MFI based algorithm is equal to 80 Hz which is lower than 100 Hz corresponding to the target unambiguous range delay T_0. Also, there is no fixed periodicity present in the frequency spacing between these 100 frequency samples.

Next, the second observation made is that there are various gaps in the array that are much larger than the Nyquist interval. By examining these gaps closely, it is determined that there are at least 8 such spectrum gaps have sizes that are at least 2.5% of the total spectrum width and the two largest gaps having widths of 13.82% and 9.5% respectively. Also, a computation of the aggregation of these 8 spectrum gaps results in an aggregated value of 46.85%. Now, the presence of these gaps with unequal width seems to indicate that the Sparse Spectral Allocation algorithm determines that the irregular spacing between the samples will produce the least possible estimation error variances during the estimation of γ when using the 100 frequency measurement samples as compared to uniformly spacing out these frequency samples. This also means that from the perspective of measurement redundancies, it is determined by the algorithm that the irregular spacing between samples will produce an array with the low redundancies in its coarray. Note that from the viewpoint of spectrum sharing, the presence of significant spectrum gaps within the span of the full original spectrum will indicate that these spectrum gaps can be reallocated to other

operating systems such as a communication system etc.

By examining the plot of the coarray from the MFI array with that of the uniformly spaced array in Fig.3.2 as shown belows, the deduction based on the second observation is validated. From this plot, we can see that the MFI generated array does generate a coarray with much lower redundancies that resembles a low redundancy linear array (LRLA) as compared to the uniformly-spaced frequency array that contains high redundancy values.

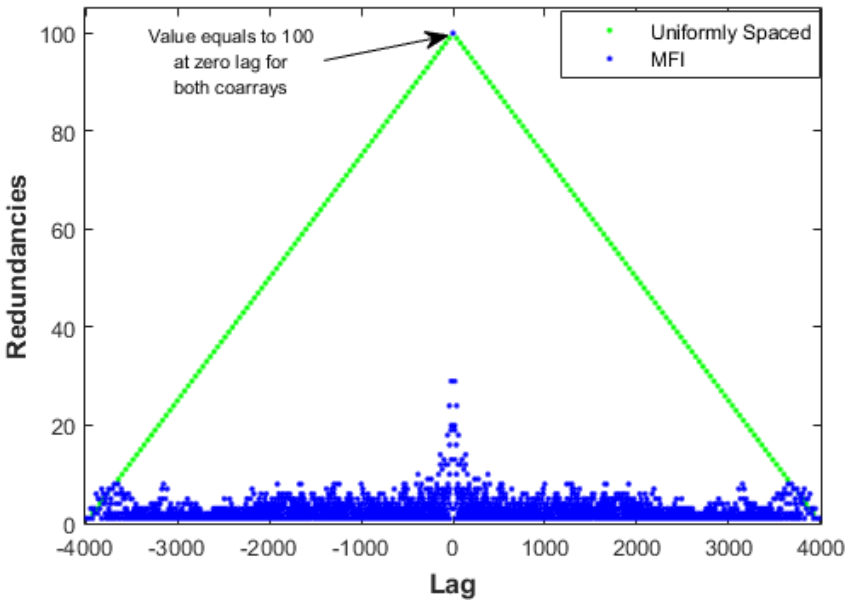

Figure 3.2: Coarrays from MFI generated array and Uniformly-spaced frequency array for K = 100

In order to examine the estimation error variances that arise when using this array, the Matched Filter operation is applied to compute the estimation errors that will arise when estimating one target located at start of the unambiguous target range, i.e. at zero delay. The resulting plot obtained is analogous to the beam pattern obtained when using the Delay-Sum beamformer as the weight vector in array beamforming operation.

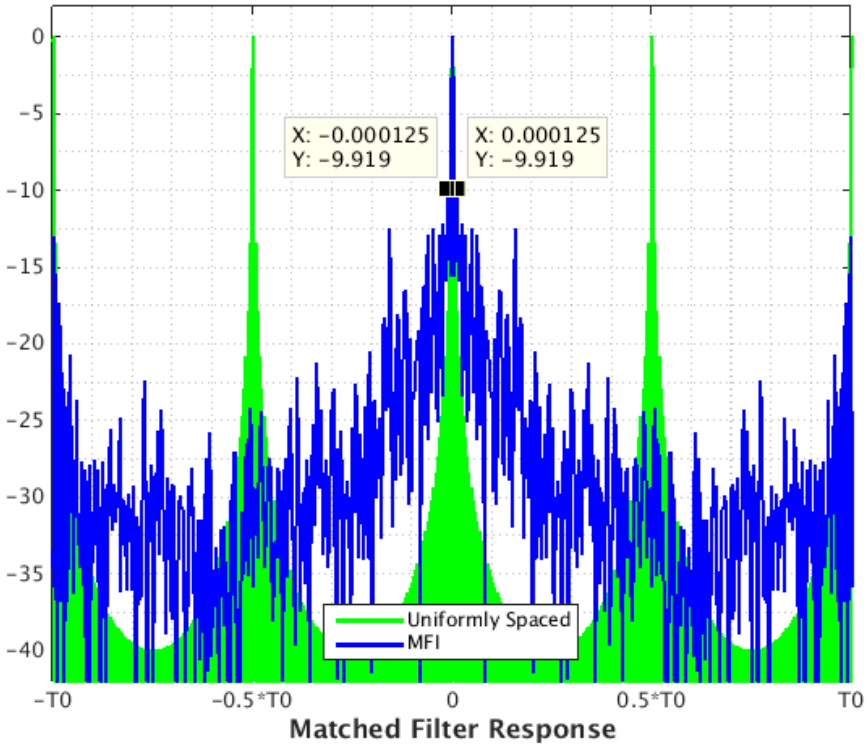

Figure 3.3: Matched Filter Response using MFI generated array for $K = 100$

From examining Fig.3.3, the first observation is that PSL value obtained from the MFI generated frequency array has a value of -9.919 dB when compared to a value of -13.50 dB when using the uniformly-spaced frequency array. This means that if there is a target with non-zero γ value located at the range corresponding to ± 0.000125 second delay in the range profile, it will contribute maximum error to the estimation of the γ value located at 0.00 second delay. The second observation made is that although the side-lobe performance of the uniformly-spaced frequency array are much better than that of the MFI generated frequency array for the same value of $K = 100$, grating lobes appeared within the span of the unambiguous range T_0 due to the frequency spacing greater than 100 Hz corresponding to T_0.

Having observed the superior performance of the MFI generated frequency array to that of the uniform-spaced frequency array for $K = 100$, we also compare this sparse frequency array to that of

an frequency array of the same size whose *K* locations are randomly generated by using a random permutation of all possible frequency locations. Next, we plot the result of the ISL of the MFI generated array versus that of the histogram results obtained from 10000 trials of randomly-spaced frequency array.

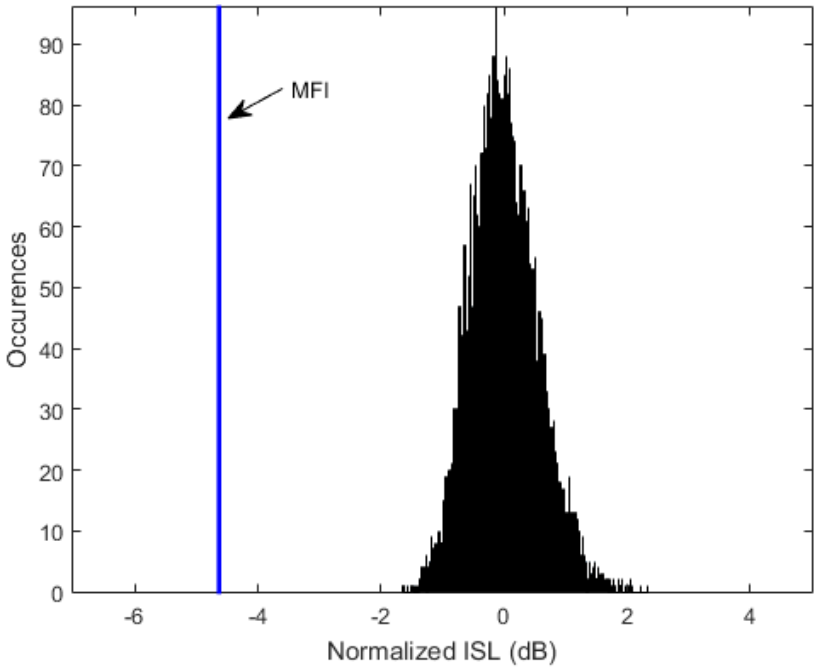

Figure 3.4: ISL value from MFI generated array and randomly-spaced frequency array using K = 100 and 10000 trials

From Fig.3.4 above, the computation of the normalized ISL from the randomly-spaced frequency array has a standard deviation of 0.5299 dB. Compared to the normalized ISL result from the MFI generated array whose value is -4.636 dB, this shows that the result from the Sparse Spectrum Allocation algorithm (MFI based) is 8.7492 standard deviations away from the average value of the randomly-spaced array. Thus, it can be seen that it is virtually impossible to generate the result obtained using the MFI based algorithm via random permutation.

Next, to investigate whether we can replicate these results using a higher spectrum usage, the second scenario in which the spectrum usage has been doubled to 50%, i.e. K is now equal to 200 measurements, was considered. The steps of the SSA algorithm as described previously are then repeated based on this new spectrum usage to generate a new set of results. The new results based on the parameter K = 200 are shown in Fig. 3.5 - 3.7 respectively.

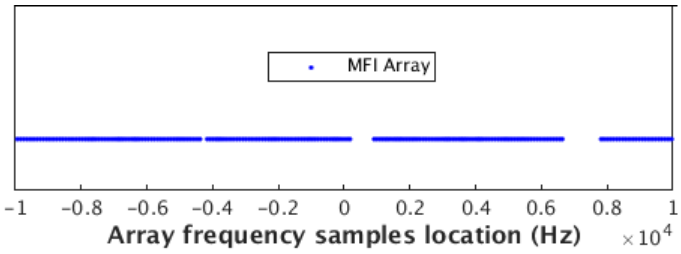

Figure 3.5: Frequency sample locations for MFI generated array for K = 200 (50% of total bandwidth)

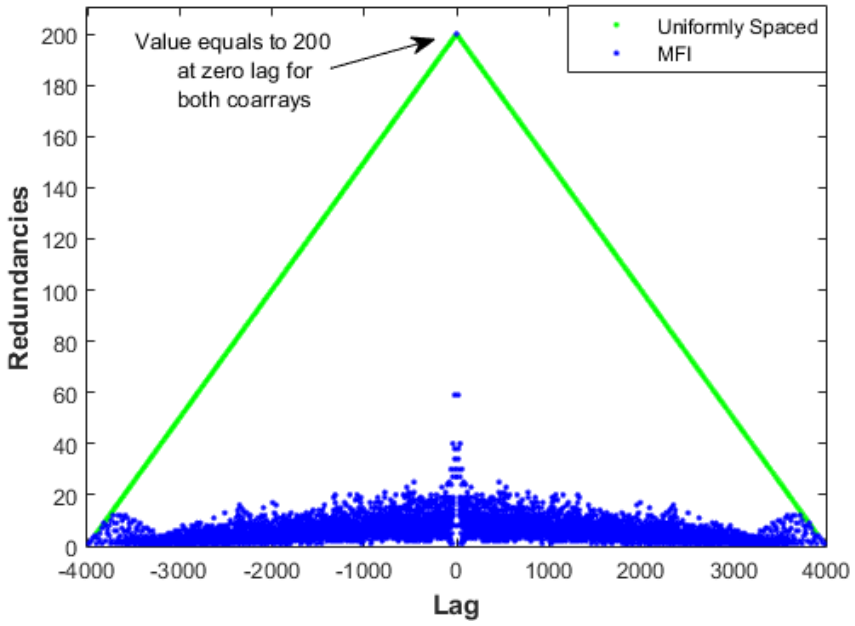

Figure 3.6: Coarrays from MFI generated array and Uniformly-spaced frequency array for K = 200

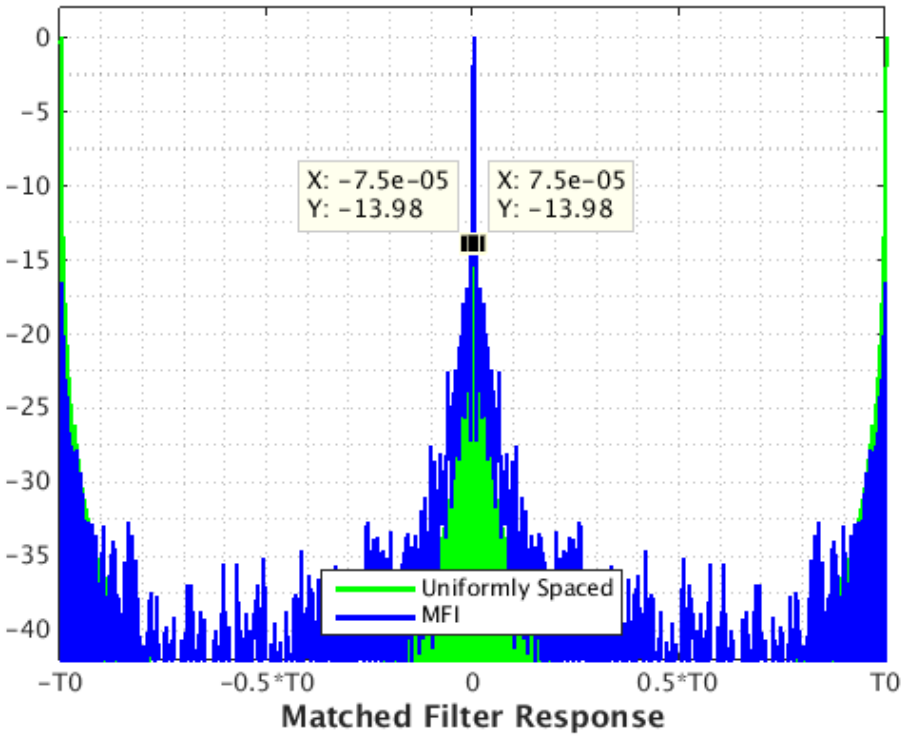

Figure 3.7: Matched Filter Response using MFI generated array for $K = 200$

By examining Fig.3.5, the first observation is that the minimum frequency spacing between the samples generated using the MFI based algorithm is equal to 75 Hz which is still lower than 100 Hz corresponding to the target unambiguous range delay T_0. Again, there is no fixed periodicity present in the frequency spacing between these 200 frequency samples.

Next, the second observation made is that the number of significant spectrum gaps in the frequency sampling array corresponding to 50% of spectrum usage are much lesser than that of the case where the spectrum usage is equal to 25%. By examining these gaps closely, it is determined that there are only 2 such spectrum gaps have sizes that are at least 2.50% of the total spectrum and the widths are 5.90% and 3.67% respectively. In this case, instead of placing the frequency samples at locations that will result in generating significant spectrum gaps as hoped, these larger gaps are instead redistributed into many small spectrum gaps that are unnoticable from the plot when the plot is not zoomed in.

By comparing the results as shown in Fig.3.6 with that from Fig.3.2, it can be observed that the MFI generated array still generate a coarray with low redundancies that resembles a LRLA even when the number of frequency measurements have doubled to 200. Likewise from Fig.3.7, an improvement is observed in the peak side-lobe performance from a value of -9.92 dB when K = 100 to a value of -13.98 dB when K = 200. Also, these results have been reported in [96].

Now, as in the case of the frequency sampling array obtained by SSA algorithm for K = 100, a comparison is also made of the sparse frequency array corresponding to K = 200 to that of an array whose K locations are randomly generated as before. The plot of the ISL result from the MFI generated array versus that of the histogram results obtained from 10000 trials of randomly-spaced array is as shown in Fig.3.8

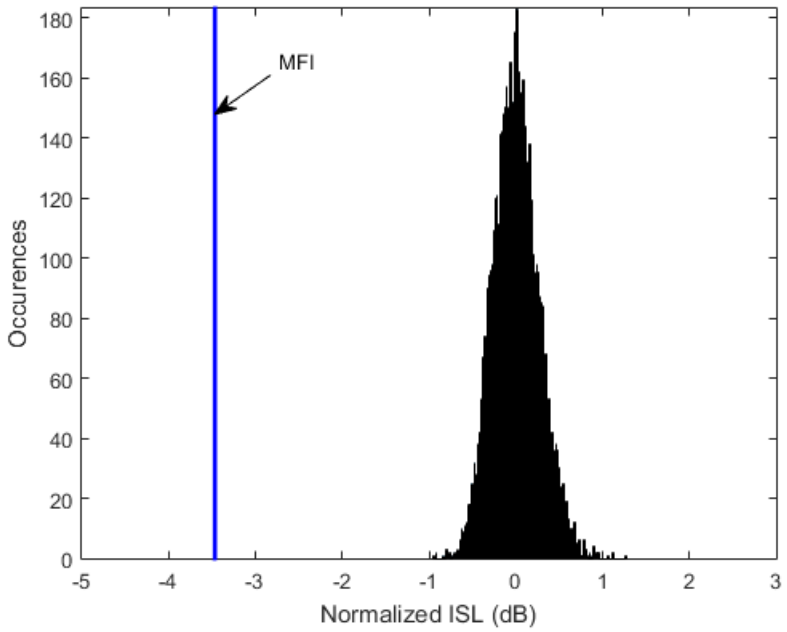

Figure 3.8: ISL value from MFI generated array and randomly-spaced frequency array using K = 200 and 10000 trials

From Fig.3.8 shown above, the computation of the normalized ISL from the randomly-spaced frequency array has a standard deviation of 0.2610 dB. Compared to the normalized ISL result from the MFI generated array whose value is -3.468 dB, this shows that the result from the Sparse

Spectrum Allocation algorithm (MFI based) is 13.2876 standard deviations away from the average value of the randomly-spaced array. Thus, it can be seen that it is still virtually impossible to generate the result obtained using the MFI based algorithm via random permutation even when the spectrum usage has been doubled from 25% to 50%.

After examining the results shown in the previous plots, it can be seen that for the case when 25% of the total original spectrum has been allocated to the radar application based on the SSA algorithm, the resulting PSL performance that is obtained is aorund -9.919 dB. Thus, this prompts the question on whether it is possible to achieve a lower PSL value if the SSA algorithm is to incorporate the PSL value as a second optimization metric besides the using the MFI metric. In order to answer this question, the SSA algorithm is modified to incorporate this change by having the algorithm to switch its optimization metric between MFI and PSL values during the optimization process for a few iterations but eventually settles at the MFI metric until convergence is obtained. At the same time, this switching of the optimization metric may help to prevent the SSA algorithm from getting stuck at local minima points during optimization process due to the fact that the SSA algorithm uses a greedy-search based approach. However, this also means that the computational time required for the algorithm to converge will be extended due to the switching between two optimization metrics.

3.2.2 Construction of Sparse Frequency Array model based on Single Frequency location insertion with mixed MFI/PSL metrics - second adaptation

In this subsection, the modified SSA algorithm with the mixed optimization metric is applied to the first scenario of 25% usage of spectrum. Likewise, this modified algorithm is also applied to the second scenario of 50% of spectrum usage to investigate on whether further improvement to the PSL results obtained earlier for this second scenario can be achiveved as well. The new results

for both scenarios generated by the SSA algorithm with mixed optimization metrices are as shown in Fig. 3.9 - 3.11 and Fig. 3.13 - 3.15 respectively.

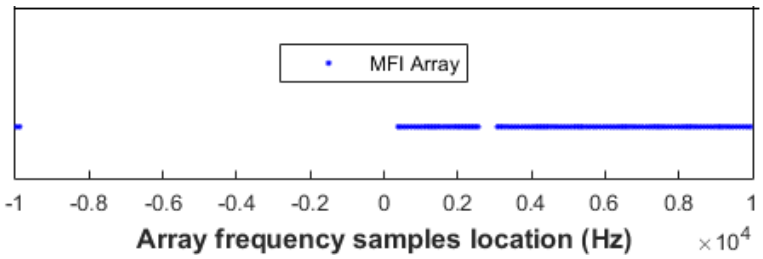

Figure 3.9: Frequency sample locations for Sparse generated array for $K = 100$ using Mixed MFI/PSL metrics

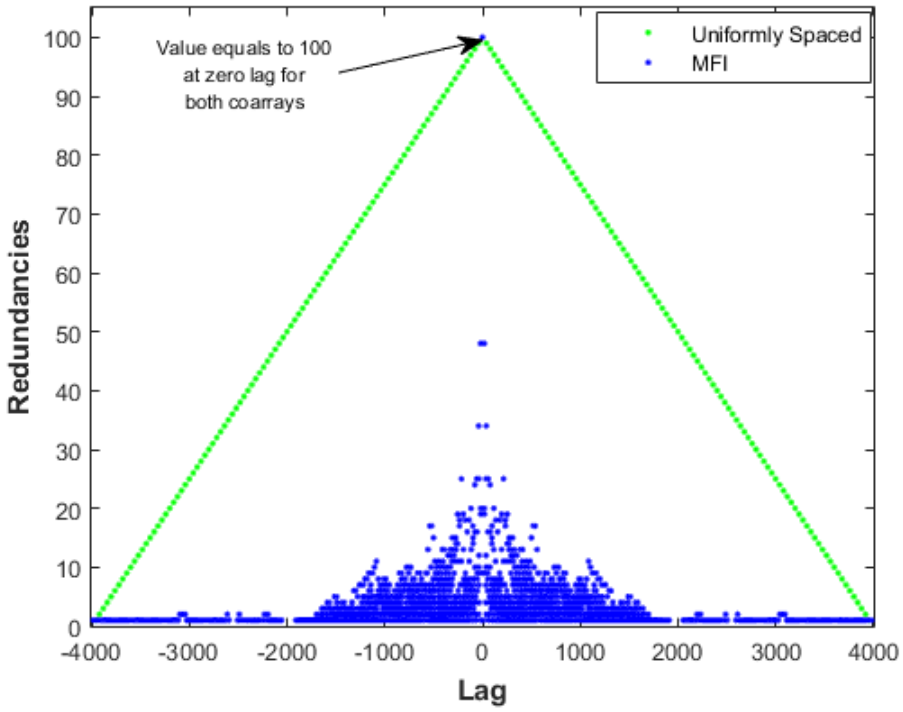

Figure 3.10: Coarrays from using Mixed metrics and Uniformly-spaced frequency array for $K = 100$

From the results obtained for the spectrum usage of 25%, ,as a start, it is observed from Fig.3.9 that the various spectrum gaps of significant sizes as shown in Fig.3.1 have been merged into a single huge spectrum gap as well as a second significant gap while the appearance of the coarray

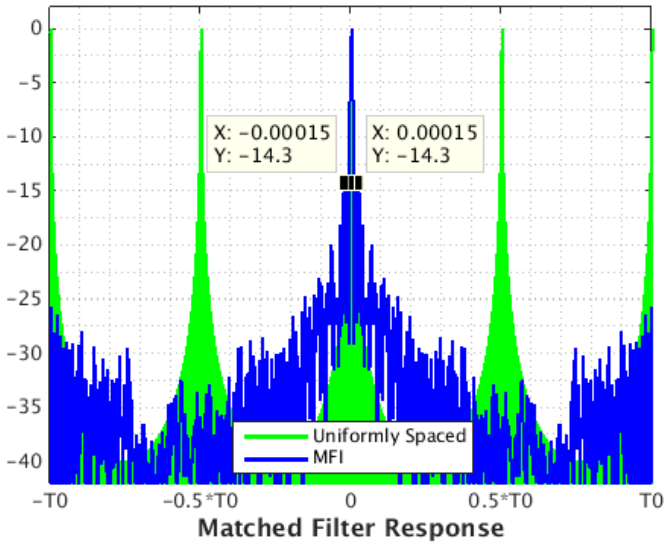

Figure 3.11: Matched Filter Response from using Mixed metrics for $K = 100$

as shown in Fig.3.10 still resembles that of a LRLA.

From Fig.3.11 as shown above, it can be seen that for the same scenario, the modified SSA algorithm incorporating the usage of PSL metric does produces an autocorrelation plot that has possesses a PSL value with a lower value (-14.3 dB) shown in Fig.3.11 as compared to the results (-9.919 dB) obtained from the initial SSA algorithm as shown in Fig.3.3. However, upon closer examination, this improvement of the PSL performance comes at the cost of widening the 3-dB mainlobe by twice its previous amount such that the 3-dB range resolution is now degraded as shown in Fig.3.12. Thus, this new modification does not result in joint improvements of both spectrum usage and PSL value as it only frees up slightly more proportion (aggregated value of 54.025% as combined to 46.85% for gaps of at least 2.5% in spectrum width) of the original spectrum for reallocation at the expense of degrading the 3-dB range resolution by a factor of two.

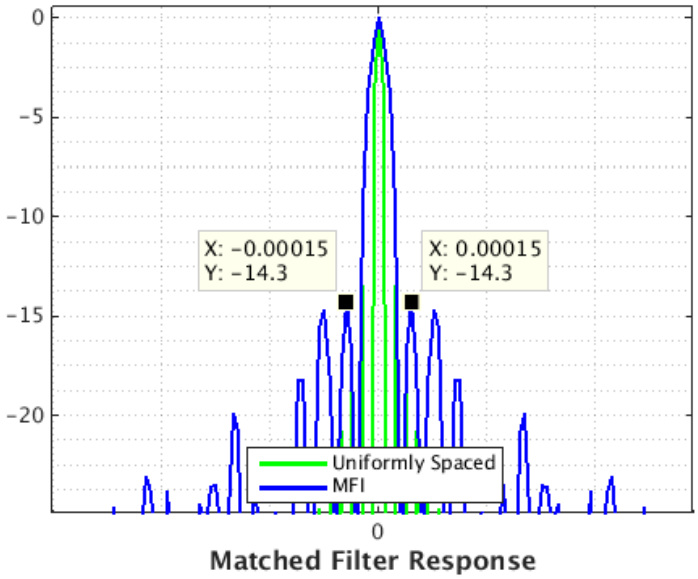

Figure 3.12: Zoom-in of Fig.3.11

Next, the results obtained from applying the modified SSA algorithm using mixed metrics (MFI and PSL) to the second scenario are then shown on the plots showm in Fig. 3.13 - 3.15 below and the subsequent page. An analysis of these results obtained as compared to that of using the original SSA algorithm is also provided as well.

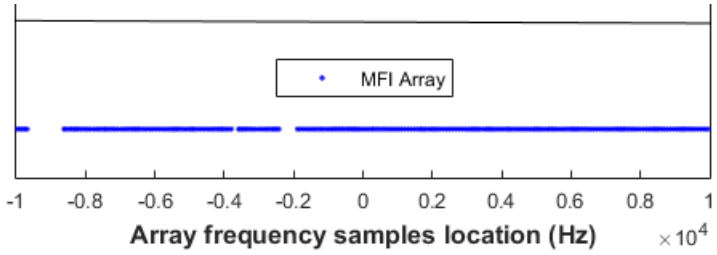

Figure 3.13: Frequency sample locations for Sparse generated array for $K = 200$ using Mixed metrics

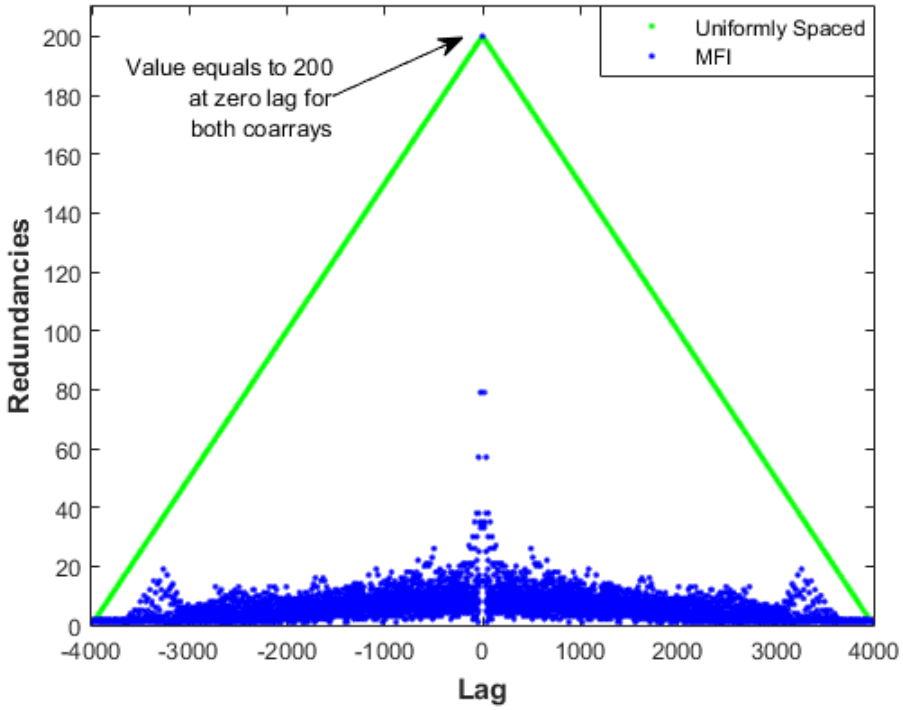

Figure 3.14: Coarrays from using Mixed metrics and Uniformly-spaced frequency array for K = 200

Now, by comparing the results of the PSL value between Fig.3.15 shown on the next page and Fig.3.7 as shown previously for the 50% spectrum usage scenario, it is observed that there is no improvement of the PSL when using the modified SSA algorithm. In fact, there is a slight degradation in both the PSL value (from -13.98 dB to -13.60 dB) as well as the aggregated spectrum size of those generated gaps with sizes greater than 2.50% (from 9.575% to 8.075%) when using the modified SSA algorithm. Therefore, it can be concluded that for the first approach of using single frequency location insertion for the SSA algorithm, the modification of the SSA algorithm to utilize mixed metrices may not be feasible as no overall improvement is noted when using this modification.

At this stage, based on the results obtained using the MFI-based sparse spectrum allocation, it has been shown that it is possible to release spectral contents from the radar application while maintaining the radar range resolution. However, there is a cost/tradeoff to this release of spectrum

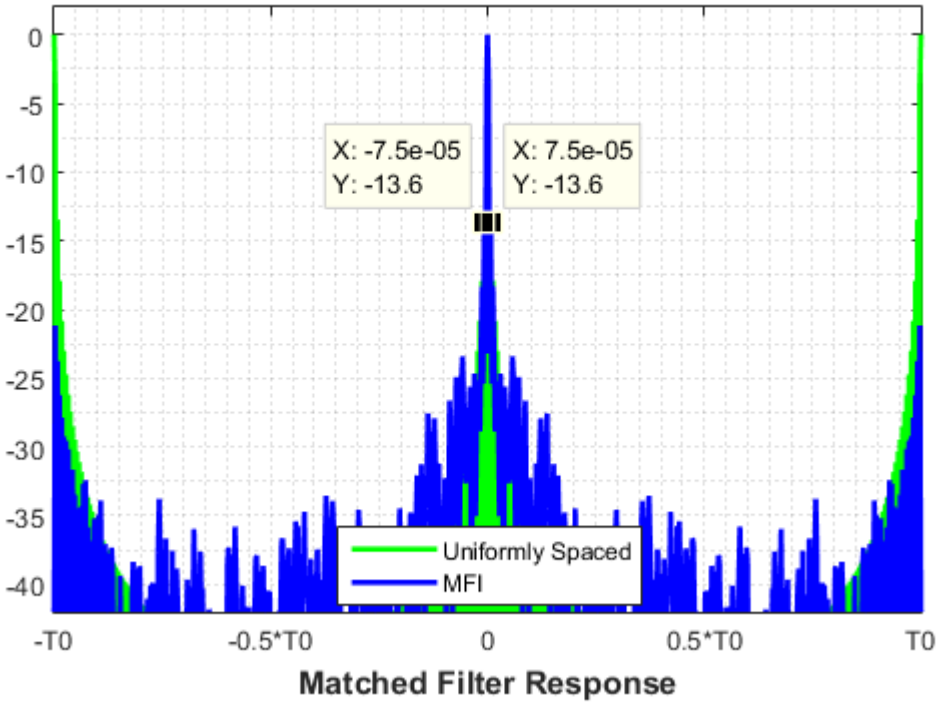

Figure 3.15: Matched Filter Response from using Mixed metrics for $K = 200$

and it comes in the form of degraded ISL and PSL performance when compared to using the full contiguous spectrum band.

Next, besides examining the PSL performance between the two example scenarios of 25% and 50% of spectrum allocation/usage, the amount of spectrum contents that have been released from these two scenarios are also examined. As a start, the first scenario of $K = 100$ coresponding to 25% of spectrum usage by the radar application will be examined. As mentioned previously, by aggregating the eight unallocated spectrum gaps greater than 2.50% of the total spectrum shown in Fig.3.1, it is found that an amount of 46.85% from the total spectrum can be reassigned for another application. If one is to include smaller spectrum gaps into the aggregation as well, this amount can goes higher as the theoretical amount of unused spectrum is 75%.

Following that, the spectrum allocation performance for the second scenario of $K = 200$ is then examined. From the result obtained by aggregating the two unallocated spectrum gaps greater

than 2.50% of the total spectrum as shown in Fig.3.5, this value is a much smaller amount of 9.575% due to the fact that there are many spectrum gaps with sizes of 1.00% or smaller w.r.t. the total spectrum being generated in this second scenario. Thus, the results obtained from the SSA algorithm for the second scenario is less attractive when utilized in a spectrum sharing mode of operation as compared to the first scenario.

Therefore, in order to increase the proportion of spectrum gaps to be made available to other applications for the second scenario as well as further improving the current results for the first scenario, it is proposed that the solution may be achieved by using the second approach of subgrouping these K frequency locations into P smaller groups/blocks of frequencies with each frequency location within a block being spaced apart at the Nyquist sampling interval. The SSA algorithm will then determine the starting location of each of these frequency blocks one block at a time during the optimization process instead of a single frequency sample as in the first approach. The rationale that this approach will generate a larger proportion of spectrum gaps is based on the fact that all the previous non-useful small spectrum gaps (slightly greater than Nyquist sampling interval) generated between adjacent frequency samples will no longer be formed by using the second approach of block insertion.

In the next subsection, we will explore these two example scenarios again by using the results obtained from the second approach to SSA algorithm design while still based on the Sparse Array Perspective.

3.2.3 Construction of Sparse Frequency Array model based on insertion of Frequency Block samples - third adaptation

In the previous subsection, due to the K degrees of freedom that are available when inserting K number of frequency samples into N possible frequency locations via the single frequency location insertion approach, it has resulted in a sparse spectrum allocation that may not always be conducive for spectrum sharing with other systems due to the generation of many small spectrum gaps instead of fewer larger gaps within the total available spectrum. In addition, when considering each single frequency sample as a narrowband coherent transmitter for a physical implementation, this approach will necessiate many transmitters and accompanying RF modules that will be undesirable for a system design point of view.

However, if these K frequency samples are to be grouped into P small blocks of frequency samples with the frequency interval between adjcent samples within each block maintained at Nyquist sampling interval, then it is perceived that it will be less likely for the optimization results to contain many smaller unusable spectrum gaps. The reason is because these K frequency samples are now more tightly coupled together in groups as compared to the previous case where the only requirement is that the frequency interval between samples has to be less than or equal to 100 Hz corresponding to target unambiguous range delay T_0. In addition, by adopting this approach, there are further benefits to be obtained besides the generation of larger spectrum gaps. For a start, as the number of frequency locations to be determined during the optimization process of the SSA algorithm have been reduced from K to the value of $(K \div P)$, this will definitely reduce the computational time of the optimization process as there are less frequency locations to be determined in each iteration. Secondly, from a physical implementation standpoint, there are also now less hardware enough as the system now only requires to have P coherent transmitters as compared to the original K number of transmitters.

Now, with all the potential benefits from the second approach of implementing the SSA algo-

rithm via frequency block insertion (denoted as third adaptation), it give rise to the question of the tradeoff in this approach as compared to the first approach of single frequency sample location insertion. From an optimization point of view, as the Degrees of Freedom (DOF) for searching for the optimal solution has been reduced from K in the first approach to P in the second approach, thus the outcome to be expected is further degradation of both PSL and ISL performance in the final sparse frequency array generated using the second approach as compared to the prior approach. This observation will be verified from the simulation results that are obtained for the two example scenarios of 25% and 50% of spectrum usage.

Before proceeding to discussing the simulation results that are generated based on the second approach, there is an important issue that have to be addressed before the simulations can be performed. This issue is the size of each P block of frequency samples to be designed for the block frequency sample insertion process. Based on a usage of 25% of the available spectrum, one can design each o^{th} block to have a size of 1.00% of the spectrum such that there are a total of 25 optimal starting frequency locations to be allocated for these 25 frequency blocks during each iteration of the optimization process. Alternatively, one can design the spectrum width of each o^{th} block to have a size of 5.00% such that there are only 5 blocks of frequency samples to be considered in each iteration. By basing on inituition, it can be inferred that as the size of each block gets bigger, there will be lesser DOF available in the optimization process and thus the PSL and ISL performance will be further degraded. Similarly, when the size of each block is as small as a single frequency sample, the results obtained from the second approach of block frequency sample insertion will converge exactly to that of the first approach of using single frequency location insertion.

As a start, the plots of the frequency sample locations and coarrays for K = 100 samples (25% utilization of total bandwidth) obtained using the second approach of the SSA algorithm with a block size of 0.50%, i.e. 2 frequency samples per block is shown in Fig. 3.16 - 3.18. This also means that there are a total of 50 frequency blocks to be inserted corresponding to the spectrum usage of 25%.

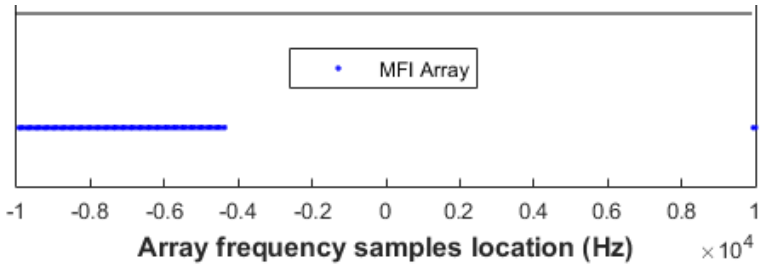

Figure 3.16: Frequency sample locations for blocksize of 0.50% (first scenario)

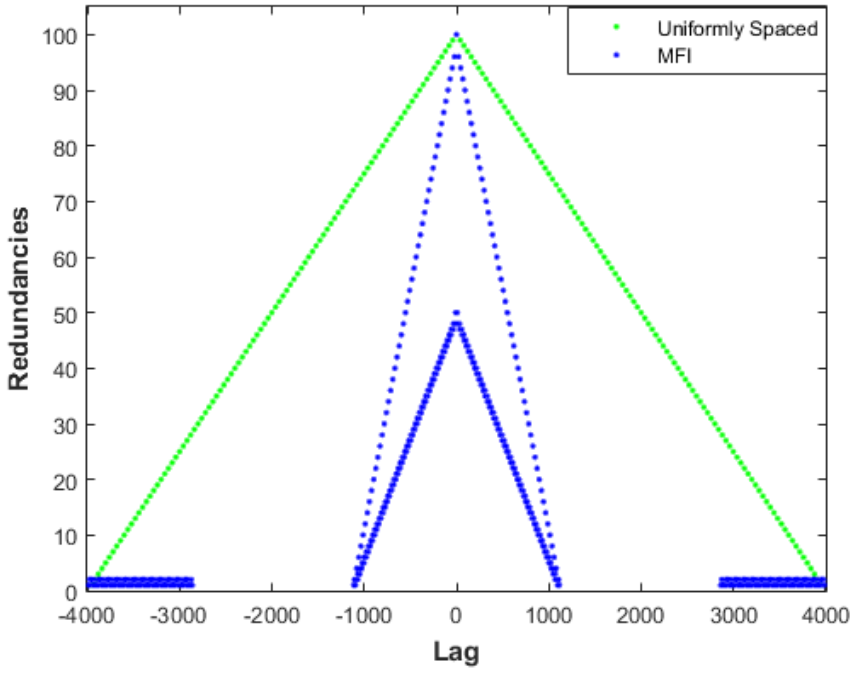

Figure 3.17: Coarrays from MFI generated array versus Uniformly-spaced frequency array for blocksize of 0.50%

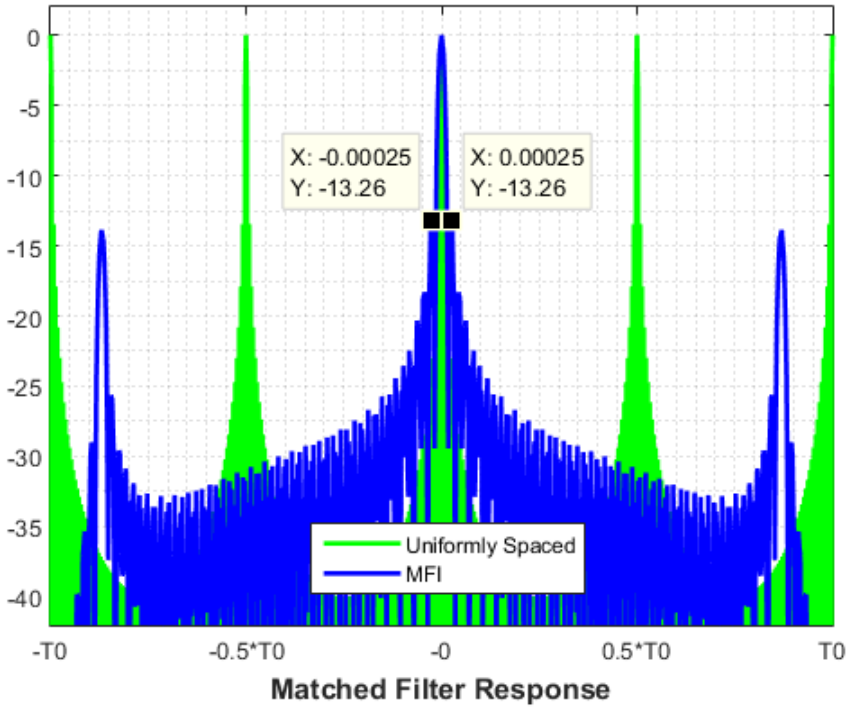

Figure 3.18: Matched Filter Response using MFI generated array for blocksize of 0.50%

By examining both Fig. 3.16 and Fig. 3.18, the first observation is that both the PSL performance as well as the spectrum gap that is generated using this approach have improved greatly as compared to using the first approach or equivalently, using a blocksize with just 1 frequency sample. Also, it is interesting to observe that the block-based insertion SSA algorithm has placed only one frequency block at the upper end of the spectrum whereas the remaining 49 frequency blocks are placed at the other end of the spectrum. However, as in the case obtained with using the SSA algorithm with mixed metric implementation denoted as the second adaptation, this comes at the cost of widening the mainlobe resolution by 3.75 times or in terms of 3-dB range resolution, it is degraded by a factor of 3.75 as observed in Fig. 3.19 on the following page. Furthermore, by observing the coarray generated using this 0.50% blocksize, it seems that the optimization process is stuck in some local minima and thus the appearance of the coarray borne some resemblance to that of an uniformly-spaced frequency array (USFA) rather than a LRLA. At this point, no conclusion is drawn between any correlation of the frequency block size to the likelihood of the SSA

algorithm being stuck in local minima during optimization until more combination of results are presented.

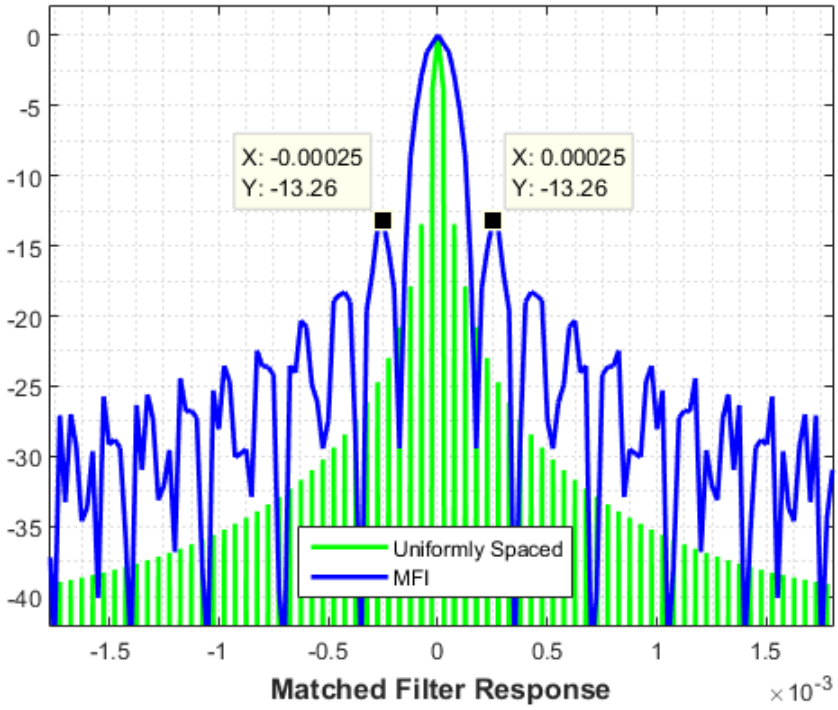

Figure 3.19: Zoom-in of Fig. 3.18

Next, the simulations are then performed with each frequency block varying with size percentage of [1.00, 1.25, 2.50 and 5.00] respectively. Based on the simulation results obtained from these various sizes, it is observed that with the exception of using the block size of 1.25%, the MFI based frequency arrays using the other blocksizes do not possess coarrays that resembles a LRLA but rather to that of an USFA. To illustrate these observations, the plots of the frequency sample locations and coarrays corresponding to both 1.00% and 2.50% sized frequency blocks are shown in Fig. 3.20 - 3.23 as examples.

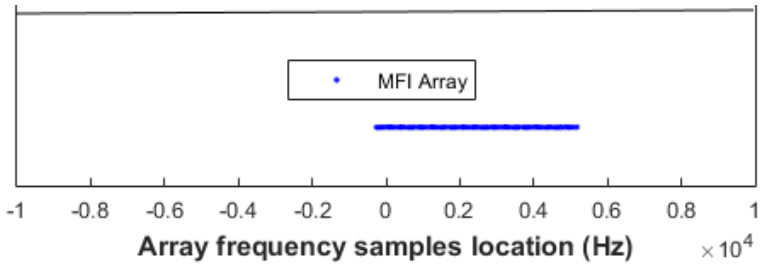

Figure 3.20: Frequency sample locations for blocksize of 1.00% (first scenario)

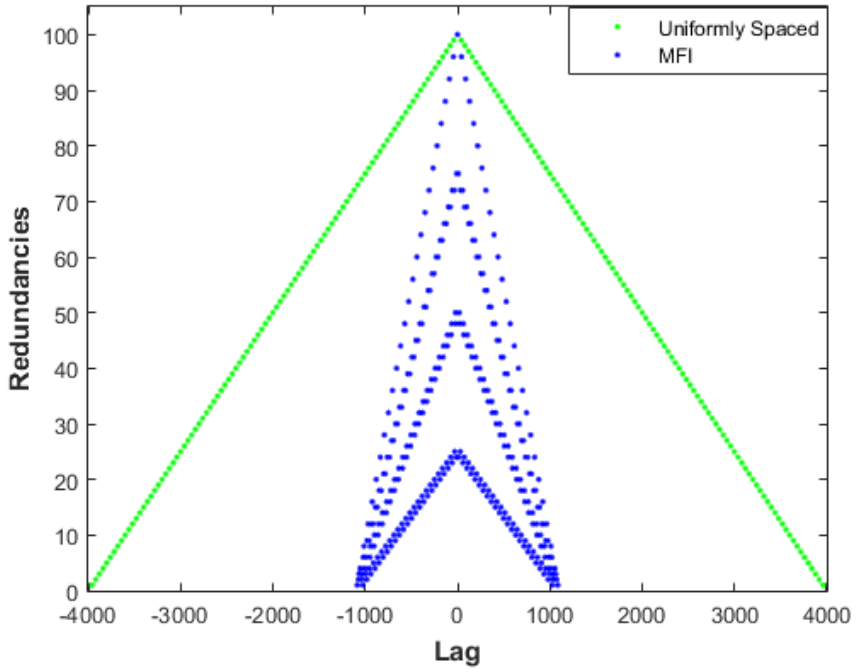

Figure 3.21: Coarrays from MFI generated array versus Uniformly-spaced frequency array for blocksize of 1.00%

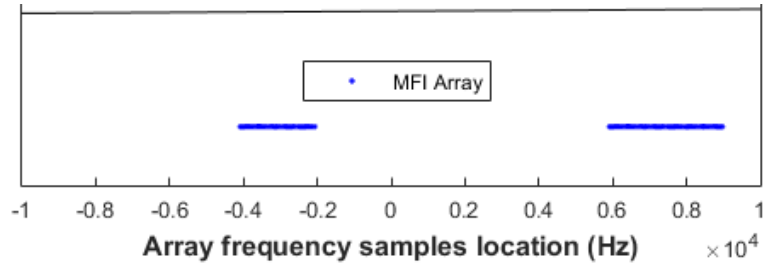

Figure 3.22: Frequency sample locations for blocksize of 2.50% (first scenario)

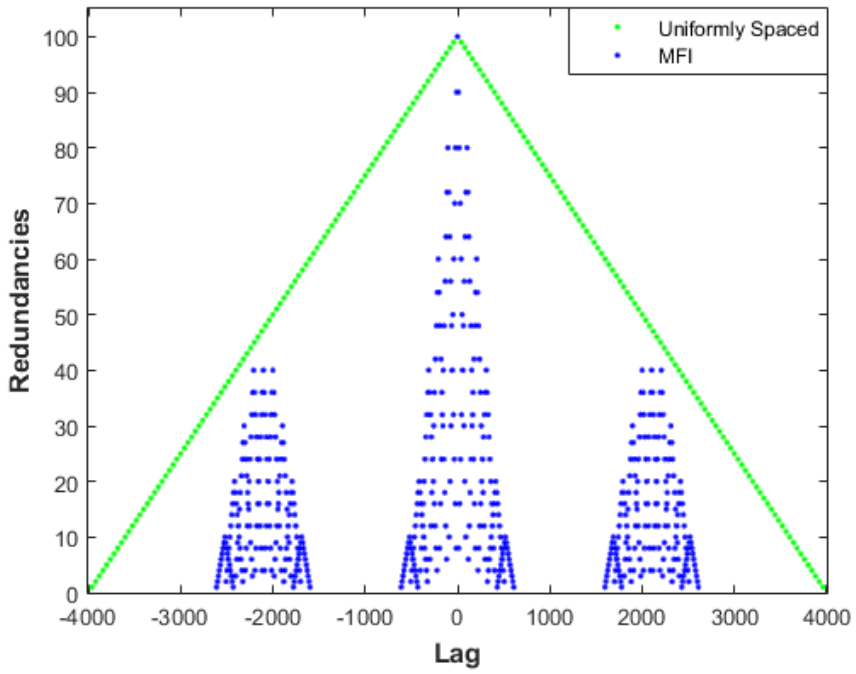

Figure 3.23: Coarrays from MFI generated array versus Uniformly-spaced frequency array for blocksize of 2.50%

Following the plots for both 1.00% and 2.50% sized frequency blocks which shows strong resemblance to an USFA, the plots corresponding to the frequency block size of 1.25% are as shown in Fig. 3.24 - 3.26. For this set of results, the coarray structure obtained from using this frequency block size bears slightly more resemblance to a LRLA as compared to the other combinations.

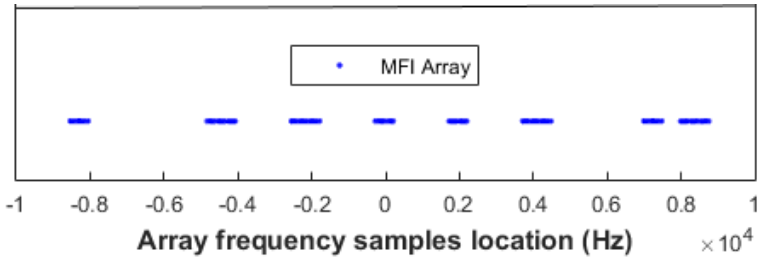

Figure 3.24: Frequency sample locations for blocksize of 1.25% (first scenario)

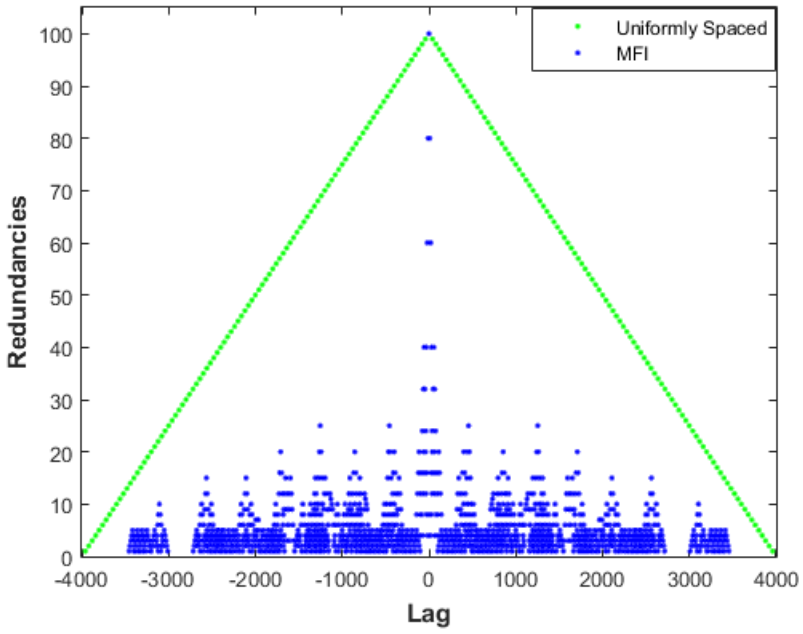

Figure 3.25: Coarrays from MFI generated array versus Uniformly-spaced frequency array for blocksize of 1.25%

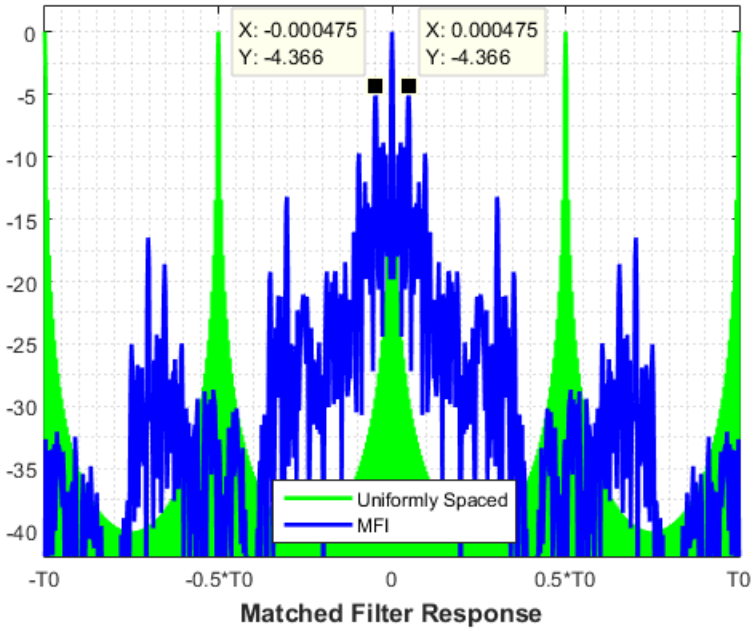

Figure 3.26: Matched Filter Response using MFI generated array for blocksize of 1.25%

By examinining the plots generated using the second approach of the SSA algorithm via frequency block insertion for the first example scenario, one deduction that can be made is that the greedy-search based optimization process may be stuck in some local minima for this approach when only the MFI measure is used as the metric of optimization for this greedy-based search algorithm. Also, this deduction is based on the facts that the coarrays obtained from these optimized sparse frequency arrays bear strong resemblances to a USFA. If it is indeed true that the algorithm is stuck in local minima, then it will not have achieved the best possible results in terms of sidelobe and spectrum reallocation performance.

However, for the case when the frequency blocksize is set to 1.25% of the total spectrum, the corresponding coarray bears lesser resemblance to an USFA and more of a LRLA. Next, by further examining Fig. 3.24 corresponding to this blocksize whose coarray exhibits a more LRLA structure, it can be seen that the grouping of frequency samples does help to further increase the amount of spectrum content to be allocated for other systems (around 74.0% for gaps of at least 2.50% in spectrum width) as compared to using the single frequency location insertion (around 46.85%) in the first approach. Also, this improvement is achieved with only a degradation factor of 1.20 for the 3-dB range resolution. However, the main tradeoff for this choice of blocksize comes at the expense of a worsening PSL value from a previous value of -9.919 dB for the first approach to a current value of -4.366 dB for this approach.

Thus, as mentioned above, in order to avoid getting stuck at the local minima during optimization, it may be necessary to implement the SSA algorithm with frequency block insertion using the mixture of MFI/PSL metrices as was introduced in the previous section. However, before showing the results of this hypothesis in the next subsection, simulations for varying frequency blocksizes of [0.50, 1.00, 1.25, 2.50, 5.00] percentage are repeated for the second scenario of 50% spectrum usage using just the MFI metric. Again, the results obtained by using a frequency blocksize of 0.50% (100 such blocks for 50% spectrum usage) are first shown in Fig. 3.27 - 3.29 for discussion. Subsequently, the results obtained by using the other frequency blocksizes will be shown for

comparison with the results obtained from the first scenario.

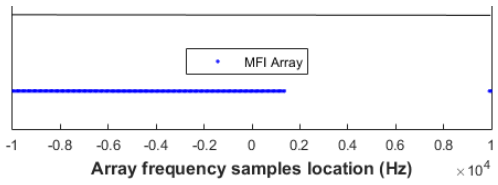

Figure 3.27: Frequency sample locations for blocksize of 0.50% (second scenario)

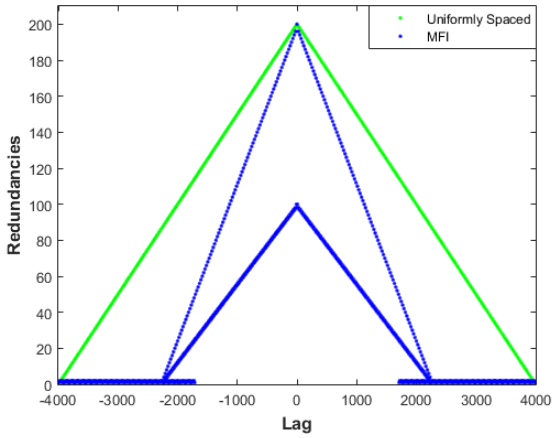

Figure 3.28: Coarrays from MFI generated array versus Uniformly-spaced frequency array for blocksize of 0.50%

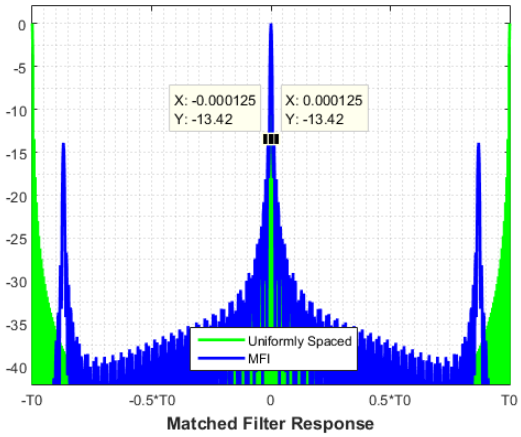

Figure 3.29: Matched Filter Response using MFI generated array for blocksize of 0.50%

By comparing the plots shown in Fig. 3.27 - 3.29. with that from Fig. 3.16 - 3.18, it can be seen that the same trend is observed in the second scenario for the case of using a frequency blocksize of 0.50%. As the SSA algorithm has again place only a single frequency block at the upper end of the spectrum, thus this results in a degradation of the range resolution by a factor of 1.75 as shown in Fig. 3.30 below and the structure of the coarray also bears close similarity to that from an uniformly-spaced frequency array (USFA). Also, the results obtained for using a frequency blocksize of 0.50% again indicates that the optimization process may be stuck at a local minima as is the case of the previous scenario.

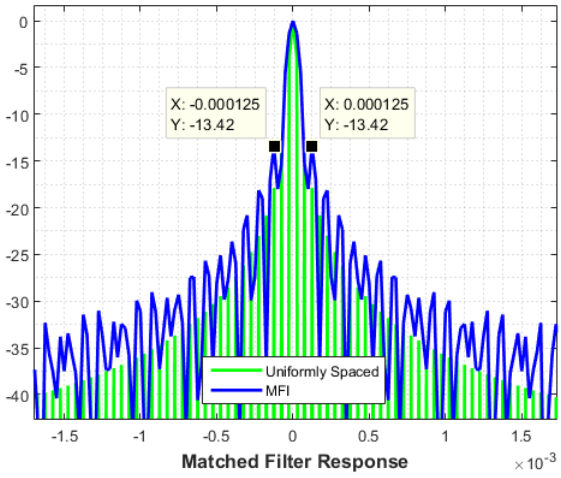

Figure 3.30: Zoom-in of Fig. 3.29

Next, the simulation results obtained from the other blocksizes are shown in the following plots. Interestingly, the resulting frequency arrays obtained from block sizes of 1.00% and 1.25% bear strong similarity to that of a LRLA unlike the case for the first scenario. However, for the larger frequency blocksizes, the corresponding frequency arrays again borne stronger resemblances to that of an USFA. To illustrate this point, the plots of the frequency sample locations and coarrays corresponding to both 1.00%, 1.25% and 2.50% sized frequency blocks are as shown in Fig. 3.31 - 3.36.

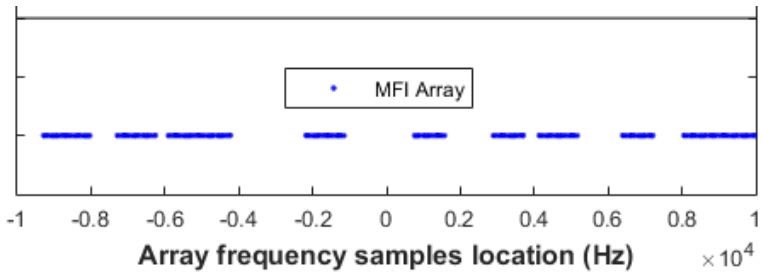

Figure 3.31: Frequency sample locations for blocksize of 1.00% (second scenario)

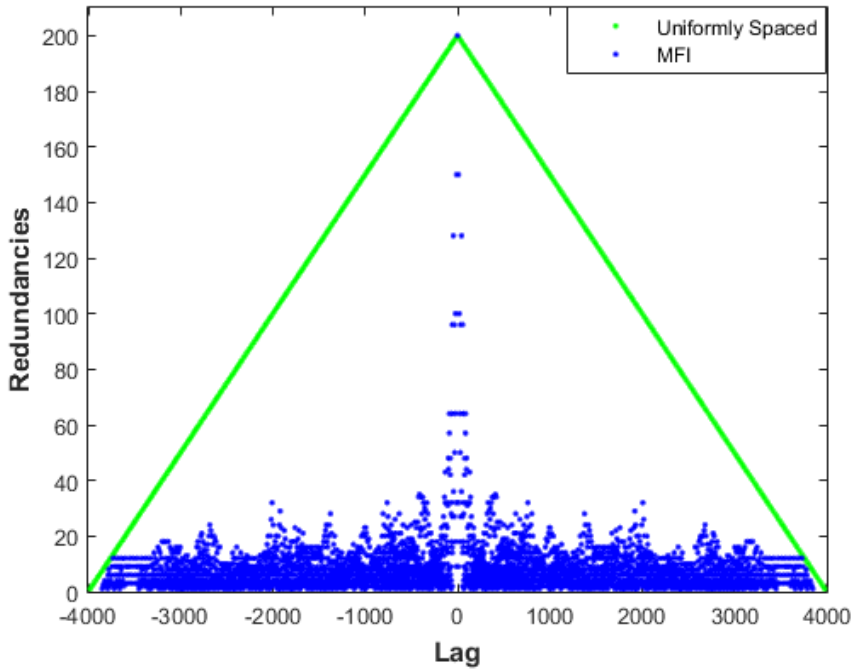

Figure 3.32: Coarrays from MFI generated array versus Uniformly-spaced frequency array for blocksize of 1.00%

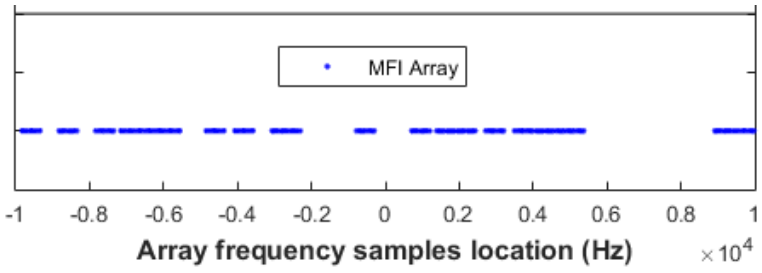

Figure 3.33: Frequency sample locations for blocksize of 1.25% (second scenario)

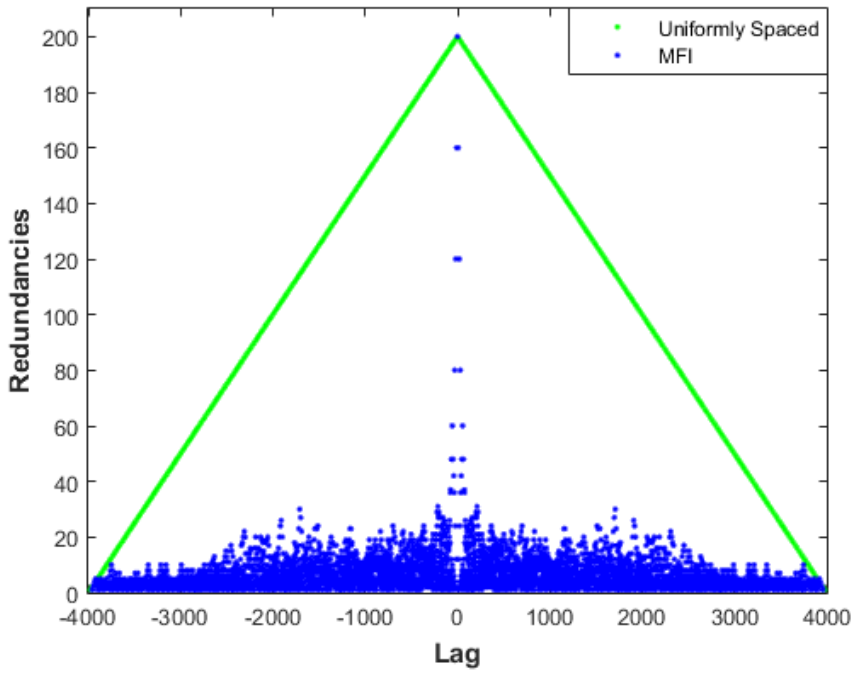

Figure 3.34: Coarrays from MFI generated array versus Uniformly-spaced frequency array for blocksize of 1.25%

By examining Fig. 3.31 and Fig. 3.33 corresponding to the frequency blocksizes of 1.00% and 1.25%, the first observation is that there are now many more significant spectrum gaps present in the MFI based frequency arrays generated by the SSA algorithm using frequency block-based insertion as compared to when using single frequency sample-based insertion. In fact, by performing an aggregation fo those spectrum gaps using the criteria that each gap size should be larger than 2.50% of the total spectrum, the values obtained are 40.675 % and 41.875% of the total spectrum for frequency blocksize of 1.00% and 1.25%. These results for the second example scenario indicate a huge improvement from that previously obtained by using single frequency location insertion where the best possible aggregated value of unallocated spectrum gaps using the same criteria amounts to only 9.575%. The second observation made is that both coarrays corresponding to the two frequency block sizes bear more resemblances to a LRLA rather than that of an USFA. This resemblance to a LRLA may explain the reasons behind the huge improvements obtained as this is an indication that the optimization process is not stuck in some local minima as was in the

case of the first scenario. Nevertheless, these improvments come with worsening PSL performance with the PSL values being -8.89 dB and -11.39 dB for 1.00% and 1.25% frequency blocksizes as shown in Fig. 3.37 - 3.38 as compared to the value of -13.98 dB when using single sample-based insertion approach. Most important of all, the 3-dB range resolution is maintained when using these two frequency block sizes compared to when using the full spectrum.

Next, by examining Fig. 3.35 - 3.36 below and on the next page corresponding to a frequency blocksize of 2.50%, it can be observed that the appearance of both the frequency array and its coarray falls in-between a LRLA and an USFA structure. Also, for this MFI generated frequency array, the aggregated amount of spectrum content that can be reallocated is still a useful value of 48.75% of the total spectrum at the expense of a degradation factor of 1.20 for the 3-dB range resolution as well as a worsening PSL value of -6.29 dB as shown in Fig. 3.39.

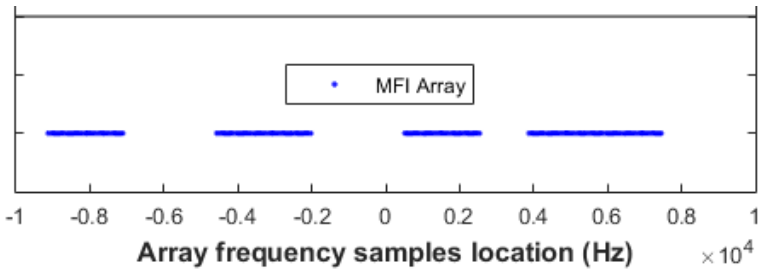

Figure 3.35: Frequency sample locations for blocksize of 2.50% (second scenario)

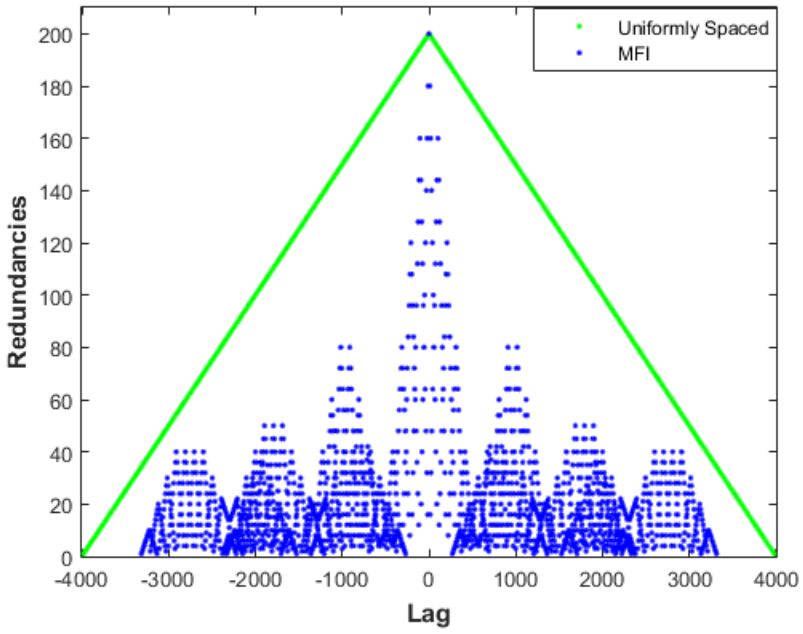

Figure 3.36: Coarrays from MFI generated array versus Uniformly-spaced frequency array for blocksize of 2.50%

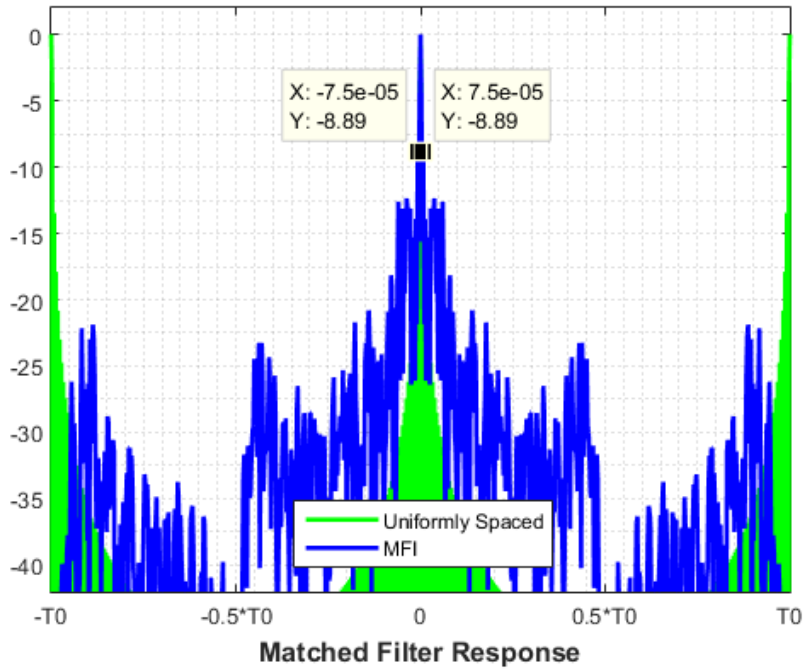

Figure 3.37: Matched Filter Response using MFI generated array for blocksize of 1.00%

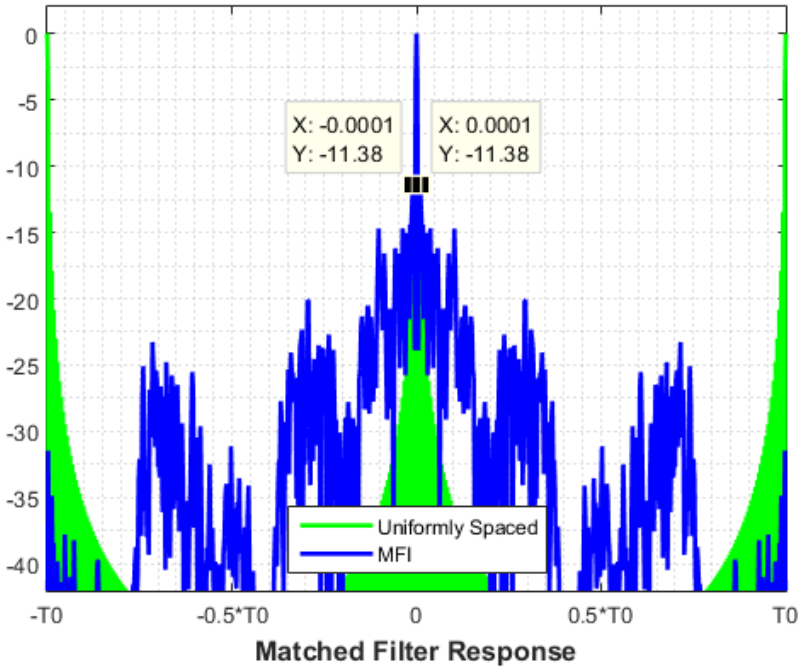

Figure 3.38: Matched Filter Response using MFI generated array for blocksize of 1.25%

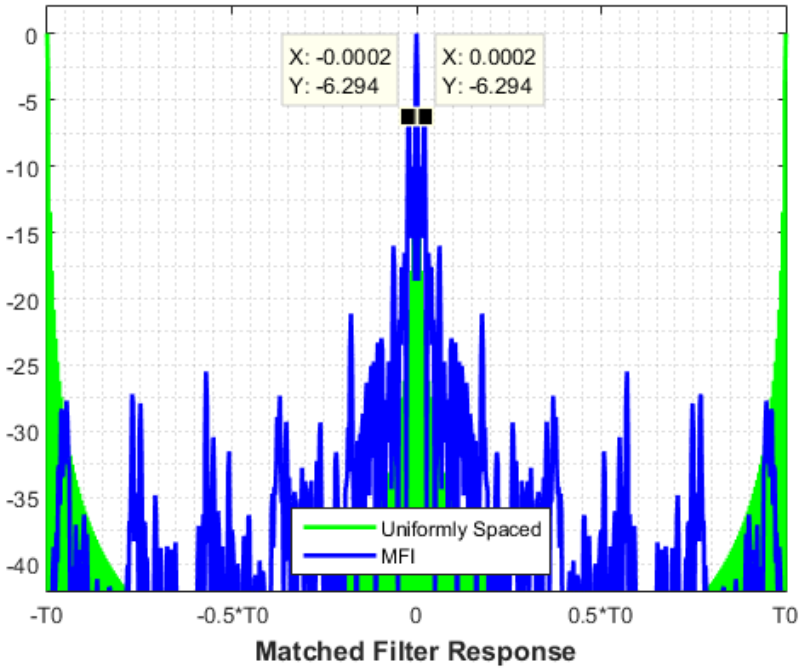

Figure 3.39: Matched Filter Response using MFI generated array for blocksize of 2.50%

As mentioned previously based on the general observation of the results obtained from the first scenario, a hypothesis was formed which states that it may be necessary to implement the SSA algorithm with frequency block insertion using mixed MFI/PSL metrices in order to avoid the algorithm from getting stuck at the local minima during optimization. The only exception to the trend is the case of using the frequency blocksize of 1.25% where the corresponding coarray of the optimized sparse frequency array borne some resemblances to a LRLA.

Now, for the second scenario, the co-array results obtained from using frequency blocksizes of 0.50%, 2.50% and 5.00% etc. again appear to resemble more closely to an USFA as well and thus provides more support to this hypothesis. The exception of this trend comes from using frequency blocksizes of 1.00% and 1.25% in which the appearance of both MFI generated frequency arrays and coarrays shows more resemblances to a LRLA instead. Based on the results from these two scenarios, the modified SSA algorithm with mixed MFI/PSL metrices which was implemented in the previous subsection for single frequency sample-based insertion is applied to these two scenarios when using frequency block-based insertion along with the same frequency blocksizes of [0.50, 1.00, 1.25, 2.50, 5.00] percent accordlingly. The results obtained from the modified SSA algorithm will be shown and discussed in the next subsection starting from the first scenario.

3.2.4 Construction of Sparse Frequency Array model based on insertion of Frequency Block samples with mixed MFI/PSL metrics - fourth adaptation

In this subsection, the frequency-block based SSA algorithm with the mixed optimization metric is applied to both scenarios of 25% and 50% usage of spectrum. The objective in this subsection is to demonstrate on the validity of the hypothesis which states that it is necessary to implement the frequency-block based SSA algorithm with mixed MFI/PSL metrics in order to avoid from getting stuck at the local minima during optimization. This is essential as by avoiding getting stuck in a local minima, the results obtained may exhibit better sidelobe performance as well as more

reusable spectrum for reallocation. As a start, the results for the first scenario generated by this SSA algorithm adaptation using frequency blocksizes of percentage [0.50, 1.00, 1.25, 2.50, 5.00] are shown starting with the usage of the blocksize of 0.50%. Also, following the results obtained from the first scenario, the results obtained from the second scenario will be shown accordingly.

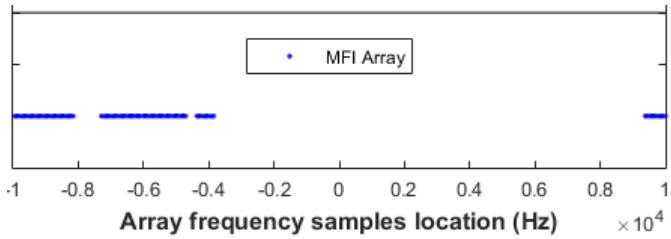

Figure 3.40: Frequency sample locations for blocksize of 0.50% using Mixed metrics (first scenario)

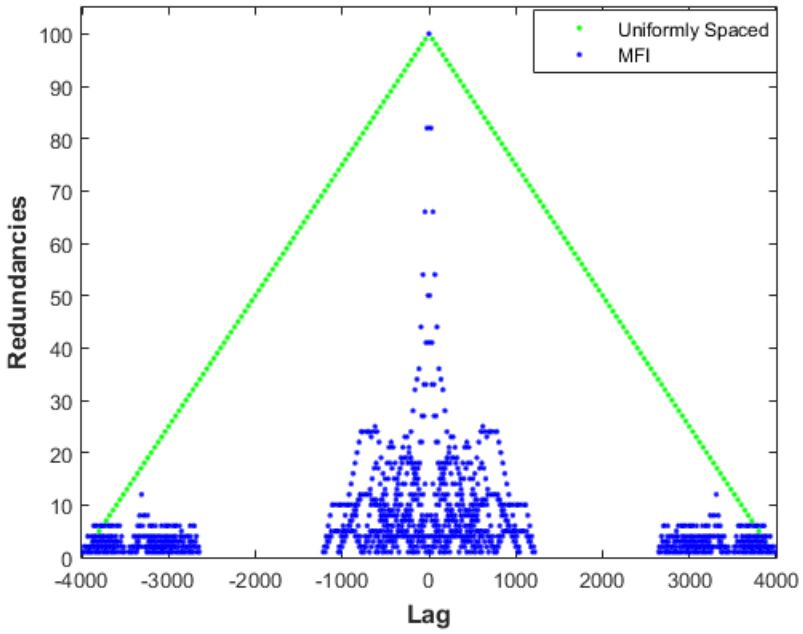

Figure 3.41: Coarrays from using Mixed metrics versus Uniformly-spaced frequency array for blocksize of 0.50%

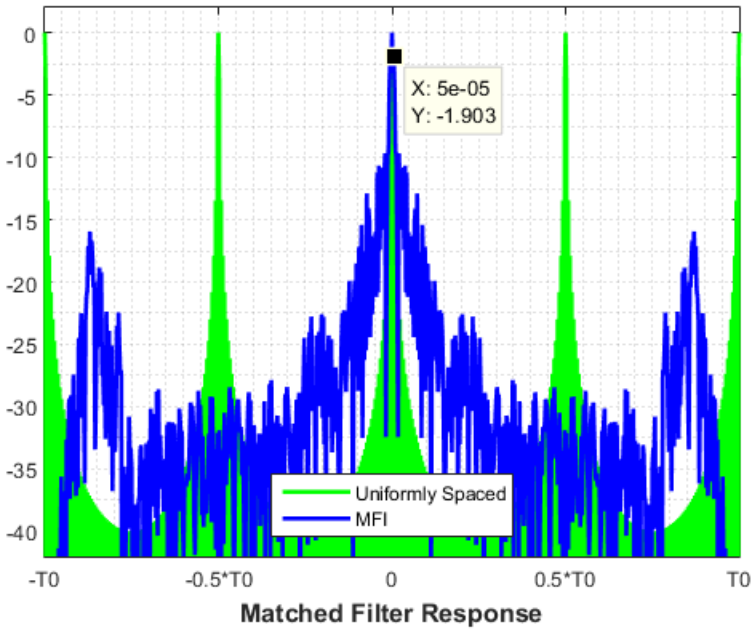

Figure 3.42: Matched Filter Response from using Mixed metrics for blocksize of 0.50%

By comparing Fig. 3.40 - 3.42 generated using the mixed MFI/PSL metric to that of Fig. 3.16 - 3.18 generated using just the MFI metric, it is seen that the newer results obtained using the mixed metric do bear more resemblance to a LRLA unlike the previous results of using just the MFI metric. Also, the aggregated value of the significant-sized spectrum gaps for reallocation in this new sparse-frequency array is only slightly worst off at a value of 70.60% compared to the previous value of 71.58%. Furthermore, closer examination of the matched filter response obtained with the new frequency array as shown in Fig. 3.43 reveals that it still retains the same 3-dB range resolution degradation of 3 times as before when both are compared to using full contiguous spectrum. In addition, by further examining the Matched Filter response, it is seen that there is a shoulder-lobe artefact generated around the mainlobe which causes the PSL value to be mistakenly declared as -1.903 dB due to this shoulder-lobe.

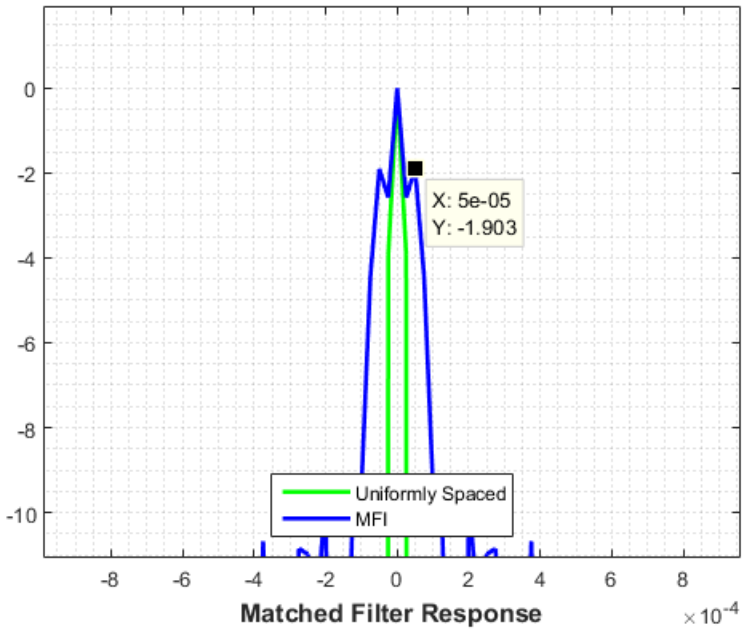

Figure 3.43: Zoom-in of Fig. 3.42

Next, the results of both sparse frequency arrays and their corresponding coarrays obtained from using blocksizes of [1.00, 1.25, 2.50, 5.00] are shown in Fig. 3.44 - 3.51, followed by some of their matched filter responses as shown in Fig. 3.52 - 3.53. From these results obtained as compared to that from Fig. 3.16 - 3.25, the mixed metric implementation does results in sparse frequency arrays showing more resemblances to a LRLA. Thus, these results support the hypothesis made with respect to using mixed metric for block-based implementation of the SSA algorithm.

Besides the task of validating the hypothesis on using mixed metric implementation to prevent the optimization process from being stuck in local minimas, the next step is to determine whether there is any performance improvement in terms of spectrum content for reallocation as well as sidelobe levels. By examining the plots of frequency sample locations obtained from using both implementations, the results indicate that both generate around 70% of reusable spectrum for reallocation. However, by examining the corresponding matched filter responses, it is found that the sidelobe performance (both PSL and ISL) obtained from mixed metric implementation are worst off in general than that from solely MFI-based implementation. One main reason for this degrada-

tion is due to the presence of high shoulder-lobe artefacts that can be seen in Fig. 3.43 and 3.53. At the same time, the presence of these artefacts may provide a false impression that the 3-dB range resolution is preserved but in reality they exhibit 3-dB range resolution degradation in excess by a factor of 3.75 as seen previously when only the MFI metric is used.

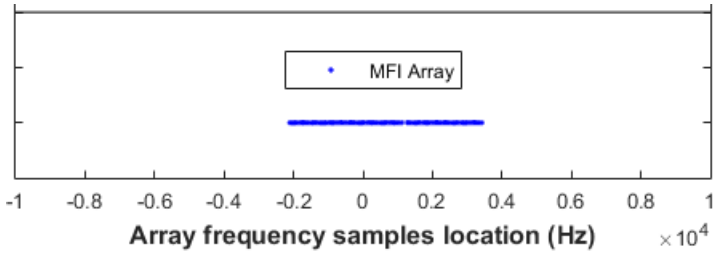

Figure 3.44: Frequency sample locations for blocksize of 1.00% using Mixed metrics (first scenario)

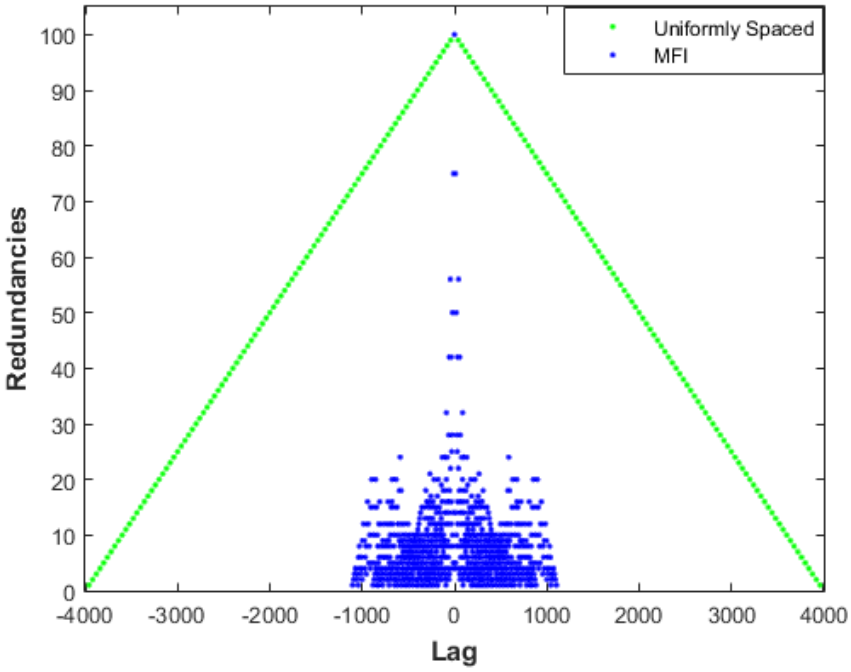

Figure 3.45: Coarrays from using Mixed metrics versus Uniformly-spaced frequency array for blocksize of 1.00%

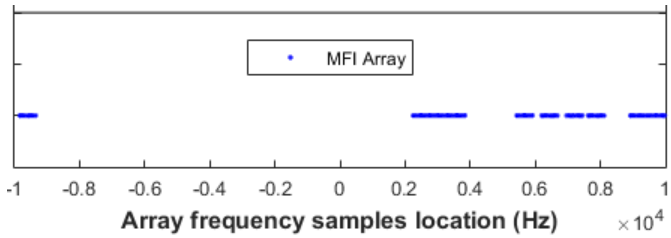

Figure 3.46: Frequency sample locations for blocksize of 1.25% using Mixed metrics (first scenario)

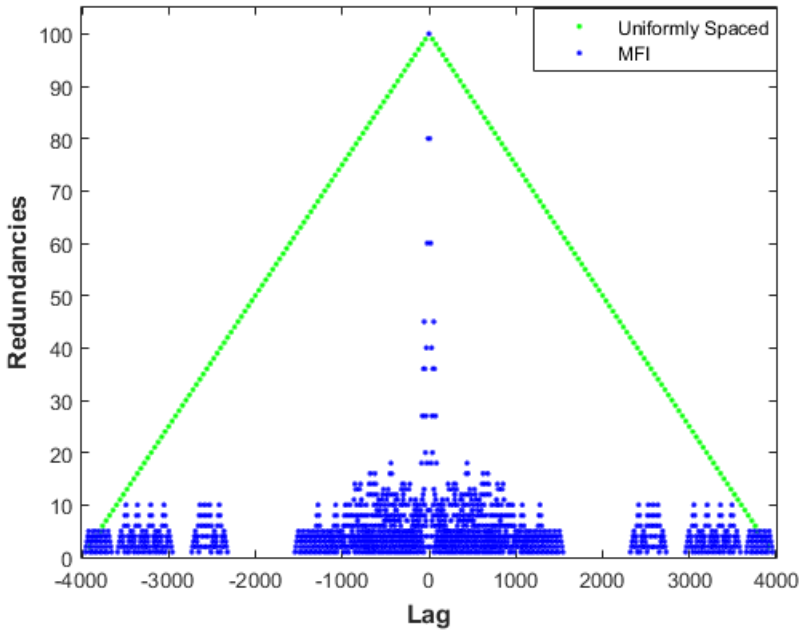

Figure 3.47: Coarrays from using Mixed metrics versus Uniformly-spaced frequency array for blocksize of 1.25%

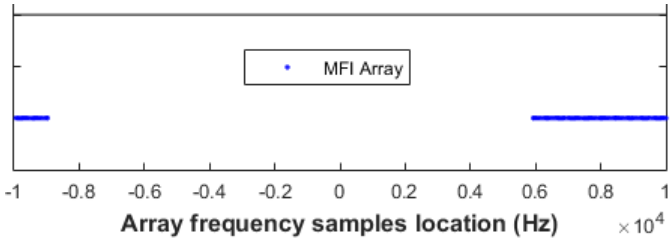

Figure 3.48: Frequency sample locations for blocksize of 2.50% using Mixed metrics (first scenario)

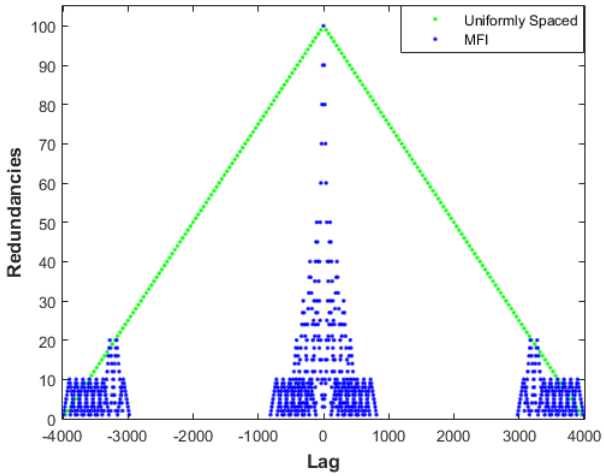

Figure 3.49: Coarrays from using Mixed metrics versus Uniformly-spaced frequency array for blocksize of 2.50%

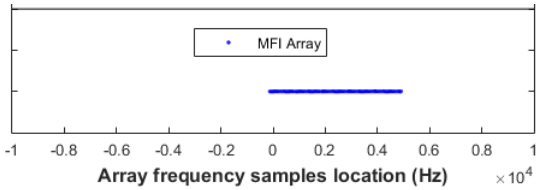

Figure 3.50: Frequency sample locations for blocksize of 5.00% using Mixed metric (first scenario)

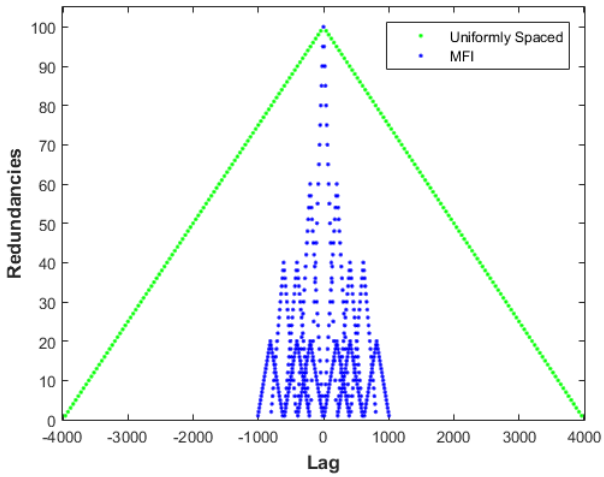

Figure 3.51: Coarrays from using Mixed metrics versus Uniformly-spaced frequency array for blocksize of 5.00%

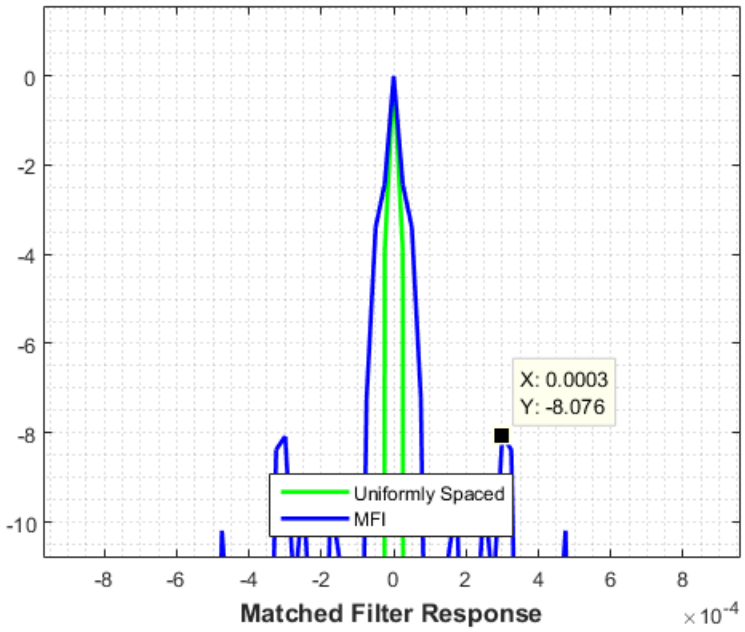

Figure 3.52: Zoom-in of Matched Filter Response using Mixed metrics for blocksize of 1.25%

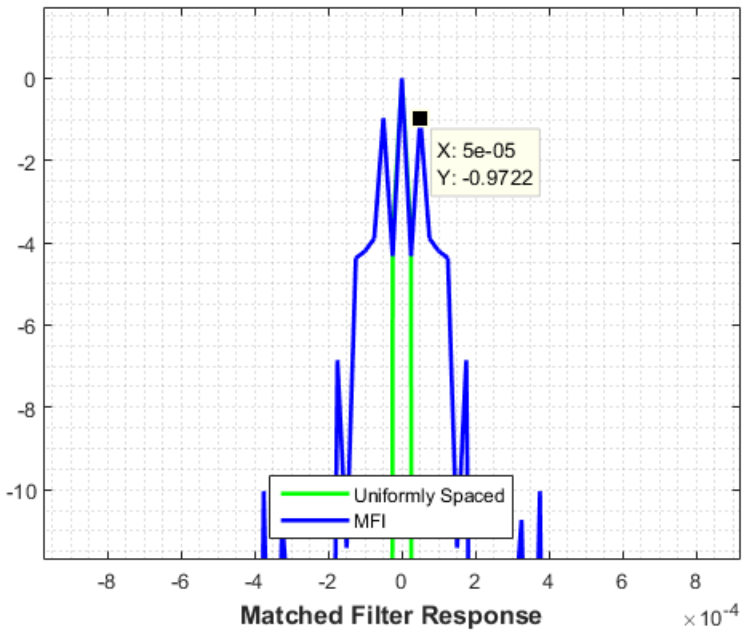

Figure 3.53: Zoom-in of Matched Filter Response using Mixed metrics for blocksize of 2.50%

After examining the results for the first scenario, the results obtained from the second scenario starting with the frequency blocksize of 0.50% are shown in Fig. 3.54 - 3.56 and followed by that

from the other frequency blocksizes as shown in Fig. 3.57 - 3.64.

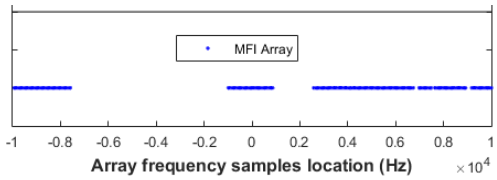

Figure 3.54: Frequency sample locations for blocksize of 0.50% using Mixed metrics (second scenario)

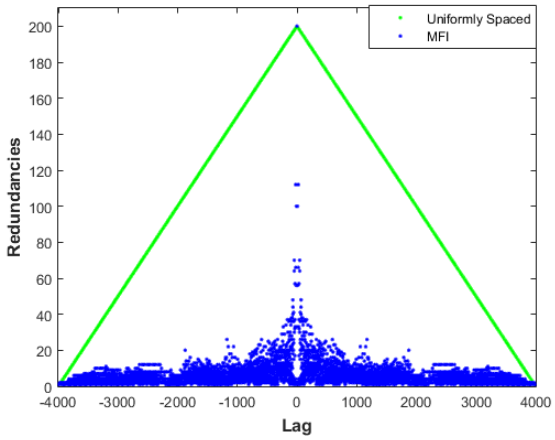

Figure 3.55: Coarrays from using Mixed metrics versus Uniformly-spaced frequency array for blocksize of 0.50%

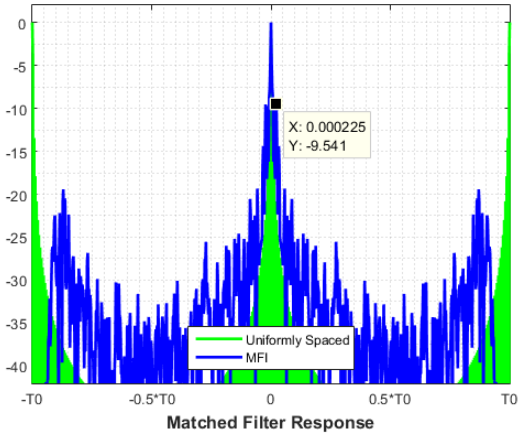

Figure 3.56: Matched Filter Response using Mixed metrics for blocksize of 0.50%

By comparing Fig. 3.54 - 3.56 generated using the mixed MFI/PSL metrics implementation to that of Fig. 3.27 - 3.29 generated using just the MFI metric for the 0.50% frequency block size, it is seen that the newer results obtained using this implementation is now more closer to a LRLA compared to the previous results of using solely the MFI metric. Also, for this more LRLA-like frequency array, the aggregated value of all significant-sized spectrum gaps produces a value of 41.58% of reallocatable spectrum as compared to 42.83% previously in Fig. 3.27. Furthermore, a zoom-in examination of the matched filter response obtained with the new result reveals that it is able to remove the 3-dB range resolution degradation from a previous factor of 2.00 to no degradation when both cases are compared to using the full contiguous spectrum.

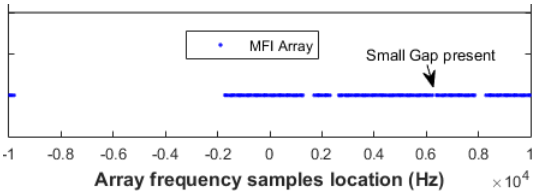

Figure 3.57: Frequency sample locations for blocksize of 1.00% using Mixed metrics (second scenario)

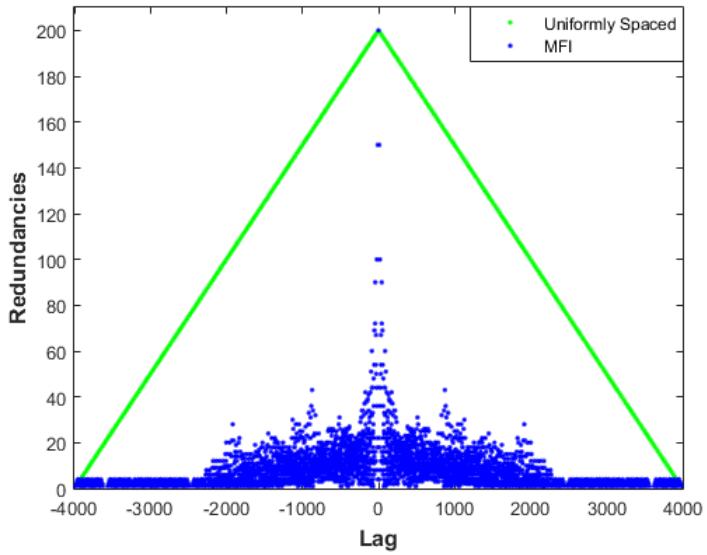

Figure 3.58: Coarrays from using Mixed metrics versus Uniformly-spaced frequency array for blocksize of 1.00%

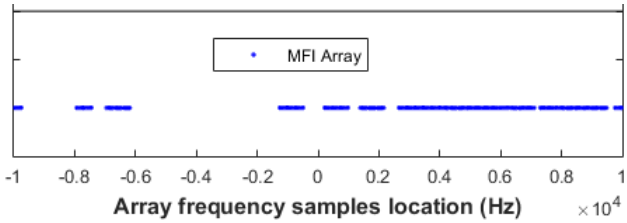

Figure 3.59: Frequency sample locations for blocksize of 1.25% using Mixed metrics (second scenario)

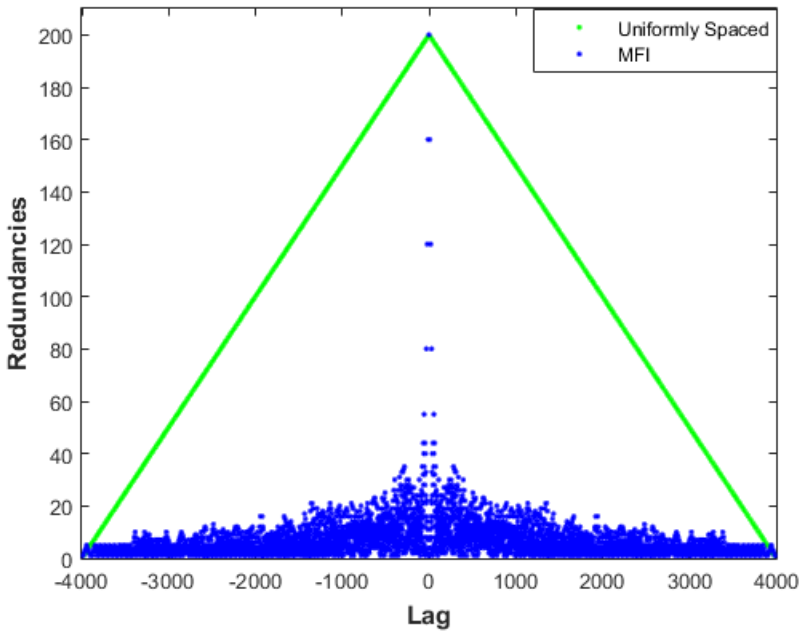

Figure 3.60: Coarrays from using Mixed metrics versus Uniformly-spaced frequency array for blocksize of 1.25%

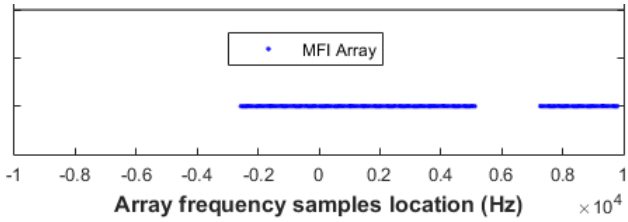

Figure 3.61: Frequency sample locations for blocksize of 2.50% using Mixed metrics (second scenario)

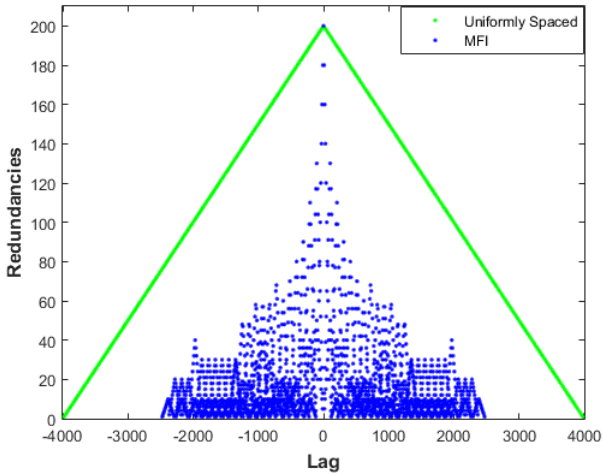

Figure 3.62: Coarrays from MFI generated array using Mixed metrics versus Uniformly-spaced frequency array for blocksize of 2.50%

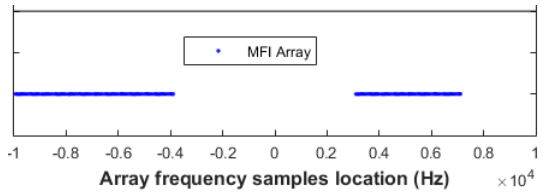

Figure 3.63: Frequency sample locations for blocksize of 5.00% using Mixed metrics (second scenario)

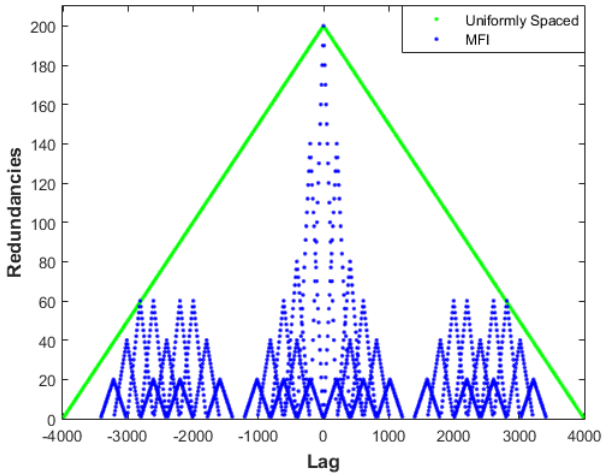

Figure 3.64: Coarrays from MFI generated array using Mixed metric versus Uniformly-spaced frequency array for blocksize of 5.00%

From all the results obtained for the second scenario as shown from Fig. 3.54 - 3.64, for some block sizes like 0.50% and 5.00%, the mixed metric implementation does results in sparse frequency arrays whose coarrays bear more resemblance to a LRLA compared to when they are generated using just MFI metric solely. In fact, for the case of 0.50% block size, the mixed metric implementation produces an sparse frequency array that not only maintains the 3-dB range resolution with a PSL value of -9.541 dB (compared to range resolution degradation factor of 2.00 when solely using MFI metric) but still provides a significant amount of 41.58% of spectrum content for reallocation.

However, for the sparse frequency array generated using other block sizes of 1.00%, 1.25% and 2.50%, there are no significant changes in their coarray structures. Furthermore, for these cases, they now possess 3-dB range resolution degradations of 1.60, 1.33 and 1.67 respectively as compared to zero or minimum range resolution degradation previously when using the MFI metric solely. Thus, from the results obtained from the second scenario when using the frequency block-based insertion approach, it will seem feasible to only use the mixed metric implementation in those instances when the coarray results obtained from using solely MFI metric implementation appears to resemble an USFA structure.

3.2.5 Review of Sparse Spectrum Allocation results from all adaptations based on the Sparse Array Design Perspective

At this stage, we will review the results that have been provided from the Sparse Spectrum Allocation (SSA) algorithm when the algorithm design is approached from the perspective of Sparse Array. As a start, the two example scenarios that are examined under this perspective are as follows:

- The first scenario in which the radar system utilises only 25% of the available spectrum content while releasing the remaining 75% portion of the spectrum for reallocation to other user systems

- The second scenario in which the radar system utilises only 50% of the available spectrum content while the remaining 50% portion are released for reallocation to other user systems

Next, using the two above scenarios, four adaptations of the SSA algorithm were investigated for their performance in terms of preservation of 3-dB range resolution, sidelobe performance and amount of feasible unused spectrum available for reallocation. These four adaptations are namely:

- Single-frequency sample based insertion approach and using the MFI value as the metric for optimization process
- Single-frequency sample based insertion approach and using both MFI and PSL values as the metrics for optimization process
- Block-frequency samples based insertion approach and using the MFI value as the metric for optimization process. Also, various block sizes are evalulated for this approach
- Block-frequency samples based insertion approach and using both MFI and PSL values as the metrics for optimization process along with using various block sizes for the investigation

Based on the results obtained of the first adaptation for both scenarios, it has been shown that it is possible to systematically design such a sparse frequency array that can maintain the 3-dB range resolution. Hence, the first objective of the dissertation has been achieved using this adapation. However, with these results, the tradeoff includes a significantly degraded sidelobe performance when compared to using the full spectrum. For instance, when using the full spectrum, the Matched filter response will produce a resulting PSL value of -13.50 dB and ISL value of -7.25 dB. However, for the first scenario, the PSL value has been degraded to -9.919 dB and the ISL value by 12.47 dB. As for the second scenario, although there is no degradation observed for the PSL value, the ISL value is still degraded by 4.32 dB compared to using the full spectrum. In spite of the sidelobe performance degradation, for both scenarios, there are no grating lobes generated for both sparse frequency arrays produced using this adaptation when compared to using an uniformly-spaced frequency array.

Also, for the first adaptation, due to the generation of many small spectrum gaps between adjacent samples with gap widths slightly greater than the Nyquist sampling interval, the amount of spectrum content that is deem feasible to be reusable is an amount of 46.85% for the first scenario instead of the theoretical amount of 75.0%. As for the second scenario, the feasible amount drops even lower to a value of 9.57% from the theoretical amount of 50.0%.

Next, to tackle the first issue of improving the sidelobe performance for both scenarios obtained from using the first adapation, the second adaption for the SSA algorithm that uses both MFI and PSL metrics was then implemented for testing both scenarios. Results obtained for the first scenario reveals that although the PSL value has improved from -9.919 dB to -14.3 dB and the amount of reusable spectrum content improves to 54.03% from 46.85%, this improvement comes at the expense of the 3-dB range resolution being degraded by a factor of two. Similarly, results obtained for the second scenario also do not show any improvement over the first adaptation in sidelobe or reusable spectrum performance other than the ISL value improving from a degradation of 4.32 dB down to 2.78 dB. Thus, based on the results obatined from both scenarios, it is seen that when the single frequency sample-based insertion approach of the SSA algorithm is adopted, the usage of the mixed metric implementation is unable to improve on the sidelobe performance obtained when using solely MFI metric.

Going further, to tackle the second issue of the first adaptation with regards to increasing the feasible reusable amount of spectrum for reallocation, the third adaptation of the SSA algorithm on using both frequency block-based insertion approach and solely MFI metric was explored and various block sizes of [0.50, 1.00, 1.25, 2.50, 5.00] percent of the total spectrum were tested on both scenarios.

From the results obtained from the first scenario, a trend was observed from the corresponding coarray structure of all the sparse frequency arrays generated using these various frequency block sizes. This trend is that the coarray structures bear more resemblance to an uniformly spaced

frequency array (USFA) rather to that of a low redundunacy linear frequency array (LRLA). Based on this resemblance, thus a hypothesis is formed in that this adaptation of the SSA algorithm is stuck at local minimas during the optimization process. As such, the results obtained from using the various frequency block sizes are sub-optimal in terms of preserving the 3-dB range resolution as almost all combinations of block sizes will result in 3-dB range degradation in excess of a factor of 3.75 although more than 70% of the full spectrum can be reused for reallocation. The seeming exception to this trend is that of using the frequency block size of 1.25% of which the 3-dB range resolution is only degraded by a factor of 1.20 while allowing for an amount of around 75.00% of spectrum to be reallocated. However, in this case, the PSL value has a very high value of -4.386 dB. Nevertheless, for all the results obtained when using the third adaptation for the first scenario, one very important point to take note is that there are still no grating lobes generated at all in any of the sparse frequency arrays produced using this adaptation although their coarray structures may resemble an USFA.

Next, the results obtained from the second scenario using the third adapation are then examined. Again, for the smallest and largest frequency block sizes used, the trend of their coarray structures bearing more resemblance to an USFA is observed and thus lends more support to the hypothesis mentioned above. As such, the results obtained from using these two frequency block sizes produces 3-dB range degradation in excess of a factor of 1.75 although more than 42.80% of the full spectrum can be reused for reallocation. However, for the other frequency block sizes of 1.00% and 1.25%, the improvements obtained from using this adaptation are very substantial. Besides the ability to preserve the 3-dB range resolution with no degradation, the resulting sparse frequency arrays also allows for an amount of at least 40.00% of spectrum to be reallocated compared to 9.57% when using the first adaptation. The only tradeoff is that the PSL value is being degraded to values of -8.89 dB and -11.39 dB in the third adaptation as compared to -13.98 dB when using the first adaptation. Finally, when using the frequency block size of 2.50%, the 3-dB range resolution is also only degraded by a factor of 1.20 while allowing for an amount of around 48.00% of spectrum to be reallocated. However, for this case, the PSL value is again a very high

value of -6.29 dB. Likewise, for the second scenario, there are again no grating lobes generated for those sparse frequency arrays produced using the third adaptation although their coarray structures may resemble an USFA.

Finally, to address the issues of coarray structures resembling that of an USFA as seen in the third adaptation that may be due to the hypothesis mentioned above, the fourth adaptation of the SSA algorithm on using both frequency block-based insertion approach and mixed MFI/PSL metrics was explored using the same block sizes of the total spectrum as prior on both scenarios. From the results obtained for the first scenario, the coarray structures generated from the sparse frequency arrays do show more resemblances to a LRLA when compared to the third adaptation. However, besides this difference in the coarray structures, there are no performance improvements noted in either the sidelobe level or the amount of feasible unused spectrum for reallocation. Next, in terms of coarray structures generated for the second scenario, it is also observed that those coarray structures that previously resemble an USFA have been modified to resemble that of a LRLA when using the fourth adaptation. Furthermore, improvements are also obtained for these sparse frequency arrays who belong to this category. For instance, for the frequency block size of 0.50%, the new sparse frequency array generated is able to maintain the 3-dB range resolution with no degradation at a PSL level of -9.541 dB and a feasible unsued amount of 41.58% of spectrum for reallocation. This is another big improvement from the third adaptation in which the 3-dB range resolution was degraded by a factor of 1.75 while allowing for more than 42.80% of the full spectrum to be reused for reallocation.

To summarise, based on the results obtained from all four adaptations implemented for the design of sparse frequency arrays, it has been demonstrated that it is possible to design a Sparse Spectrum Allocation algorithm using a methodical approach with either the MFI metric or a mixture of MFI/PSL metrics during the optimization process to achieve the following objectives:

- Maintaining the 3-dB radar range resolution while only using a portion of the total allocated spectrum

1. For the first scenario of 25.0% usage of the spectrum, the best result is obtained when using the first adaptation in which the PSL value is -9.919 dB (compared to -13.50 dB for full spectrum usage). The second best result is obtained when using the third adaptation for the frequency blocksize set to 1.25% in which the 3-dB range resolution is slightly degraded by a factor of 1.20 with a PSL value of -4.366 dB
2. For the second scenario of 50.0% usage of the spectrum, the best result is obtained when using the third adaptation in which the PSL value is -11.39 dB when using a frequency block size of 1.25%. The second best result is obtained when using the fourth adaptation for the frequency block size of 0.50% in which the PSL value is -9.541 dB

- Providing a feasible amount of spectrum gaps for reallocation to other wireless users such as communication systems

1. For the first scenario of 25.0% usage of the spectrum, the best result is obtained when using the first adaptation in which the 46.85% of spectrum can be feasibly reallocated. The second best result is obtained when using the third adaptation for the frequency blocksize set to 1.25% in which 74.0% of spectrum can be feasibly reallocated
2. For the second scenario of 50.0% usage of the spectrum, the best result is obtained when using the third adaptation in which 41.88% of the spectrum can be reallocated. The second best result is obtained when using the fourth adaptation for the frequency block size of 0.50% in which 41.58% of spectrum can be reallocated

3.3 Implementation of SSA algorithm based on the Array Thinning Design Perspective

In this section of Chapter 3, the second perspective of array thinning will be adopted for the design of the SSA algorithm. Also, for simulating the target scenario, the same parameters as per Table 3.1 will be used in this section as well. At the same time, a description of the array thinning design based SSA algorithm is provided in the next paragraph.

Initially, starting from an fully filled measurement array with N number of frequency samples, the optimization process involved will remove one block of frequency samples or from the viewpoint of gap block insertion, insert a gap whose width is equivalent to the amount of frequency samples covered by a block. Also, the criteria to identify the starting location of each block to be removed in order to thin the spectrum is by either using MFI metric or with the mixed MFI/PSL metrics. Finally, the goal of the SSA algorithm will be to remove P frequency blocks corresponding to K number of frequency samples where these K frequency samples represent the percentage of spectrum to be thinned or removed.

Next, the rationale for not using the approach of single frequency sample-based location removal is from the practical viewpoint of providing spectrum sharing between the radar and other wireless systems. As there should be a minimum gap width to faciliate the reallocation of all usable spectrum gaps fulfilling this requirement to other systems, thus it is impractical to implement the removal of single frequency-based gap location for the array thinning process as the gap width provided from just one frequency sample location will be too small for practical usage. However, when using the approach of using block-based frequency samples removal, there is now another potential issue that may appeared. This issue is that the amount of retained spectrum content between two adjacent gaps can be as small as that occupied by a single frequency sample location. Thus, the resulting thinned spectrum can consists of uneven blocks of remaining frequency samples for the radar application with some of these remaining blocks being as small as a single frequency

sample location.

Going further, for the array thinning design based SSA algorithm implementation, the amount of spectrum content being considered for removal are namely, 40% and 15% or the values 160 and 60 frequency samples out of a total of 400 frequency samples (Nyquist sampling requirement). This will mean that the radar system will retain either 60%, and 85% usage of the total available spectrum accordingly and these usages are denoted as the third and fourth scenarios accordingly. Also, as mentioned above, two adaptations of the SSA algorithm based on frequency gap-block removal approach will be considered, namely either using solely the MFI metric or with the mixed MFI/PSL metrics during the optimization process. In addition, for these two scenarios, the size of the frequency blocks/gaps considered for removal/insertion are chosen as [2.50, 5.00] percent of the total spectrum. Thus, for the third scenario on using 60% of the spectrum, the number of frequency blocks to be removed are 16 and 8 accordingly. For the fourth scenario on using 85% of the spectrum, the number of frequency blocks to be removed are 6 and 3 accordingly.

In the next subsection, the first adaptation of the removal of frequency blocks or insertion of gap blocks will be examined starting with the third scenario of retaining 60% of the original spectrum for the radar application and followed by the fourth scenario of retaining 85% of the spectrum likewise.

3.3.1 Construction of Array Thinning model based on MFI metric - first adaptation

As a start, the results obtained from the third scenario using a gap size of 2.50% are presented in Fig. 3.65 - 3.67 below. This also means that there are a total of 16 frequency blocks that are removed corresponding to the spectrum retention of 60%.

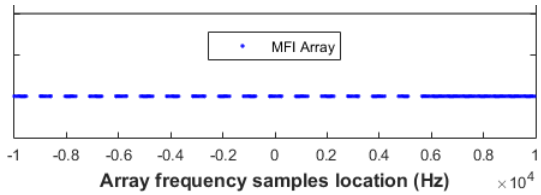

Figure 3.65: Frequency sample locations
for gap size of 2.50% (third scenario)

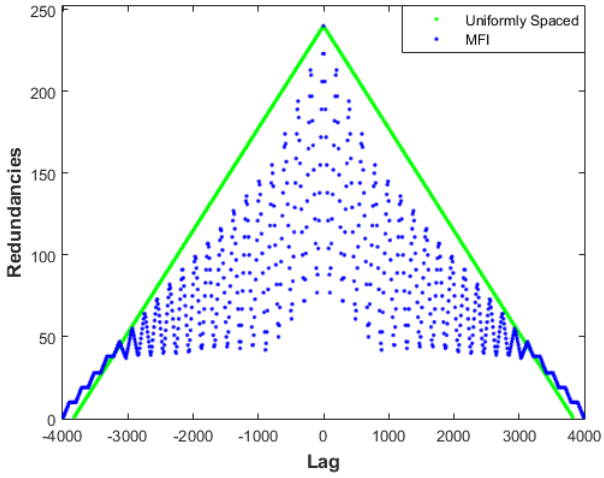

Figure 3.66: Coarrays from MFI generated array versus Uniformly-spaced frequency array
for gap size of 2.50%

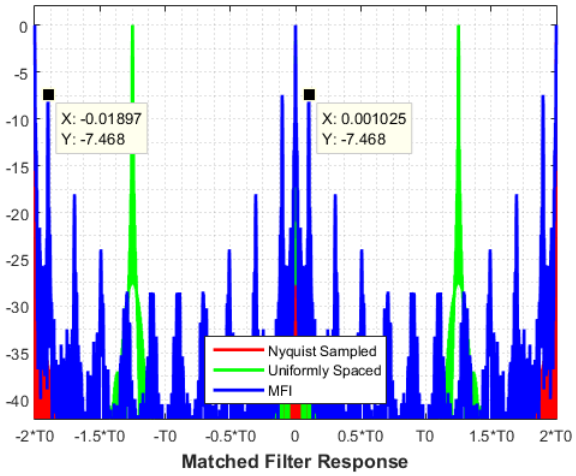

Figure 3.67: Matched Filter Response using MFI generated array
for gap size of 2.50%

From Fig. 3.65, the locations of the 16 gaps that were determined by the SSA algorithm to be the most optimal locations for removing 40% of the spectrum for reallocation are observed. Note that instead of evenly inserting the gap blocks across the spectrum as is the approach of an USFA, the appearance from the final thinned frequency array bears some resemblance to an irregularly spaced frequency array or a LRLA. Thus, this resulted in a interesting shape in its coarray structure. Finally, when using a gap size of 2.50%, by examining Fig. 3.67, it is determined that the resulting optimized array is able to maintain the 3-dB range resolution while exhibiting a degraded PSL value of -7.468 dB as well as ISL value degradation of -9.288 dB.

Next, the results obtained from the third scenario when using a gap block size of 5.00% are shown in the Fig. 3.68 - 3.70 below and in the following page. By examining these results, it is observed that the same trend in terms of the appearance of the thinned frequency array and its coarray is present as well when using this larger gap size. However, by examining Fig. 3.70, it is determined that the resulting optimized array from using this gap size has result in a 3-dB range resolution degradation of 1.13 compared to that of using the 2.50% gap size that does not suffer from any range resolution degradation. Due to this range resolution degradation, the sidelobe performances obtained from using the 5.00% gap block size exhibit a better PSL value of -13.875 dB along with lesser ISL value degradation of -6.695 dB.

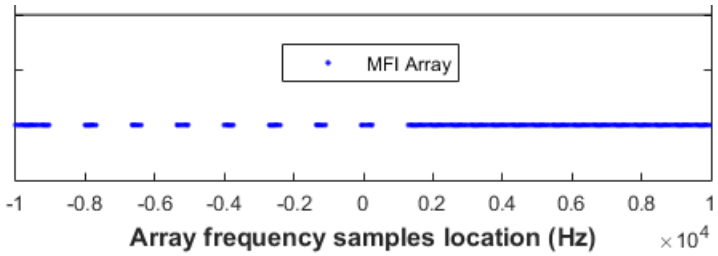

Figure 3.68: Frequency sample locations for gap size of 5.00% (third scenario)

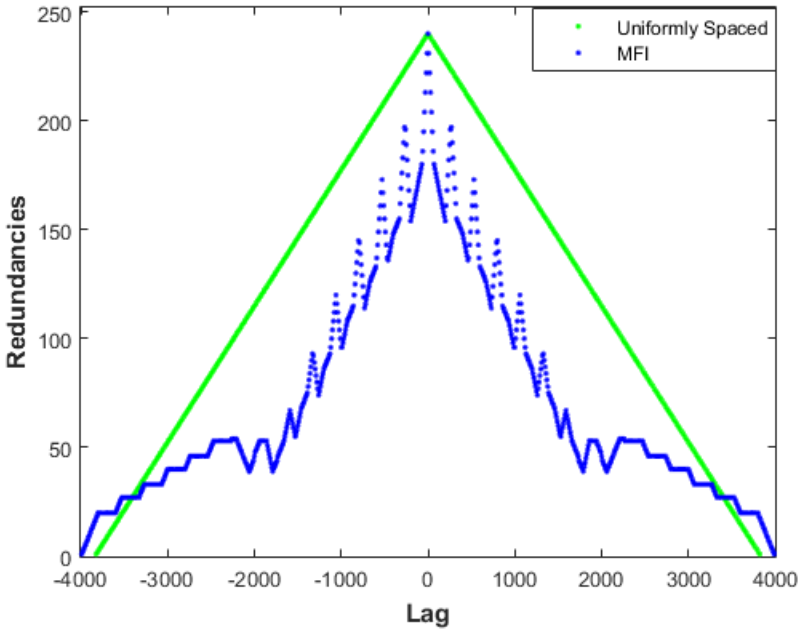

Figure 3.69: Coarrays from MFI generated array versus Uniformly-spaced frequency array for gap size of 5.00%

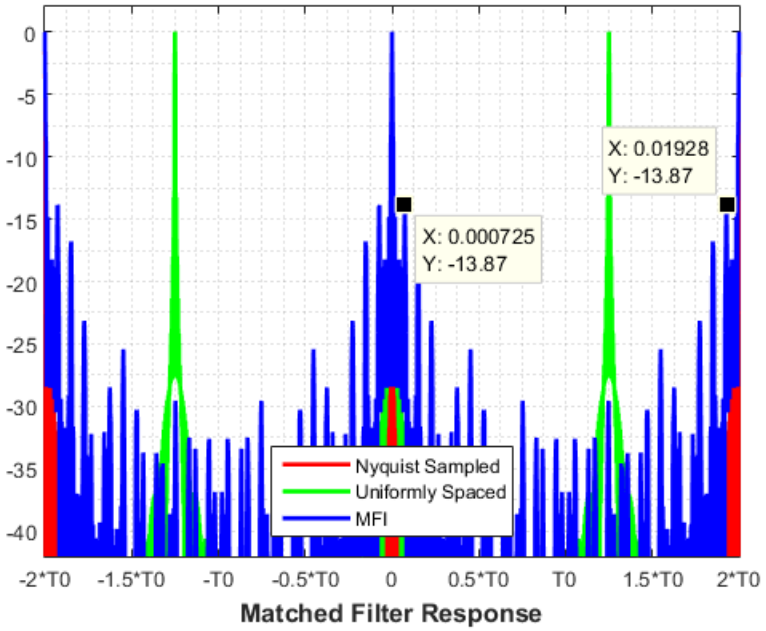

Figure 3.70: Matched Filter Response using MFI generated array for gap size of 5.00%

After examining the results of the SSA algorithm on the third scenario when using the gap block sizes of 2.50% and 5.00%, the results obtained from applying the SSA algorithm to the fourth scenario of releasing 15% of the original spectrum are as shown in the following figures. Also, for this scenario, when using a gap block size of 2.50%, 6 gaps will be inserted to the original fully-filled frequency array when using the SSA algorithm. Similarly, when using a gap block size of 5.00%, only 3 gaps will be inserted into the original frequency array.

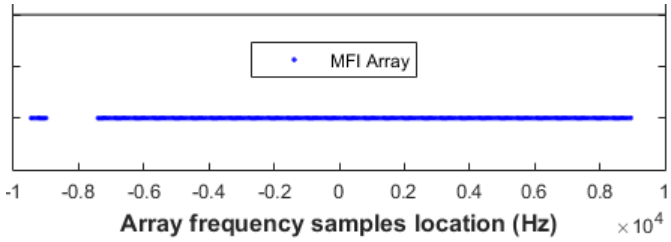

Figure 3.71: Frequency sample locations for gap size of 2.50% (fourth scenario)

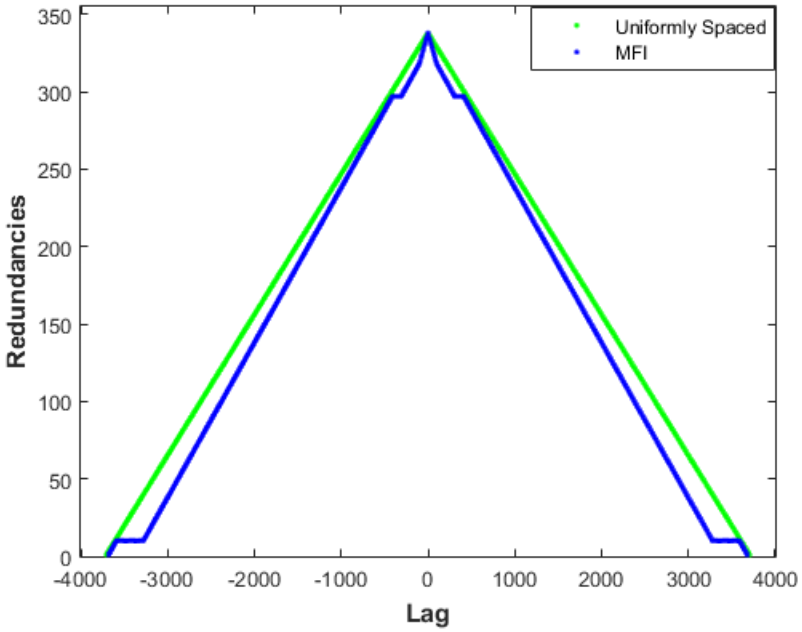

Figure 3.72: Coarrays from MFI generated array versus Uniformly-spaced frequency array for gap size of 2.50%

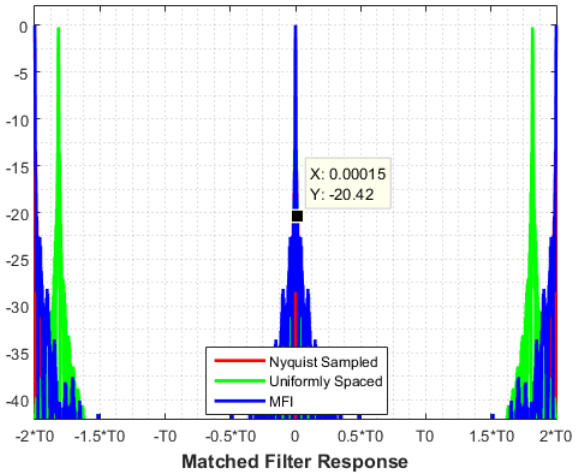

Figure 3.73: Matched Filter Response using MFI generated array
for gap size of 2.50%

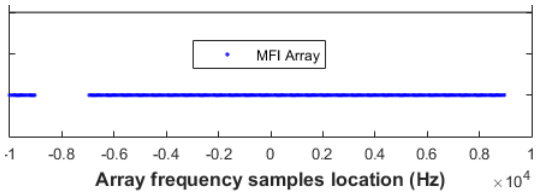

Figure 3.74: Frequency sample locations for gap size of 5.00% (fourth scenario)

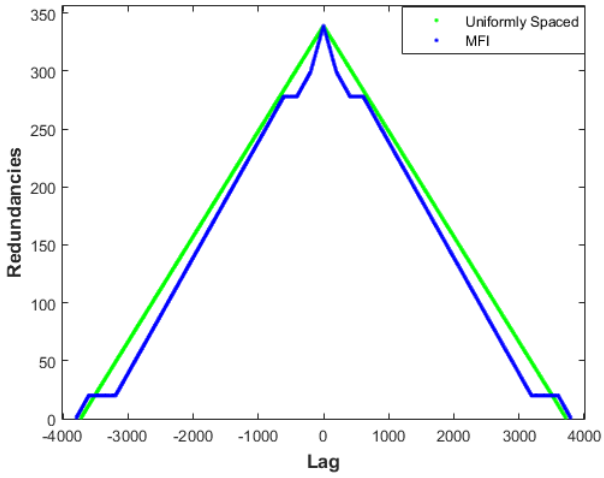

Figure 3.75: Coarrays from MFI generated array versus Uniformly-spaced frequency array
for gap size of 5.00%

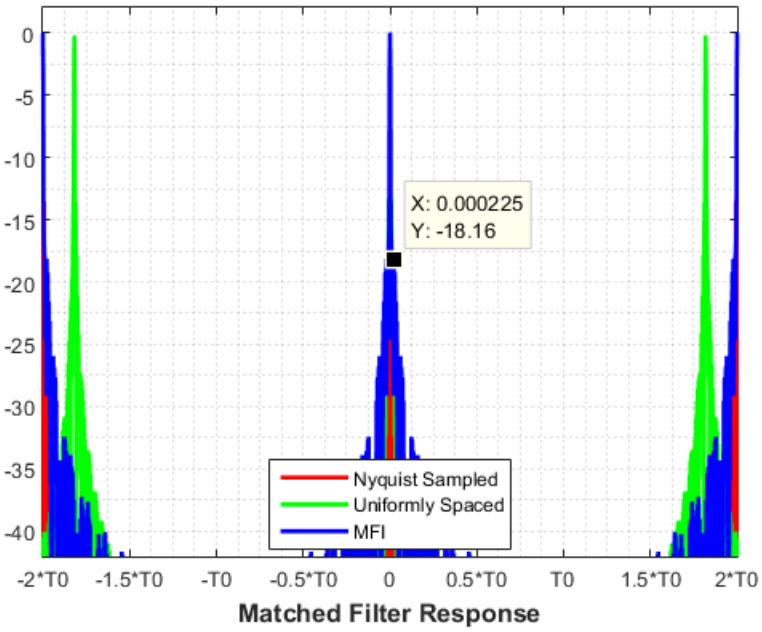

Figure 3.76: Matched Filter Response using MFI generated array for gap size of 5.00%

From examining the results of the SSA algorithm as shown in Fig. 3.71 - 3.76 on the fourth scenario when using gap block sizes of 2.50% and 5.00%, it is observed that these two larger thinned frequency arrays also bear some similarity to a irregularly-spaced frequency array with both a larger spectrum segment and a smaller spectrum segment being retained in the thinned frequency array for the radar application. Moreover, for the case of using 2.50% gap block size, the resulting PSL value is -20.42 dB and there is even an improvement in the ISL value of an amount of 0.69 dB when compared to using the full contiguous spectrum. As for the case of using 5.00% gap block size, the resulting PSL value has -18.16 dB with a ISL value degradation of only 0.635 dB. However, these "encouraging" good sidelobe level performances comes about due to the resulting 3-dB range resolution degradation by a factor of 1.32 when using the 2.50% gap block and a factor of 1.33 when using the 5.00% gap block.

At this stage, it has been shown that it is possible to implement a SSA algorithm for generating a sparse frequency array that is based on the second perspective of Array Thinning Design. By using

this perspective, a clear advantage is that it will be possible to predesign the minimum size of the gap to be inserted into the fully-filled frequency array without having to encounter the possibility of small unusable gaps being generated as was observed from the results obtained when using the first perspective of Sparse Array Design.

Next, as per the previous section in using the first perspective of Sparse Array Design, the first adaptation is also modified to incorporate mixed MFI/PSL metrics during the optimization so as to investigate on whether this new adaptation will produce better results in terms of sidelobe level performance. The results obtained from applying this second adaptation to both third and fourth scenarios will be presented for discussion in the following subsection.

3.3.2 Construction of Array Thinning model based on mixed MFI/PSL metrics - second adaptation

In this subsection, the gap block-insertion based SSA algorithm with the mixed MFI/PSL optimization metric is applied to the third and fourth scenarios of 60% and 85% usage of spectrum by using gap block sizes of 2.50% and 5.00%. Results obtained from the third scenario are presented for discussions and followed by that from the fourth scenario.

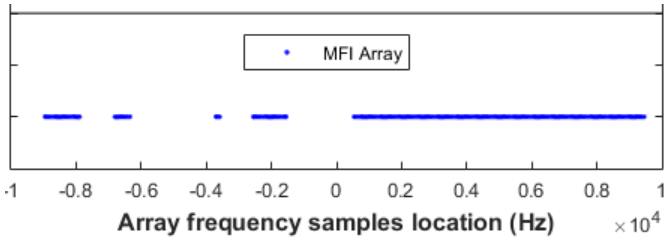

Figure 3.77: Frequency sample locations for gap size of 2.50% using Mixed metrics (third scenario)

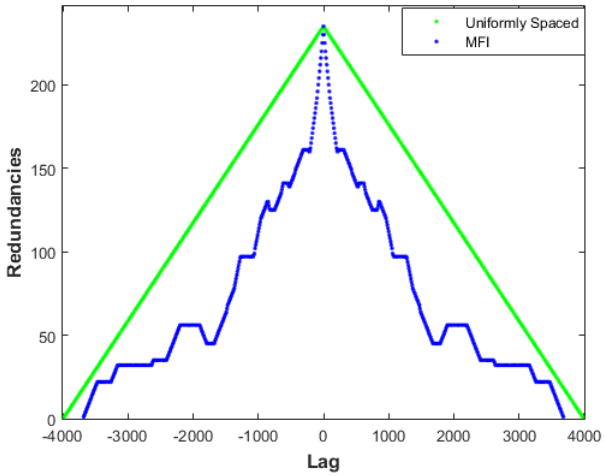

Figure 3.78: Coarrays from using Mixed metrics versus Uniformly-spaced frequency array for gap size of 2.50%

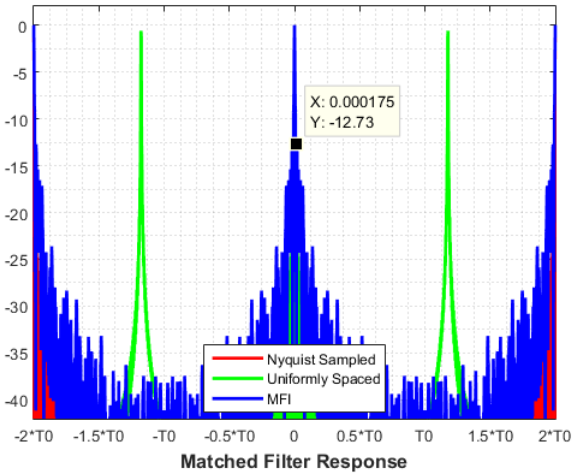

Figure 3.79: Matched Filter Response using Mixed metrics for gap size of 2.50%

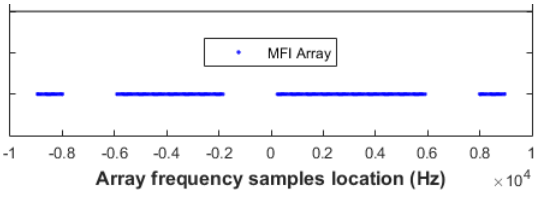

Figure 3.80: Frequency sample locations for gap size of 5.0% when using Mixed MFI/PSL metrics (third scenario)

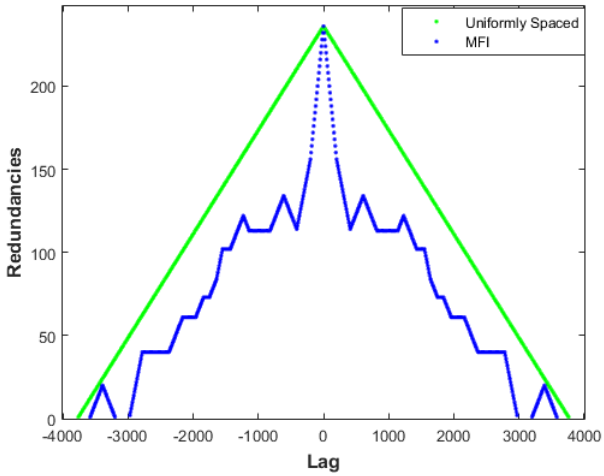

Figure 3.81: Coarrays from using Mixed metrics versus Uniformly-spaced frequency array for gap size of 5.00%

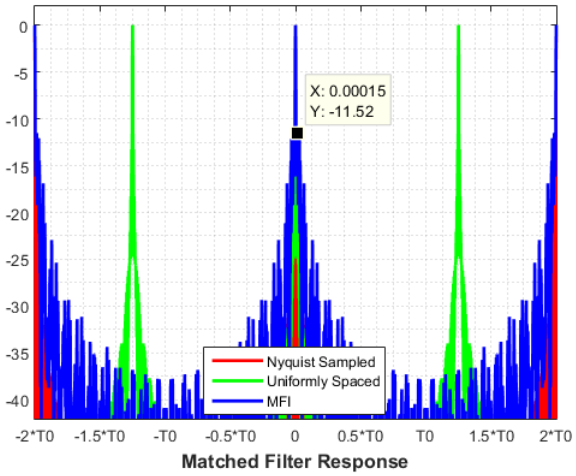

Figure 3.82: Matched Filter Response using Mixed metrics for gap size of 5.00%

As a start, the results obtained by using the gap size of 2.50% for the third scenario are examined. By comparing both thinned frequency array and its corresponding coarray generated using solely MFI metric as shown in Fig. 3.65 - 3.66 with the new results generated using mixed metrics implementation as shown in Fig. 3.77 - 3.78, it is seen that the mixed metric implementation does help to produce a thinned frequency array that shows more resemblance to a LRLA. At the same time, by comparing both Fig. 3.67 and Fig. 3.79, it is observed that the Matched filter response

obtained using mixed metrics approach also exhibits better sidelobe level performances. However, upon closer examination of Fig. 3.79, it is determined that the improved performances in sidelobe level comes about due to the 3-dB range resolution degradation by a factor of 1.33 as compared to zero range resolution degradation when using solely MFI metric. Nevertheless, due to the uneven distribution of the inserted gap blocks within the thinned frequency array generated when using mixed metrics (Fig. 3.65), the two largest gaps generated have consolidated widths of 13.0% and 10.0% as compared to just constant gap width of 2.50% when using solely MFI metric-based implementation. These larger gap sizes are definitely more useful for reallocation to another system when both systems are coexisting in a Spectrum sharing mode.

Next, by examining the results as shown in Fig. 3.80 - 3.82 that are obtained when using the gap size of 5.00% on the same scenario, it is seen that these results are much worst off when compared to solely using the MFI metric-based implementation as shown in Fig. 3.68 - 3.70. Besides suffering from 3-dB range resolution degradation by a factor of 1.40 as compared to the previous smaller value of 1.13, this deterioration is also accompanied by both poorer PSL and ISL values. The only improvement obtained from the results by using the mixed metrics-based implementation is that the average gap size that are generated in the new thinned frequency array are now about 10.0% as compared to 5.00% when solely using the MFI metric-based implementation.

Finally, the last set of results to be reviewed under the second perspective of Array Thinning Design is that from applying the mixed metrics-based implementation to the fourth scenario. Results obtained from both usage of 2.50% and 5.00% gap sizes are shown in Fig. 3.83 - 3.88 in the following pages.

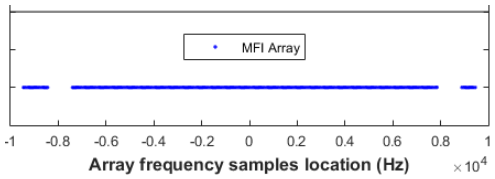

Figure 3.83: Frequency sample locations
for gap size of 2.50% using Mixed metrics (fourth scenario)

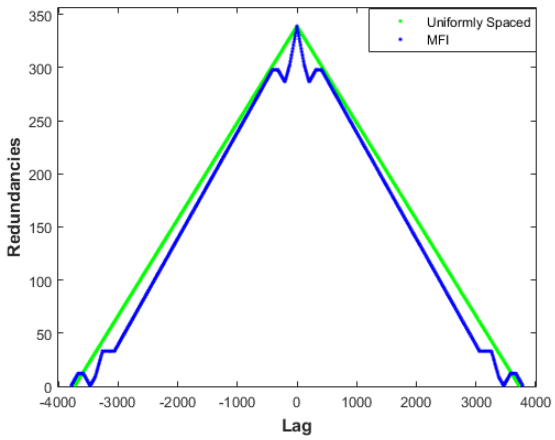

Figure 3.84: Coarrays from using Mixed metrics versus Uniformly-spaced frequency array
for gap size of 2.50%

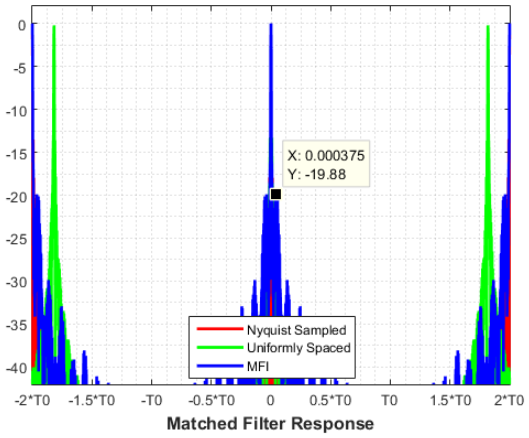

Figure 3.85: Matched Filter Response using Mixed metrics
for gap size of 2.50%

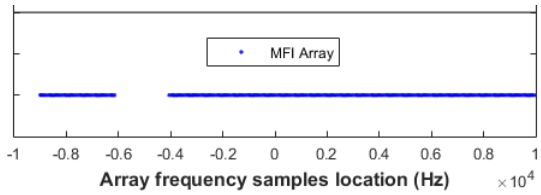

Figure 3.86: Frequency sample locations
for gap size of 5.00% when using Mixed MFI/PSL metrics (fourth scenario)

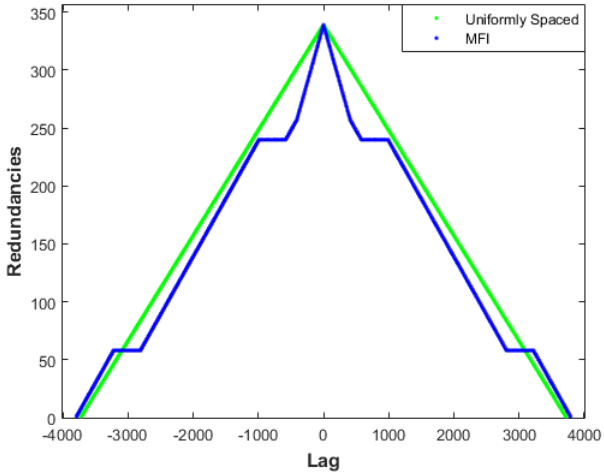

Figure 3.87: Coarrays from using Mixed metrics versus Uniformly-spaced frequency array
for gap size of 5.00%

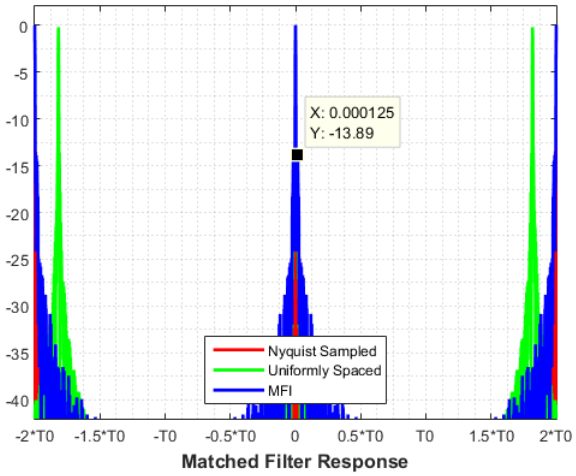

Figure 3.88: Matched Filter Response using Mixed metrics
for gap size of 5.00%

From the results obtained from the fourth scenario for the case of using 2.50% gap size, it is observed that the mixed metrics-based implementation does not produce a set of results that is significantly different compared to using solely MFI metric-based implementation. Also, in the case of using gap block width of 5.00%, only some improvement is noted the 3-dB range resolution degradation factor is now reduced from 1.33 to 1.16 with the corresponding PSL value of -13.89 dB (compared to -18.16 dB) along with ISL value degradation of -3.481 dB (compared to -0.6354 dB).

3.3.3 Review of Sparse Spectrum Allocation results from all adaptations based on the Array Thinning Design Perspective

At this stage, we will review the results that have been provided from the Sparse Spectrum Allocation (SSA) algorithm when the algorithm design is approached from the perspective of Array Thinning Design. As a start, the two example scenarios that are examined under this perspective are as follows:

- The first scenario in which the radar system utilises 60% of the available spectrum content while releasing the remaining 40% portion of the spectrum for reallocation to other user systems
- The second scenario in which the radar system utilises 85% of the available spectrum content while the remaining 15% portion are released for reallocation to other user systems

Next, using the two above scenarios, two adaptations of the SSA algorithm were investigated for their performance in terms of preservation of 3-dB range resolution, sidelobe performance and amount of feasible unused spectrum available for reallocation. These two adaptations are namely:

- Gap block-samples based insertion approach and using the MFI value as the metric for optimization process. Also, two gap sizes are evalulated for this approach

- Gap block-samples based insertion approach and using both MFI and PSL values as the metrics for optimization process along with using the same gap sizes for the investigation

Based on the results obtained of both adaptations for both scenarios, it is again shown that it is possible to systematically design such a sparse frequency array with the objective of maintaining the 3-dB range resolution when approaching from the perspective of Array Thinning Concept. Also, when using this approach, the application of mixed MFI/PSL metrics in the second adaptation will not result in any performance improvement in either the sidelobe level or range resolution degradation as compared to the results obtained solely using the MFI metric-based implementation. Thus, unlike the case of constructing sparse frequency arrays based on the perspective of Sparse Array Design when improvements are obtained when using the mixed metrics-based implementation, it is determined that it is not necessary to adopt this approach when performing array thinning for spectrum usage exceeding 50.00% by the radar system. The main reason for this outcome is due to the fact that there are less degrees of freedoms or flexibility for inserting the gap blocks when both the amount of spectrum for retention and gap sizes are large.

Finally, one possible useful outcome that comes about from using mixed metrics-based implementation for array thinning is that the resulting gap widths are larger due to consolidation as compared to using solely MFI metric-based implementation. As such, this will allow for more practical usage of the results from using mixed metrics-based implementation as it is always easier to reallocate a larger gap width in the spectrum for usage by other systems.

Chapter 4

Higher-order PCFM waveforms

4.1 Characteristics of PCFM waveform

4.1.1 First-order PCFM waveform

In [6],it was shown how the CPM implementation that has been used to provide power/spectrally efficient communications [64] could be modified to enable the implementation of arbitrary polyphase codes (specifically, zeroth-order codes) as physically realizable FM radar waveforms. Such waveforms may also be directly optimized [14]. Due to the nature of this implementation, the polyphase-coded FM (PCFM) scheme [6] corresponds to a first-order representation in which the phase function of waveform $s(t) = exp\{j\phi_1(t)\}$ can be expressed as:

$$\phi_1(t) = \int_0^t \left[\sum_{n=1}^{N} a_n g_1(t' - (n-1)T_p) \right] dt' + \bar{\phi}_1 \tag{4.1}$$

where the set of phase-change value a_n for $n = 1, 2, ...N$ constitute a first-order code (which may or may not be derived from a zeroth-order code of length $N + 1$ per [6] that produces a continuous waveform of pulsewidth T. The term $g_1(t)$ is a shaping filter that integrates to unity over the time support [0,T_p] for $T_p = T/N$, and $\bar{\phi}_1$ is the initial phase for the waveform. If $g_1(t)$ is a rectangular filter, the phase function in (4.1) is piece-wise linear. Let the continuous, first-order coded function

inside the brackets of (4.1) be:

$$\chi_1(t) = \sum_{n=1}^{N} a_n g_1(t-(n-1)T_p) \tag{4.2}$$

which represents the time-varying frequency of the waveform, then (4.1) becomes:

$$\phi_1(t) = \int_0^t \chi_1(t')dt' + \bar{\phi}_1. \tag{4.3}$$

From [6], the first-order phase function of 4.1 - 4.3 can be implemented as shown in Fig.4.1 below.

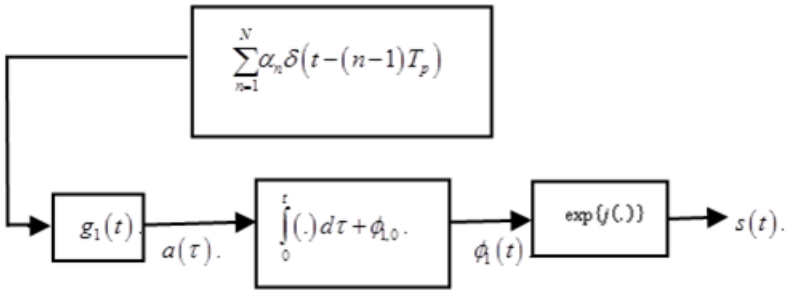

Figure 4.1: First-order implementation of polyphase-coded FM (PCFM) waveforms

The first-order code a_n represents the (normalized) time-varying frequency with permissible values in $[-\pi,\pi]$. Because $g_1(t)$ integrates to unity over $[0,T_p]$, the maximum phase change in T_p seconds is $\pm\pi$. Thus the 3 dB bandwidth is

$$\pm(\frac{\pi}{T_p}) = \pm(\frac{\pi N}{T}) = \pm(\frac{\pi BT}{T}) = \pm\pi B \; rad/s, \tag{4.4}$$

$\pm(B)/2$ Hz (at baseband), in which the relationship $T = NT_p$ is utilized and the fact that the time-bandwidth product BT is well approximated by N. Note that the permissible region of $[-\pi,\pi]$ for the code values can be expanded to provide greater design freedom as long as appropriate spectral containment measures are also enforced to prevent expansion of the spectral content (see [73]).

4.1.2 Formulation of second/third-order PCFM implementation

Using the format defined by (4.3), the generalization to second-order and third-order waveform phase functions can be expressed as

$$\phi_2(t) = \int_0^t \int_0^{t'} \chi_2(t'')\, dt''dt' + \int_0^t \bar{\omega}_2 dt' + \bar{\phi}_2 \tag{4.5}$$

and

$$\phi_3(t) = \int_0^t \int_0^{t'} \int_0^{t''} \chi_3(t''')\, dt'''\, dt''\, dt' + \int_0^t \int_0^{t'} \bar{\beta}_3, dt''\, dt' + \int_0^t \bar{\omega}_3 dt' + \bar{\phi}_3 \tag{4.6}$$

respectively, where $\bar{\phi}_2$ and $\bar{\omega}_2$ are the second-orderinitial phase and frequency and $\bar{\phi}_3$, $\bar{\omega}_3$, and $\bar{\beta}_3$ are the third-order initial phase, frequency, and chirp-rate. Like the first-order coded function $\chi_1(t)$ in 4.2, the second-order coded function from (4.5) is defined as

$$\chi_2(t) = \sum_{n=1}^{N} b_n g_2(t-(n-1)T_p) \tag{4.7}$$

and the third-order coded function from (4.6) is

$$\chi_3(t) = \sum_{n=1}^{N} c_n g_3(t-(n-1)T_p). \tag{4.8}$$

In (4.7), the *second-order code* b_n for $n = 1,2,...N$ represents the time-varying chirp-rate. Likewise, the third-order code c_n for $n = 1,2,...N$ in (4.8) represents the time-varying chirp-acceleration. As with the first-order formulation, $g_2(t)$ and $g_3(t)$ are shaping filters defined on the interval [0,T_p]. Imposing the same bandwidth as determined by (4.4) onto these higher-order implementations requires that the compounding effect of the additional integration stages be taken into account, which impacts the selection of the coding values b_n and c_n as well as the associated shaping filters $g_2(t)$ and $g_3(t)$. Also note that b_n, c_n, $\bar{\omega}_2$, $\bar{\omega}_3$, and $\bar{\beta}_3$ are in angular units (i.e. scaled by 2π), with the permissible initial frequencies $\bar{\omega}_2$, $\bar{\omega}_3 \in [-\pi/T_p,+\pi/T_p]$ and the initial chirp-rate $\bar{\beta}_3 \in$

$[-2\pi/NT_p^2, +2\pi/NT_p^2]$.

Fig.4.2 and Fig.4.3 illustrate the implementation of these second-order and third-order phase functions. Clearly, even higher order phase functions could be formulated in this manner, though such have not been found to be that useful with regard to radar waveform design. In fact, it will be shown in a later section that while the second-order formulation facilitates the design of waveforms with marked sidelobe level improvement relative to the first-order implementation, the same cannot be said for the third-order scheme, which only provides a modest benefit when combined with the first and second orders.

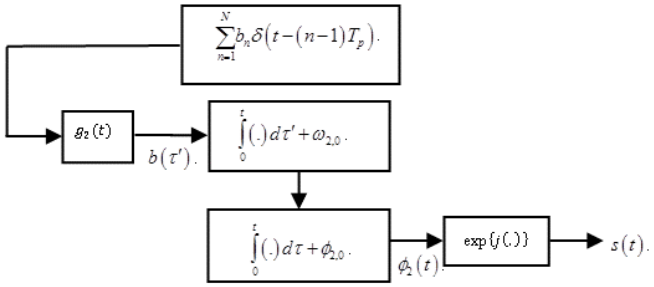

Figure 4.2: Second-order PCFM waveform implementation

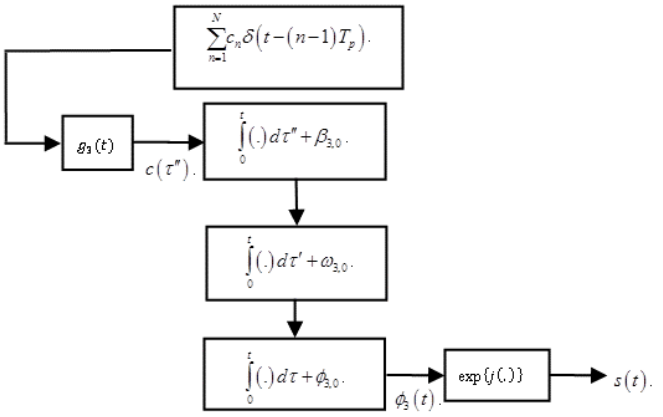

Figure 4.3: Third-order PCFM waveform implementation

4.1.3 Relationships between different PCFM implementations

The relationships between different implementation orders provide some insight into the relative waveform design freedom of each, their permissible code values, and appropriate optimization approaches. Now, as (4.3), (4.5), and (4.6) provide the instantaneous phase function for each of these implementations, the instantaneous frequency function of each can be obtained by substituting in the respective coding structures of (4.2), (4.7), and (4.8) and then taking the derivative as

$$\dot{\phi_1}(t) = \frac{d\phi_1(t)}{dt} = \sum_{n=1}^{N} a_n g_1(t-(n-1)T_p) \tag{4.9}$$

$$\dot{\phi_2}(t) = \frac{d\phi_2(t)}{dt} = \int_0^t \sum_{n=1}^{N} b_n g_2(t'-(n-1)T_p)\,dt' + \bar{\omega}_2 \tag{4.10}$$

and

$$\dot{\phi_3}(t) = \frac{d\phi_3(t)}{dt} = \int_0^t \int_0^{t'} \sum_{n=1}^{N} c_n g_3(t''-(n-1)T_p)\,dt''\,dt' + \int_0^t \bar{\beta}_3\,dt' + \bar{\omega}_3 \tag{4.11}$$

Likewise, the instantaneous chirp-rate of each implementation is obtained via an additional derivative as

$$\ddot{\phi_1}(t) = \frac{d^2\phi_1(t)}{dt^2} = \sum_{n=1}^{N} a_n \dot{g}_1(t-(n-1)T_p) \tag{4.12}$$

$$\ddot{\phi_2}(t) = \frac{d^2\phi_2(t)}{dt^2} = \sum_{n=1}^{N} b_n g_2(t-(n-1)T_p) \tag{4.13}$$

and

$$\ddot{\phi_3}(t) = \frac{d^2\phi_3(t)}{dt^2} = \int_0^t \sum_{n=1}^{N} c_n g_3(t-(n-1)T_p)\,dt' + \bar{\beta}_3 \tag{4.14}$$

noting that the first-order representation in (4.12) involves the derivative of the shaping filter

$g_1(t)$.

As an illustrative example, the linear FM (LFM) chirp which possesses a rather simple structure and is an easy waveform to generate in hardware (e.g. via a swept local oscillator) is being considered. For 3 dB bandwidth B and pulsewidth T, the LFM chirp-rate is

$$\beta_{LFM} = \frac{B}{T} Hz/s = \frac{2\pi B}{T} rad/s^2 \tag{4.15}$$

with associated time-bandwidth product $BT = \beta_{LFM} T^2$. Since the LFM phase is known to be quadratic in time this waveform clearly requires a form of second-order implementation (a piecewise linear approximation to LFM using a first-order implementation was presented in [6]). Recalling (4.5), for an up-chirp at baseband the initial angle frequency is $-\pi/T_p$ and the final frequency at the end of the pulse is $+\pi/T_p$. The waveform therefore traverses a total angular frequency interval of $2\pi/T_p$ radians/s over the pulsewidth, for a bandwidth of $B = 1/T_p = N/T$ Hz. Substituting this result into (4.15) yields $\beta_{LFM} = N/T^2 Hz/s$ which, when converting to angular frequency and again using $T = NT_p$, realizes $\beta_{LFM} = 2\pi/NT_p^2 rad/s2$ that can be equated to the right side of (4.13) since LFM has a constant chirp-rate.

Thus, given the time-bandwidth product $BT \tilde{=} N$, an LFM up-chirp can be realized with the second-order implementation of (4.5) and (4.7) by setting $\bar{w_2} = -\pi/T_p$ and $b_n = 2\pi/N$ for $n = 1, 2, ...N$ and using a rectangular second-order shaping filter defined as $g_2(t) = (1/T_p^2) rect[0, T_p]$. Hence, the amount of angular frequency traversed during an interval of T_p seconds is $2\pi/NT_p$ rad/s. The constant chirp-rate code b_n combined with the rectangular shaping filter realizes a constant instantaneous chirp-rate via (4.13) and thus a linear instantaneous frequency in (4.10), which is as expected for an LFM waveform. Also, the initial phase term $\bar{\phi_2}$ from (4.5) is arbitrary.

Next, the generation of the same LFM waveform using a third-order implementation is being considered. With $\bar{w_3} = -\pi/T_p$ and $\bar{\phi_3}$ again being arbitrary, the obvious way would be to ignore the coding altogether ($c_n = 0$) by simply setting $\bar{\beta_3} = 2\pi/NT_p^2 rad/s2$. Alternatively, it is possible to set

$\bar{\beta}_3 = 0$ and determine the code values c_n and shaping filter g_3 that, when combined and integrated as in (4.14), will produce the constant LFM chirp rate. This result can be accomplished by taking the derivative of the second-order instantaneous chirp rate from (4.13), where the derivative of $g_2(t) = (1/T_p^2)rect[0,T_p]$ realizes a positive unit impulse function at $t = 0$, or $(1/T_p^2)\delta(t)$, and a negative unit impulse function at $t = T_p$, or $(-1/T_p^2)\delta(t - T_p)$. Thus an equivalent third-order shaping filter is

$$g_3(t) = (1/T_p^2)[\delta(t) - \delta(t - T_p)] \tag{4.16}$$

while the coding $c_n = b_n = 2\pi/N$ does not change. Because c_n is a constant, the bracketed term in (4.14) becomes

$$\sum_{n=1}^{N} c_n g_3(t - (n-1)T_p = \frac{2\pi}{NT_p^2}[\delta(t) - \delta(t - T)] \tag{4.17}$$

where all but the first and last impulses over the pulsewidth are cancelled. Fig.4.4 illustrates the normalized frequency content of the second-order and third-order implementations of an LFM waveform, which are identical as expected.

Where the first-order implementation of (4.1) can realize a piece-wise linear approximation to LFM, exact generation of LFM requires some modification to the first-order structure. Consider the modified first-order implementation

$$\phi_(1,mod)(t) = \int_0^t \left[\sum_{n=1}^{N} a_n h_1(t' - (n-1)T_p)\right] dt' + \int_0^t \bar{\omega}_1 dt' + \bar{\phi}_1, \tag{4.18}$$

which includes an initial frequency offset $\bar{\omega}_1$ and the new shaping filter $h_1(t - (n-1)T_p)$. Comparing (4.9) with (4.10) and (4.12) with 4.13, we find that an exact LFM can be generated using this modified first-order implementation by setting $a_n = b_n = 2\pi/N$ and $\bar{\omega}_1 = -\pi/N$ and defining the new shaping filter as

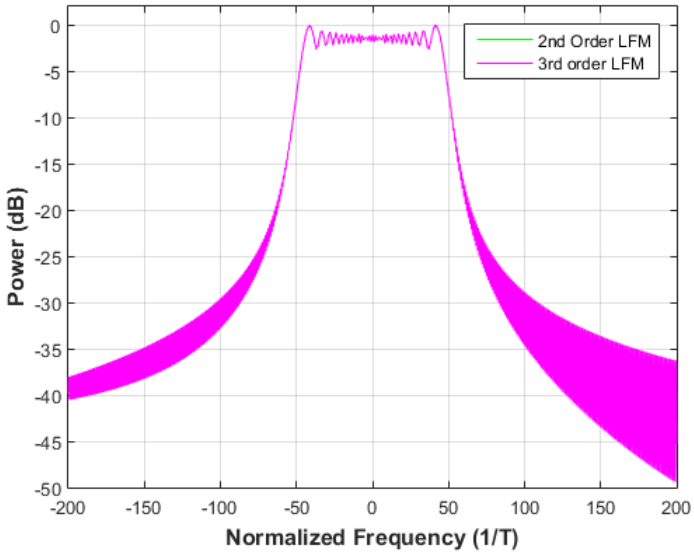

Figure 4.4: Spectral Content of second-order and third-order implementations of LFM with $BT = 100$

$$h_1(t-(n-1)T_p) = \int_0^t g_2(t'-(n-1)T_p)\,dt' \tag{4.19}$$
$$= (1/T_p^2)\int_0^t \text{rect}[(n-1)T_p, nT_p]\,dt'$$

which simplifies to the ramp function

$$h_1(t-(n-1)T_p) = \begin{cases} 0, & 0 \le t \le (n-1)T_p \\ (t-(n-1)T_p)/T_p^2, & (n-1)T_p \le t \le T_p \\ 1/T_p, & nT_p \le t \le NT_p \end{cases}, \tag{4.20}$$

Fig.4.4 illustrates the spectral content of this first-order ramp implementation that is, once again, found to be precisely that of an LFM waveform. In the next section, these LFM-based relationships will be used to establish that the second-order shaping filter should integrate to $1/T_p$ over the interval $[0, T_p]$.

The different implementations of the LFM waveform depicted in Fig.4.4 and Fig.4.5 represent special cases that establish how these implementations are related. However, the true utility in the different PCFM orders lies in the different continuous phase trajectories of physical waveforms that can be realized using finite first-, second-, or third-order codes and associated shaping filters. As such, the general structure of higher-order PCFM provides greater freedom to generate waveforms that possess desirable attributes.

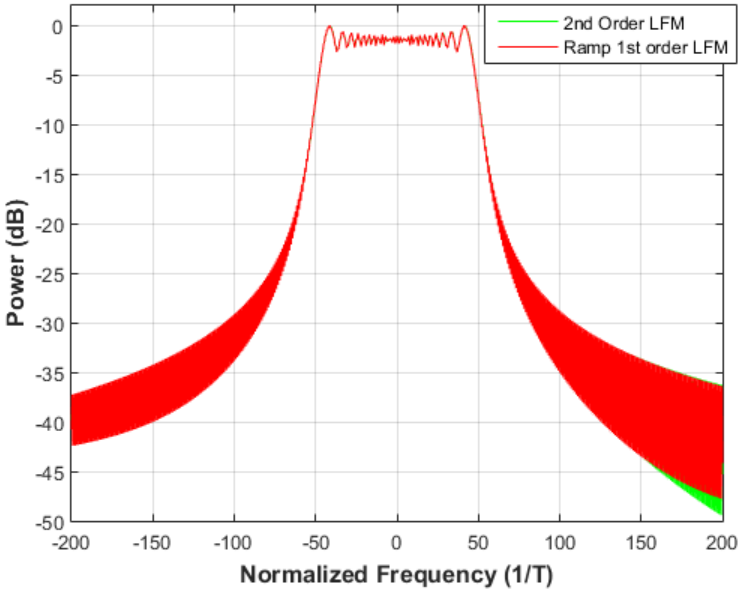

Figure 4.5: Spectral Content of second-order and first-order (RAMP) implementation of LFM with $BT = 100$

4.1.4 Permissible values for higher-order coding

As previously mentioned, additional care must be taken for higher-order coding with regard to selection of the code values. The permissible values of the first-order code a_n lie in $[-\pi, \pi]$ and these correspond to normalized instantaneous frequencies, which translate into the (angular) edge frequencies $\pm\pi/T_p$. To explore the permissible code values, the derivatives in (4.9)-(4.11) are likewise constrained as

$$-\pi/T_p \leq \sum_{n=1}^{N} a_n g_1(t-(n-1)T_p) \leq +\pi/T_p \tag{4.21}$$

$$-\pi/T_p \leq \int_0^t \left[\sum_{n=1}^{N} b_n g_2(t'-(n-1)T_p)\right] dt' + \bar{\omega}_2 \leq +\pi/T_p \tag{4.22}$$

and

$$-\pi/T_p \leq \int_0^t \int_0^{t'} \sum_{n=1}^{N} c_n g_3(t''-(n-1)T_p)\, dt''\, dt' + \int_0^t \bar{\beta}_3\, dt' + \bar{\omega}_3 \leq +\pi/T_p \tag{4.23}$$

Starting with the first-order case, the condition in (4.21) is met when $\max\{g_1(t)\} = (1/T_p)$. Given the previous stipulation that $g_1(t)$ integrate to unity over the time support $[0,T_p]$, the first-order code constraint is clearly met when $g_1(t) = (1/T_p)rect[0,T_p]$. Any other shaping filter besides rectangular that also integrates to unity over $[0,T_p]$ would exceed this constraint. Thus a first-order code bound for an arbitrary shaping filter that integrates to unity over $[0,T_p]$ is

$$[\frac{-\pi}{T_p max g_1(t)}] \leq a_n \leq [\frac{+\pi}{T_p max g_1(t)}] \tag{4.24}$$

For the second-order case, the instantaneous angular frequency during the nth code interval is being considered by expanding the derivative in (4.10) as

$$\begin{aligned}
\dot{\phi}_2((n-1)T_p \leq t \leq T_p) &= \int_0^t \left[\sum_{l=1}^{n} b_l g_2(t'-(l-1)T_p)\right] dt' + \bar{\omega}_2 \qquad (4.25)\\
&= \int_{(n-1)T_p}^{t} b_n g_2(t'-(n-1)T_p)]\, dt' + \int_0^{(n-1)T_p} \left[\sum_{l=1}^{(n-1)} b_l g_2(t'-(l-1)T_p)\right] dt' + \bar{\omega}_2\\
&= \int_{(n-1)T_p}^{t} b_n g_2(t'-(n-1)T_p)\, dt' + \omega_{2,n-1}
\end{aligned}$$

where

$$\begin{aligned}\omega_{2,n-1} &= \int_0^{(n-1)T_p} \Big[\sum_{l=1}^{(n-1)} b_l g_2(t'-(l-1)T_p)\Big]\,dt' + \bar{\omega}_2 \\ &= \left(\sum_{l=1}^{(n-1)} b_l\right)\left(\int_0^{T_p} g_2(t')\,dt'\right) + \bar{\omega}_2 \\ &= \left(\sum_{l=1}^{(n-1)} b_l\right) h_2(T_p) + \bar{\omega}_2 \\ &= \left(\sum_{l=1}^{(n-1)} b_l\right)\left(\frac{1}{T_p}\right) + \bar{\omega}_2\end{aligned} \tag{4.26}$$

is the angular frequency at the beginning of the nth code interval, with $\omega_{2,0} = \bar{\omega}_2$ for n = 1 and

$$h_2(t) = \begin{cases} 0, & t \le 0 \\ \displaystyle\int_0^t g_2(t')dt', & 0 \le t \le T_p \\ 1/T_p, & t \ge T_p \end{cases}, \tag{4.27}$$

Here, the various assumptions being made are 1) the integration of the shaping filter is the same for each code interval, 2) the finite time support of $g_2(t)$ on $[0, T_p]$ realizes a constant for $t \ge T_p$ when integrated, and 3) this constant value is $h_2(T_p) = 1/T_p$ for consistency with the second-order implementation of LFM. Likewise, evaluation of the integral in (4.25) over the nth code interval of $t \in [(n-1)T_p, nT_p]$ can be written as

$$\int_{(n-1)Tp}^{t} b_n g_2(t'-(n-1)T_p)\,dt' = b_n h_2(t-(n-1)T_p). \tag{4.28}$$

For instance, if $g_2(t) = (1/T_p^2)rect[0, T_p]$, then $h_2(t)$ would be the ramp function in (20). In general, assuming that $g_2(t)$ is non-negative for all t, then $\max\{h_2(t)\} = h_2(T_p) = 1/T_p$ due to monotonicity. Therefore, the second-order code constraint in (4.22) can be simplified to

$$-\pi/T_p \leq (1/T_p)b_n + (1/T_p)\left(\sum_{l=1}^{(n-1)} b_l\right) + \bar{\omega}_2 \leq +\pi/T_p, \tag{4.29}$$

yielding the permissible values for the nth element of the second-order code as

$$\left[-\pi - \left(\sum_{l=1}^{(n-1)} b_l\right) - T_p\bar{\omega}_2\right] \leq b_n \leq \left[+\pi - \left(\sum_{l=1}^{(n-1)} b_l\right) - T_p\bar{\omega}_2\right]. \tag{4.30}$$

As an illustrative example, the case of the second-order implementation of an LFM waveform as discussed in the previous section where $\bar{\omega}_2 = -\pi/T_p$ and $b_n = 2\pi/N$ is a constant for $n = 1, 2, ...N$ is considered. Using these parameters as initialization, (4.30) can be simplified to determine permissible values for subsequent optimization, where the nth code element could take on values in the interval

$$[\frac{-2\pi(n-1)}{N}] \leq b_n \leq [\frac{+2\pi(N-n+1)}{N}] \tag{4.31}$$

Specifically, for the first element $(n = 1)$ the constraint is

$$0 \leq b_n \leq +2\pi \tag{4.32}$$

and for the last element $(n = N)$ the constraint is

$$-2\pi\left(1 - \frac{1}{N}\right) \leq b_n \leq +2\pi\left(\frac{1}{N}\right). \tag{4.33}$$

Likewise, in the center ($n = N/2 + 1$, assuming N is even) the constraint is

$$-\pi \leq b_n \leq +\pi. \tag{4.34}$$

Collectively, (4.32), (4.33), and (4.34) imply that, depending on the starting frequency and previous (n-1) code values, the permissible values for b_n consist of an interval spanning 2π radians within the overall possible range of

$$-2\pi \leq b_n \leq +2\pi. \tag{4.35}$$

based on a hard constraint on frequency content as defined by (4.22).

Finally, for the third-order case, the derivative in (4.11) for the nth code interval is expanded as

$$\begin{aligned}\dot{\phi}_3((n-1)T_p \leq t \leq T_p) &= \int_0^t \int_0^{t'} \left[\sum_{l=1}^{n} c_l g_3(t'' - (l-1)T_p) \right] dt'' dt' + \int_0^t \bar{\beta}_3 \, dt' + \bar{\omega}_3 \\ &= + \int_0^t \int_0^{t'} \left[\sum_{l=1}^{(n-1)} c_l g_3(t'' - (l-1)T_p) \right] dt'' dt' + \bar{\beta}_3 t + \bar{\omega}_2 \\ &= \int_0^t \int_0^{t'} c_n g_3(t'' - (n-1)T_p)] \, dt'' dt' + \beta_{3,n-1} t + \omega_{3,n-1}\end{aligned} \tag{4.36}$$

where $\beta_{3,n-1}$ and $\omega_{3,n-1}$ will be defined shortly. Note that the integral over the previous $(n-1)$ code intervals can be expressed as

$$\begin{aligned}\int_0^t \int_0^{t'} \left[\sum_{l=1}^{(n-1)} c_l g_3(t'' - (l-1)T_p) \right] dt'' dt' &= \int_0^t \left[\sum_{l=1}^{(n-1)} c_l h_3(t' - (l-1)T_p) \right] dt' \\ &= \sum_{l=1}^{(n-1)} c_l f_3(t' - (l-1)T_p)\end{aligned} \tag{4.37}$$

in which

$$h_3(t) = \begin{cases} 0, & t \leq 0 \\ \displaystyle\int_0^t g_3(t')dt', & 0 \leq t \leq T_p \\ 1/T_p^2, & t \geq T_p \end{cases}, \tag{4.38}$$

noting the different constant for $h_3(t \geq T_p) = 1/T_p^2$ to remain consistent with the first-order and second-order formulations (and since there are still two additional integration stages). Subsequently, the final function in (4.37) has the general form

$$f_3(t) = \begin{cases} 0, & t \leq 0 \\ \int_0^t h_3(t')dt', & 0 \leq t \leq T_p \\ 1/T_p^2 + C, & t \geq T_p^2 \end{cases} , \tag{4.39}$$

with $C = \int_0^{T_p} h_3(t')dt' - 1/T_p$ to maintain continuity of f_3 at $t = T_p$. For example, if $g_3(t) = (1/T_p^3)rect[0, T_p]$, then $h_3(t)$ would again be a ramp function like in (4.20), albeit scaled by an additional factor of $1/T_p$. As a result,

$$f_3(t) = \begin{cases} 0, & t \leq 0 \\ t^2/(2T_p^3), & 0 \leq t \leq T_p \\ t/T_p^2 - 1/(2T_p), & t \geq T_p^2 \end{cases} \quad for \quad g_3(t) = (1/T_p^3)rect[0, T_p] \ , \tag{4.40}$$

In general, for $g_3(t)$ non-negative for all t like before, then the maximum value of $f_3(t)$ within the interval $[0, T_p]$ will be $\int_0^{T_p} h_3(t')dt' = \int_0^{T_p} \int_0^{t'} g_3(t'')dt''dt'$. For the rectangular shaping filter in (4.40), this maximum value is $0.5/T_p$, which will be used below.

For $t \geq T_p$, the function $f_3(t)$ increases linearly regardless of the particular shaping filter employed. In other words, since (4.37) represents the contribution to instantaneous frequency, it is observed that during the the nth code interval the previous code values c_1 to c_{n-1} introduce piecewise linear chirping components in addition to constant frequency offsets that can collectively be expressed as

$$\sum_{l=1}^{(n-1)} c_l f_3(t-(l-1)T_p) = \sum_{l=1}^{n-1} c_l \left[\left(t-(l-1)T_p \right)/T_p^2 - 0.5/T_p \right] \tag{4.41}$$
$$= \sum_{l=1}^{n-1} c_l \left[\left(t-(l-1)T_p \right)/T_p^2 \right] - \sum_{l=1}^{n-1} c_l \left[0.5/T_p \right]$$
$$= \left(\sum_{l=1}^{n-1} c_l \right) \left(t/T_p^2 \right) - \sum_{l=1}^{n-1} c_l \left[(l-0.5)/T_p \right]$$

Inserting (4.31) into (4.36) and associating the time-varying and constant frequency terms prior to the nth code interval therefore yields the preceding chirp-rate

$$\beta_{3,n-1} = \left(\sum_{l=1}^{n-1} c_l \right] \left(t/T_p^2 \right) + \bar{\beta}_3 \tag{4.42}$$

and angular frequency

$$\omega_{3,n-1} = \left(\sum_{l=1}^{n-1} c_l \right] \left(t/T_p^2 \right) + \bar{\omega}_3 \tag{4.43}$$

from the last line of (4.36), where $\beta_{3,0} = \beta_3$ and $\omega_{3,0} = \omega_3$ for $n = 1$. The remaining portion of (4.36) can likewise be expressed as

$$\int_0^t \int_0^{t'} c_n g_3(t''-(l-1)T_p)\, dt'' dt' = \int_0^t c_n h_3(t'-(n-1)T_p)\, dt' \tag{4.44}$$
$$= c_n f_3(t-(n-1)T_p)$$

Using this result along with (4.42) and (4.43), the instantaneous frequency from (36) becomes

$$\dot{\phi}_3((n-1)T_p \le t \le T_p) = c_n f_3(t-(n-1)T_p) + \left[\left(\sum_{l=1}^{n-1} c_l\right)\left(1/T_p^2\right) + \bar{\beta}_3\right] t \\ - \sum_{l=1}^{n-1} c_l \left[(l-0.5)/T_p\right] + \bar{\omega}_3 \tag{4.45}$$

Because the center (chirp) component is changing linearly while the first (coded) component changes nonlinearly, and assuming is non-negative for all t, the point of maximum possible frequency deviation during the nth code interval occurs at $t = nT_p$. Also using the result $f_3\left(T_p\right) = 0.5/T_p$ for the rectangular shaping filter, the hard frequency constraint from (4.23) becomes

$$-\pi/T_p \le 0.5c_n/T_p + \left[\left(\sum_{l=1}^{n-1} c_l\right)\left(t/T_p^2\right) + \bar{\beta}_3\right] nT_p - \sum_{l=1}^{n-1} c_l \left[(l-0.5)/T_p\right] + \bar{\omega}_3 \le +\pi/T_p \tag{4.46}$$

which can be rearranged to establish the permissible code values as

$$2\left[-\pi - \sum_{l=1}^{n-1}[n-l+0.5]c_l - \bar{\beta}_3 nT_p^2 - \bar{\omega}_3 T_p\right] \le c_n \le 2\left[+\pi - \sum_{l=1}^{n-1}[n-l+0.5]c_l - \bar{\beta}_3 nT_p^2 - \bar{\omega}_3 T_p\right] \tag{4.47}$$

In short, the second-order and third-order implementations involve successively more complex determination of their feasible code values. For the second-order case, this complexity involves a "frequency memory" term $\omega_{2,n-1}$ from (4.26). Likewise, for the third-order case, it involves $\omega_{3,n-1}$ from (4.43), as well as a "chirp memory" term $\beta_{3,n-1}$ from (4.42). These memory terms dictate the viability of later code values.

It is also important to note that the hard frequency constraints for the second-order and third-order implementations, originally stated in (4.22) and (4.23), are extensions of the first-order constraint and thus rely on an implicit assumption of constant frequency during a code element (time interval of T_p). However, these higher-order implementations clearly allow for changing frequency

during this interval. Thus for nonlinear chirp-like waveforms that tend to exhibit rapid frequency changes near the pulse edges (and which typify what are arguably the "best" waveforms in terms of low autocorrelation sidelobes based on a "conservation of ambiguity" notion [WD tutorial]), these hard constraints on higher-order code values should only be viewed as rough guidelines. In other words, these higher-order constraints can be relaxed as long as appropriate containment of the aggregate spectral content is maintained.

4.1.5 Aggregate spectral containment

While the higher-order constraints derived above provide a general sense of the feasible code values, a more practical way to ensure spectral containment is to constrain the aggregate spectral content of the whole waveform. For instance, in [14], the frequency template error (FTE) metric was defined which takes the form

$$\Phi_{FTE}\left[S(f)\right] = \left(\frac{1}{f_H - f_L}\right) \int_{f_L}^{f_H} \left| |S(f)|^p - |W(f)|^p \right|^q df \tag{4.48}$$

where $S(f)$ is the Fourier transform of PCFM waveform $s(t)$, according to some code parameterization, f_L and f_H demarcate the frequency interval of interest (including sufficient spectral roll-off beyond the 3-dB bandwidth), and $W(f)$ is a frequency weighting template such as a Gaussian window. The values p and q control the emphasis placed on in-band and out-of-band frequencies, with p = 1 and q = 2 defining a frequency-domain mean-square error (MSE) metric. Paraphrasing [65], a waveform having an aggregate spectral shape that decreases towards the band edges is known to also possess low autocorrelation sidelobes.

As discussed in [73] where the notion of PCFM "over-coding" is introduced, it is possible to exceed (even first-order) frequency constraints for a short amount of time as long as the aggregate spectral content still adheres to the desired spectral template. In reality, this idea is just an extension of the well-known principle of stationary phase conceived by the earliest developers of

nonlinear FM (NLFM) waveforms [[62], [63]] that states that the energy spectral density at a particular instantaneous frequency is inversely proportional to the chirp rate at that instant in time. More generally, one can say that the amount of time (relative to pulsewidth T) that a waveform resides in a given frequency directly relates to the relative amount of energy placed at that frequency. As such, where traditional NLFM waveform design has focused on the determination of nonlinear time-frequency functions [61] with which to implement the stationary phase principle, the parameterized PCFM structure permits use of various optimization methods to search for waveforms that achieve the desired aggregate spectral content. Of course, the time-frequency functions previously developed also provide very good starting points from which to initialize for further optimization.

4.1.6 Multi-order PCFM implementations

With the ability to generate higher-order PCFM waveforms as described in the previous sections, it is also possible to combine them in a multi-order formulation to take advantage of the additional design freedom while maintaining the same aggregate spectral content. For instance, the first-order and second-order schemes from (4.3) and (4.5), respectively, can be combined as

$$\phi_{21}(t) = \int_0^t \chi_1(t')dt' + \int_0^t \int_0^{t'} \chi_2(t'')\,dt''dt' + \int_0^t \bar{\omega}_{21}dt' + \bar{\phi}_{21} \tag{4.49}$$

for $\chi_1(t)$ and $\chi_2(t)$ the first-order and second-order coded signals defined in (4.2) and (4.7), respectively, and $\bar{\omega}_{21}$ and $\bar{\phi}_{21}$ the initial frequency and phase. Likewise, all three orders can be combined by incorporating (4.6) into (4.49) as

$$\begin{aligned}\phi_{321}(t) = &\int_0^t \chi_1(t')dt' + \int_0^t \int_0^{t'} \chi_2(t'')\,dt''dt' + \int_0^t \int_0^{t'} \int_0^{t''} \chi_3(t''')\,dt'''dt''dt' \\ &+ \int_0^t \int_0^{t'} \bar{\beta}_{321}\,dt''dt' + \int_0^t \bar{\omega}_{321}dt' + \bar{\phi}_{321}\end{aligned} \tag{4.50}$$

for $\chi_3(t)$ the third-order coded signals defined in (4.8) and with $\bar{\beta}_{321}$, $\bar{\omega}_{321}$, and $\bar{\phi}_{321}$ the initial chirp-rate, frequency, and phase.

The general form for the multi-order PCFM implementation is depicted in Fig.4.6, which could be used to implement any combination of these as well as single orders by simply setting the unused code(s) to zero. In light of the derivation of the code constraints and subsequent discussion regarding their complexity and relaxation in Section 4.1.4, it is clear that aggregate spectral content per Section 4.1.5 is an appropriate choice for the design of these multi-order waveforms.

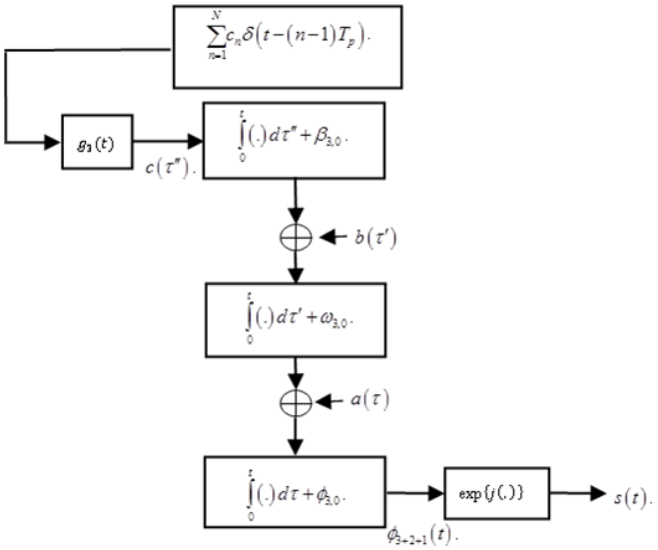

Figure 4.6: Multi-order PCFM waveform implementation

4.2 Higher-order PCFM Optimization

Optimization of the higher-order PCFM waveform codes necessitates a search of the high-dimensional space these codes parameterize according to some prescribed cost function, which generally involves some measure of the waveform ambiguity function (typically the zero-Doppler cut). In [14] the "performance diversity" paradigm was introduced that exploits the complementary nature of different ambiguity function metrics that specifically evaluate the waveform autocorrelation. These

metric are the peak sidelobe level (PSL), the integrated sidelobe level (ISL) metrics, and the FTE summarized in Section II.D. By leveraging these different, yet complementary metrics the performance diversity search is better able to avoid local minima associated with any single metric, thereby generally achieving better performance for all these metrics.

For waveform $s(t) = exp\{j\phi(t)\}$ according to one of the PCFM implementations from (4.1), (4.5), (4.6), (4.49), or (4.50), the autocorrelation (matched filter response) is

$$r(\tau) = \int_{t=0}^{T} s(t)s^*(t+\tau)\,dt \tag{4.51}$$

as a function of delay $-T \leq \tau \leq T$, with the interval $-\tau_m \leq \tau \leq \tau_m$ delimiting the mainlobe. For ease of reference, the PSL and ISL metrics are

$$PSL = \max_{\tau} \left| \frac{r(\tau)}{r(0)} \right| \quad for \quad \tau \in [\tau_m, T] \tag{4.52}$$

and

$$ISL = \frac{\int_{\tau_m}^{T} \left|r(\tau)\right|^2 d\tau}{\int_{0}^{\tau_m} \left|r(\tau)\right|^2 d\tau} \tag{4.53}$$

The performance diversity approach is used here to optimize the code parameters of the various PCFM implementations, with the additional requirement of determining the initial frequency and chirp-rate since, unlike the arbitrary initial phase, these factors do have an impact on waveform performance. In all cases the greedy search described in [14] is used, where at each stage the single code element whose change would provide the greatest improvement is updated, before the process is repeated.

For all cases, a time-bandwidth product of $BT \tilde{=} N = 100$ is used and the chosen FTE frequency

weighting template is a Gaussian window. Now, the performance diversity optimization process alternates between the metrics of PSL, ISL, and FTE from iteration to iteration using a predefined number of iterations until no further improvement is observed within each iteration when using each of this metric. Likewise, the higher-order implementations rely on this frequency template to ensure containment of the aggregate spectral content. In addition, the initial frequency for the waveform generated using the higher-order implementation is rescaled in the frequency domain so that the waveform will maintain its symmetry around the center frequency before comparing the result with the FTE metric.

4.2.1 Optimization of second/third-order PCFM implementations

For the following optimization results, the first-order case was initialized with a piece-wise LFM waveform that has been found [14] to yield good final results due to consolidation of delay-Doppler ambiguity into the delay-Doppler ridge (the "conservation of ambiguity" discussed in [71]). Leveraging the principle of stationary phase, the second-order waveform optimization is initialized with the scaled inverse of Taylor window coefficients possessing –40 dB range sidelobes. The piece-wise difference of these coefficients (approximating the derivative) was then used for the third-order initialization.

Fig.4.7 - 4.9 illustrate the autocorrelation, aggregate spectral content, and instantaneous frequency (or time-frequency function) for optimized first-order (red) and second-order (green) PCFM waveforms based on (4.1) and (4.5), respectively. In Fig.4.7, it is observed that the second-order waveform exhibits a PSL that is -2.5 dB lower than that of the first-order waveform. The spectral content (Fig.4.8) for the optimized second-order waveform is also found to exhibit a slightly broader roll-off from -15 dB down to about-40 dB. The latter effect can be explained by examining the instantaneous frequency (Fig.4.9), where the second-order waveform is shown to possess the rapid chirping behavior generally associated with waveforms designed according to the principle of stationary phase [[62], [63]]. It is observed, however, that unlike traditional smooth time-frequency

functions, the second-order PCFM instantaneous frequency exhibits small perturbations that serve to further break up sidelobe coherence. However, the second-order perturbations are much less pronounced than for the first-order case due the presence of an additional integration stage (per Fig.4.2) that smooths out such effects.

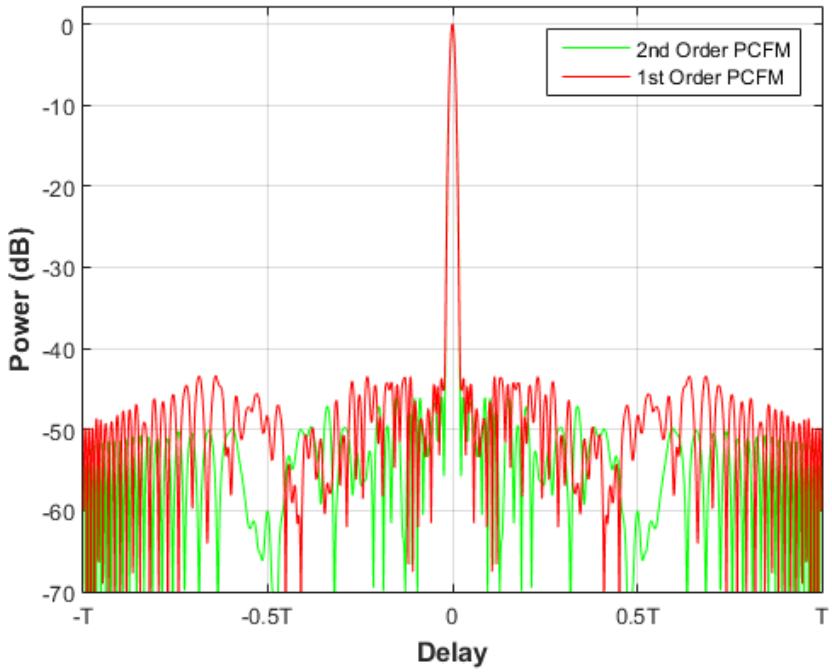

Figure 4.7: Autocorrelations of 1^{st} and 2^{nd} order optimized waveforms

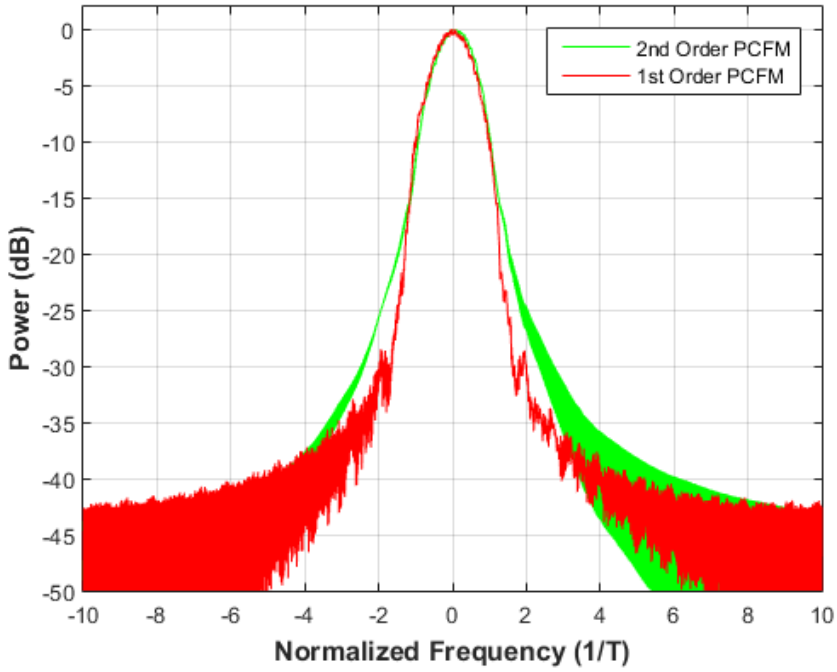

Figure 4.8: Spectral Content of 1^{st} order and 2^{nd} order optimized waveforms

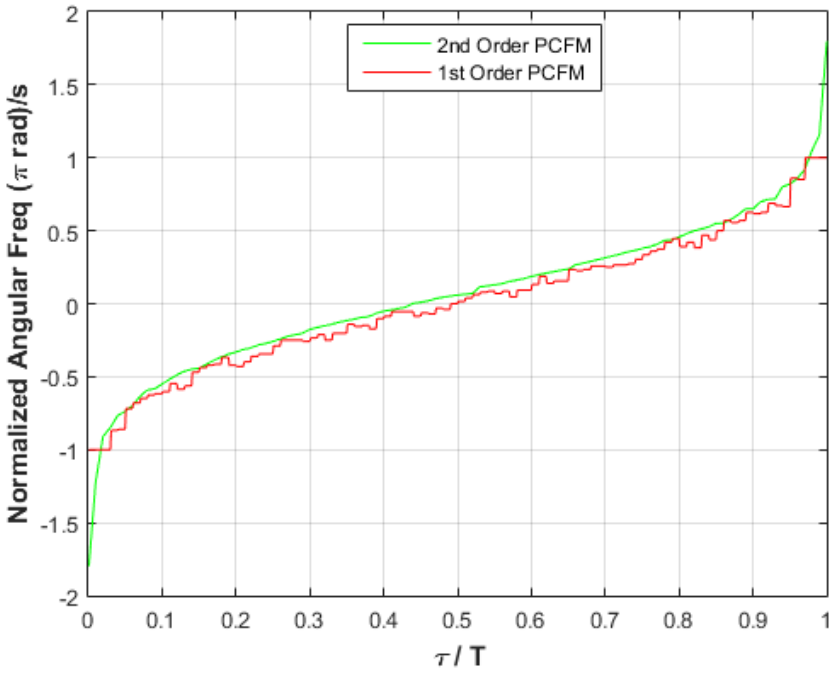

Figure 4.9: Instantaneous frequency of 1^{st} order and 2^{nd} order optimized waveforms

Fig.4.10 - 4.12 subsequently illustrate the autocorrelation, aggregate spectral content, and instantaneous frequency for an optimized third-order (blue) PCFM waveform based on (4.6), with the first-order waveform (red) also included again for comparison. Now, where the second-order waveform demonstrated a sidelobe reduction relative to first-order in Fig.4.7, Fig.4.10 shows that the third-order optimized waveform realizes some degradation (sidelobes increased by -5 dB). The spectral roll-off (Fig.4.11) for third-order does more closely match that of the first-order, albeit with a frequency-offset that arises due to the difficulty to optimize this rather complex waveform implementation. Recalling the implications of the principle of stationary phase, the reason for this frequency offset is observed in the instantaneous frequency plot (Fig.4.12) where the beginning of the waveform is found to exhibit a slower nonlinear chirping behavior than at the end of the waveform. Furthermore, the inclusion of another integration stage (now three) also produces an even smoother time-frequency function than either second-order or first-order, which serves to restrict the ability of small perturbations to break up sidelobe coherence.

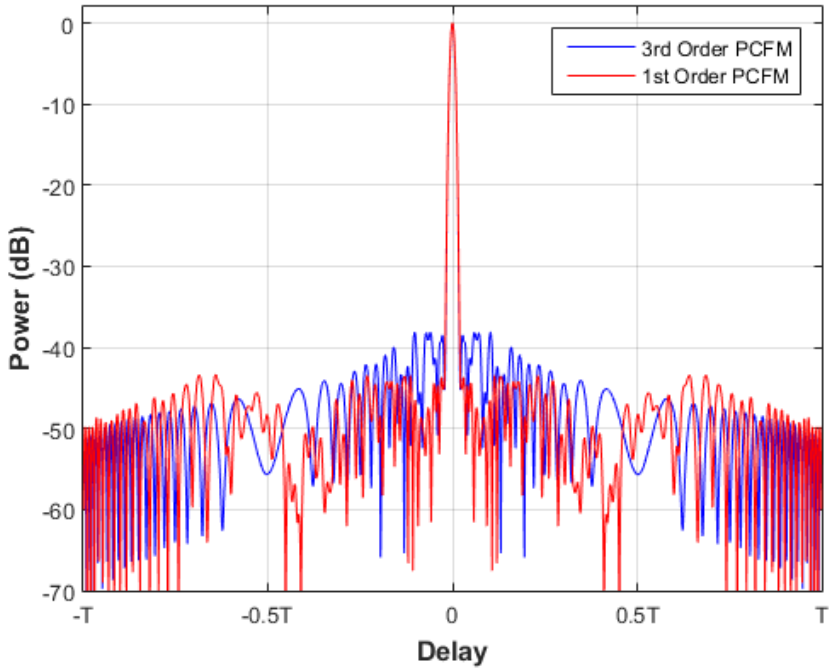

Figure 4.10: Autocorrelations of 1^{st} and 3^{rd} order optimized waveforms

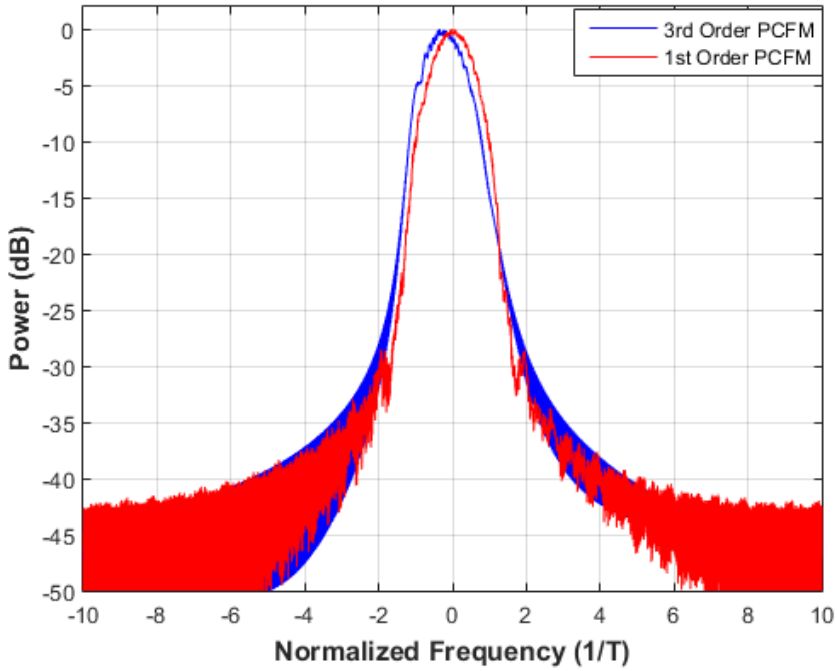

Figure 4.11: Spectral Content of 1^{st} order and 3^{rd} order optimized waveforms

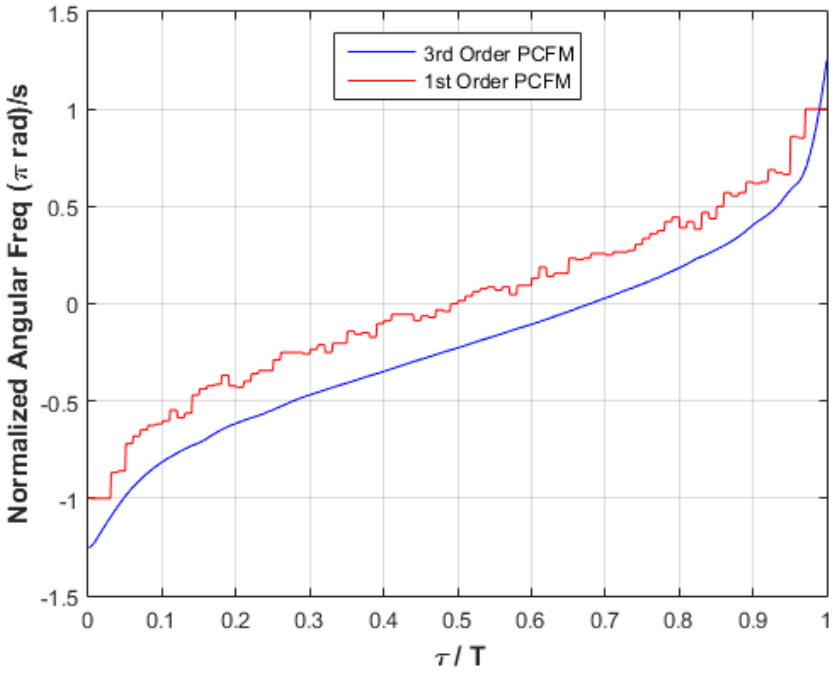

Figure 4.12: Instantaneous frequency of 1^{st} order and 3^{rd} order optimized waveforms

Table 4.1 quantifies the PSL and ISL values for the optimized first-order, second-order, and third-order waveform implementations with $BT = 100$, for B the 3-dB bandwidth. As a useful benchmark, the PSL bound for hyperbolic FM (HFM) waveforms $(-20log10(BT) - 3dB$ [[65]]) with the same BT is also included. As observed previously in [14], the first-order implementation is able exceed the HFM bound by a small margin. The second-order implementation, however, surpasses the bound by 3 dB. Although the 3-dB bandwidth remains constant across these three implementations, it is revealed in Fig.4.9 that the second-order case achieves this improvement in part due to a greater frequency function bandwidth caused by the sharp nonlinear chirping at the beginning and end of the waveform (about 1.8× greater) that translates into the modest broadening observed in the aggregate spectrum. The associated HFM bound for that increased bandwidth is -48.1 dB.

Table 4.1: PSL & ISL for 1^{st}, 2^{nd} and 3^{rd} order optimized waveforms for $BT = 100$

	1^{st} **order**	2^{nd} **order**	3^{rd} **order**	**HFM bound**
PSL (dB)	-43.4	-46.0	-38.1	-43.0
ISL (dB)	-59.5	-63.5	-57.4	N/A

4.2.2 Optimization of multi-order PCFM implementations

Using (4.49) and (4.50), the optimization of the multi-order PCFM implementations of the same $BT = 100$ dimensionality is being considered. For joint optimization, either both (for first/second-order combined) or all three of the codes are designed according to the same greedy search as above (and in [14]) in which the single code element whose change would provide the greatest improvement is updated at each stage. At the same time, the sequential optimization is also being considered whereby the different order codes are each optimized until no further improvement is possible (with the other codes set to 0 initially) and then that code is fixed while the optimization of a different code commences. Not surprising, given the results above, it has been found that starting with the second-order code, followed by either the first-order or third-order codes, generally

provides the best performance in terms of sidelobe reduction.

Fig.4.13 - 4.15 depict the autocorrelation, spectral content, and instantaneous frequency, respectively, for joint optimization of (4.49) and (4.50). Both cases realize PSL values (Fig.4.13) that are nearly 8 dB better than the previous first-order result and 5 dB better than the second-order result. The shape of the spectral content (Fig.4.14) is basically the same as the previous cases, with a small asymmetry caused by inclusion of the third-order coding likewise present. Finally, the usual "sideways S" shape is again observed for the instantaneous frequency, with extensions of the frequency function bandwidth of factors of $2\times$ and $2.25\times$ for the first/second combined orders and first/second/third combined orders, respectively. These bandwidths correspond to respective HFM PSL bounds of -49.0 dB and -50.0 dB. Per Table 4.2, it is interesting to note that the PSL values achieved by these multi-order waveforms still surpass these bounds, an effect that can likely be largely attributed to the presence of the first-order perturbations observed in Fig.4.15 that serve to break up sidelobe coherency and arise naturally from the optimization process.

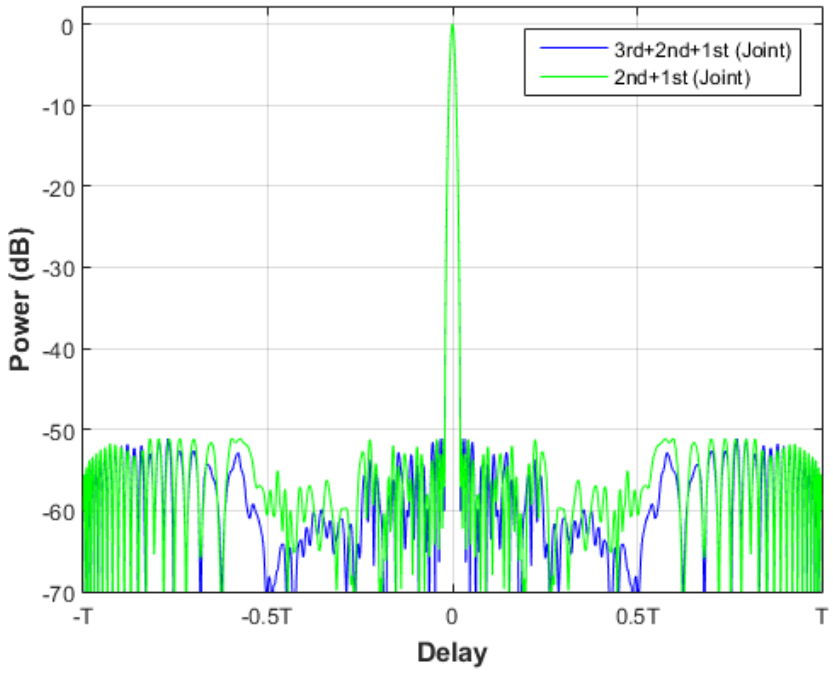

Figure 4.13: Autocorrelations of jointly optimized waveforms via (4.48) and (4.49)

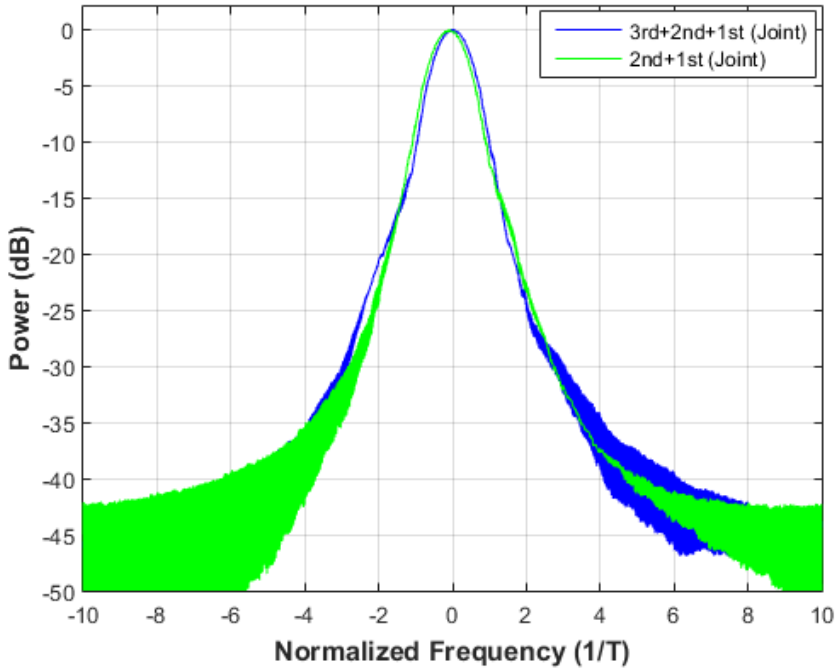

Figure 4.14: Spectral Content of jointly optimized waveforms via (4.48) and (4.49)

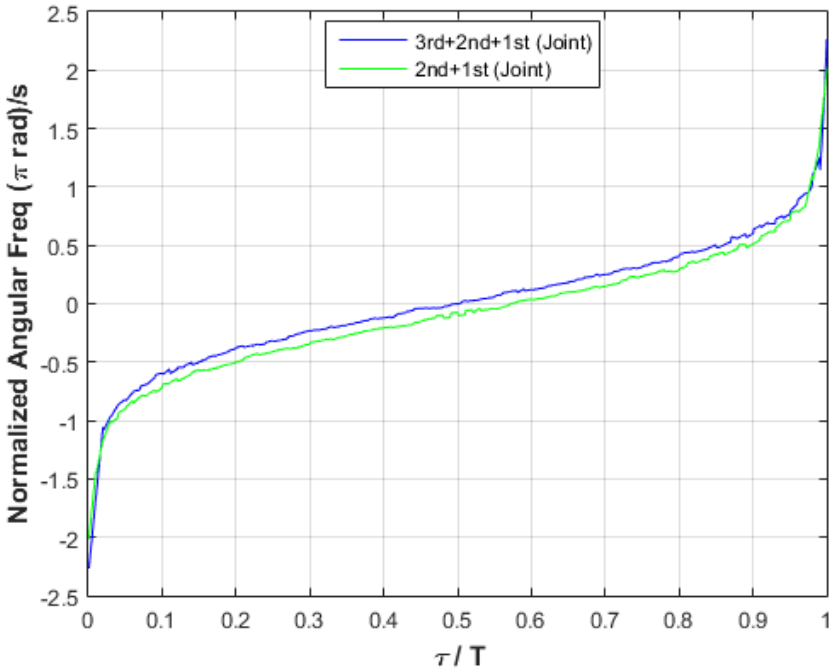

Figure 4.15: Instantaneous frequency of jointly optimized waveforms via (4.48) and (4.49)

Table 4.2: PSL & ISL for SEQ. and JOINT Optimization of Multiple Orders for $BT = 100$

	Joint. 1^{st} **&** 2^{nd} **orders**	**Joint** 1^{st}**,** 2^{nd} **&** 3^{rd} **orders**	**Seq.** 1^{st} **&** 2^{nd} **orders**	**Seq.** 1^{st}**,** 2^{nd} **&** 3^{rd} **orders**
PSL (dB)	-51.1	-51.1	-50.7	-51.2
ISL (dB)	-66.4	-67.9	-66.0	-66.8

Plots for sequential optimization are not included because they are negligibly different from joint optimization, as evidenced by their PSL and ISL values in Table 4.2. However, the sequential optimization is more computationally efficient to implement since it does not require a greedy search over all the codes at each stage.

Finally, the delay-Doppler ambiguity function for the jointly optimized multi-order PCFM waveforms defined in (4.49) and (4.50) are depicted in Fig.4.16 and Fig.4.17. As expected, by basing on the rather similar instantaneous frequency functions for these two waveforms (Fig.4.15), their ambiguity functions are quite similar as well. As seen from the plots, both exhibit the prominent delay-Doppler ridge that is typical of chirp-like waveforms as well as the surrounding Fresnel lobes. While not to the same degree as LFM, these waveforms still provide some Doppler tolerance.

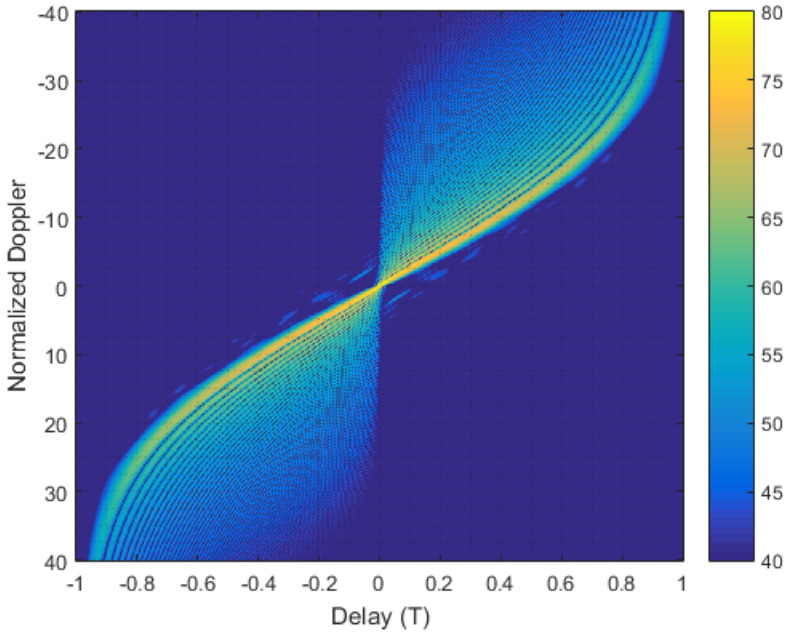

Figure 4.16: Delay-Doppler ambiguity function
for optimized multi-order PCFM waveform via (4.49)

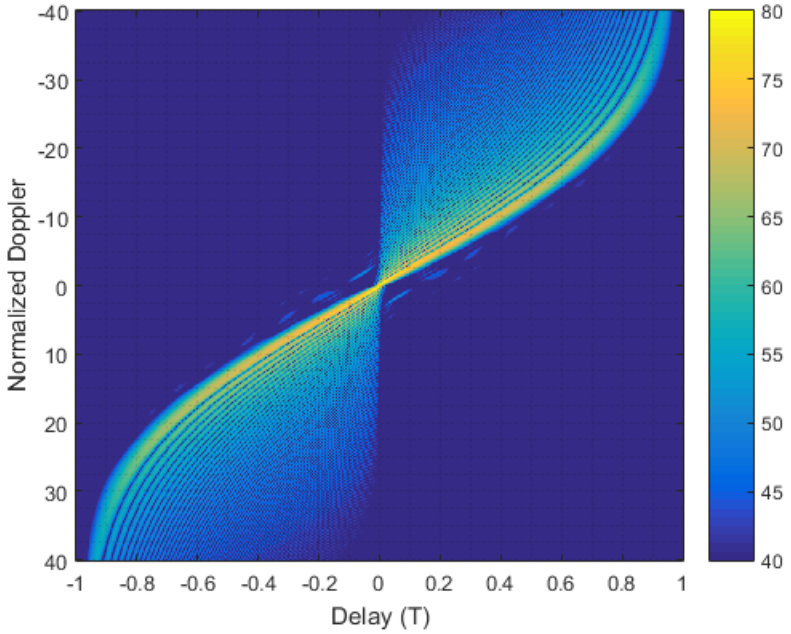

Figure 4.17: Delay-Doppler ambiguity function
for optimized multi-order PCFM waveform via (4.50)

4.3 Review of results from Higher-order PCFM waveforms

In this Chapter, it can be seen that the polyphase-coded FM (PCFM) framework for radar waveform implementation/optimization, which was previously derived from continuous phase modulation (CPM) used in communication, can be viewed as a first-order waveform representation as compared to the zeroth-order representation of a polyphase code by itself. The results that are obtained and discussed have shown that higher-order schemes can also be employed as a means to obtain more degrees of freedom for waveform design ([12],[97]-[98]). Presently, the second-order PCFM implementation tends to provide the best performance in terms of sidelobe reduction of the standalone single-order schemes. Multi-order implementation may likewise be employed to provide even better PSL/ISL performance. Finally, the mathematical relationships between these different orders has been demonstrated and subsequently used to derive general guidelines for selection of higher-order code values according to spectral containment constraints.

Chapter 5

Applying Sparse Spectrum Allocation (SSA) results to Practical Radar Applications

As this stage, it has been shown that both Part 1 and 2 of the two-step approach have separately produced good results to address and mitigate the issues of both Spectral Congestion and Spectral Sharing between radar and communication systems. In this Chapter, the results obtained from both approaches will be utilized for practical implementations of radar system applications.

In section one, the results from the Sparse Spectrum Allocation (SSA) algorithm will be used to generate various composite PCFM waveforms in which each composite waveform is the sum of various PCFM waveforms that are generated at each of the disjointed segments in the sparse spectrum allocated to the radar system. In section two, the results obtained from the SSA algorithm will then be applied to a radar target range profile estimation application on various scenarios that contain a mixture of both dominant scatterers and weak scatterers along the target radar range profile. The outcome from both sections will illustrate the feasibility of applying the results obtained from both Part 1 and 2 of the two-step approach in this dissertation for practical radar system implementations.

5.1 Applying SSA results to physical-realizable PCFM waveform implementation

In this section, results obtained from SSA algorithm corresponding to three scenarios of sparse spectrum usage by the radar system will be used for generating PCFM waveforms that bears a one-one correspondonce to each of these three scenarios. The objective of this section is to illustrate the practicality of applying the results of SSA algorithm for generating physical radar waveforms.

5.1.1 Definition of Spectrum Usage Scenarios for PCFM waveform

As a start, the details of the three scenarios of sparse spectrum usage that are selected under this section are provided as follows:

- Scenario one in which the radar system uses 25% of the available spectrum content while releasing the remaining 75.0% portion of the spectrum for reallocation to other user systems
- Scenario two in which the radar system uses 40% of the available spectrum content while the remaining 60.0% portion are released for reallocation to other user systems
- Scenario three in which the radar system uses 72.5% of the available spectrum content while the remaining 27.5% portion are released for reallocation to other user systems

In each of these scenarios, two types of plots will be generated to compare the performance from the SSA results (designed as unmodulated radar waveform in this section) with the results generated via the PCFM framework after applying the corresponding spectrum usage from the SSA algorithm (designed as PCFM waveform). These plots are namely, the autocorrelation or matched filter response as well as the spectrum usage of both unmodulated versus PCFM modulated waveforms.

5.1.2 PCFM waveform generation for Scenario One - 25% usage of radar spectrum

For the first scenario, the results obtained from the SSA algorithm based on the spectrum usage of 25.0% as well as frequency block size of 2.50% with the frequency sample location results as shown in Fig. 3.48 will be used as the spectrum to generate the PCFM waveform in this example. By examining Fig. 5.1 which is a replot of Fig. 3.48 with the x-axis extended beyond the highest frequencies in both ends of the full spectrum, it is observed that the allocated spectrum consists of two disjointed segments with the first segment occupying a spectrum width of 5.00% and the second segment occupying a spectrum width of 20.00%. As such, it will be possible to construct a PCFM waveform that correspond to each of the two disjointed spectrum segments.

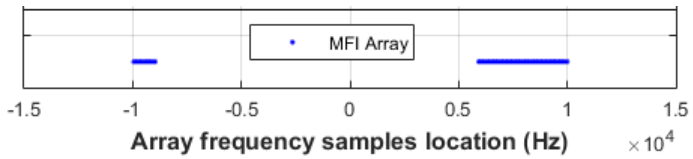

Figure 5.1: Frequency sample locations using blocksize of 2.50% for 25% spectrum usage (Unmodulated waveform)

Now, from chapter 4 of this dissertation, it is stated that the relationship between time-bandwidth product BT and the number of chip codes N in the PCFM waveform is well approximated by the expression $BT = N$. As such, if a variable N_f is assigned for the number of chip codes corresponding to full contiguous spectrum, then it is possible to assign two other variables N_1 and N_2 to represent the number of chip codes for the two PCFM waveforms that will correspond to the proportion of each disjointed spectrum segment as shown in Fig. 5.1. Also, the three variables N_f, N_1 and N_2 are related by the following equation (5.1)

$$N_f = \frac{1}{0.25} \times \left(N_1 + N_2\right) \tag{5.1}$$

Also, since both PCFM waveforms will be present throughout the full pulsewidth duration T,

thus, this will mean that the chip duration T_p for each chip code of the two PCFM waveforms will also be different as compared to the scenarios described in the previous chapter when using the relationship of $T = NT_p$.

Next, for this section, the first-order representation of the PCFM waveform is chosen to illustrate the feasibility of using the SSA results to implement a physical realizable radar waveform. As such, the corresponding first-order coded function and the first-order phase function for each of the two PCFM waveforms are defined in (5.2) to (5.5)

$$\chi_1(t) = \sum_{n=1}^{N_1} a_n g_1(t-(n-1)T_{p1}) \tag{5.2}$$

$$\chi_2(t) = \sum_{n=1}^{N_2} b_n g_1(t-(n-1)T_{p2}) \tag{5.3}$$

$$\phi_1(t) = \int_0^t \chi_1(t')dt' + \bar{\phi}_1. \tag{5.4}$$

$$\phi_2(t) = \int_0^t \chi_2(t')dt' + \bar{\phi}_2. \tag{5.5}$$

Subsequently, the two PCFM waveforms and the composite PCFM waveform that is generated by the sum of these two PCFM waveforms (as shown in Fig. 4.1 for each waveform) are given as:

$$s_1(t) = exp^{j\phi_1 t} \tag{5.6}$$

$$s_2(t) = exp^{j\phi_2 t} \tag{5.7}$$

$$s_{composite}(t) = s_1(t) + \sqrt{\frac{N_2}{N_1}} s_2(t) \tag{5.8}$$

Note that the scaling factor of $\sqrt{(N_2/N_1)}$ is needed to ensure that the second PCFM waveform $s_2(t)$ is able to maintain the same spectral power as the first PCFM waveform $s_1(t)$ within each of their allocated spectrum in the frequency domain since both waveforms are transmitted using the same pulse duration T in time.

Next, by assigning the variables $N = 200$, $N_1 = 10$ and $N_2 = 40$, the plots of both spectrum shape and matched filter response generated from the composite PCFM waveform $s_{composite}$ are compared to that generated from using the unmodulated waveform and these plots are as shown in Fig. 5.2 and Fig. 5.3 respectively. Note that the results obtained from the composite PCFM waveform consist of both the pre-optimized first-order frequency codes $\chi_{initial}(t)$ that are initialized using the piece-wsie LFM waveform ([14]) as well as the post-optimzed first-order frequency codes $\chi_{optimized}(t)$ that are optimized using the performance-diversity scheme as described in chapter 4.

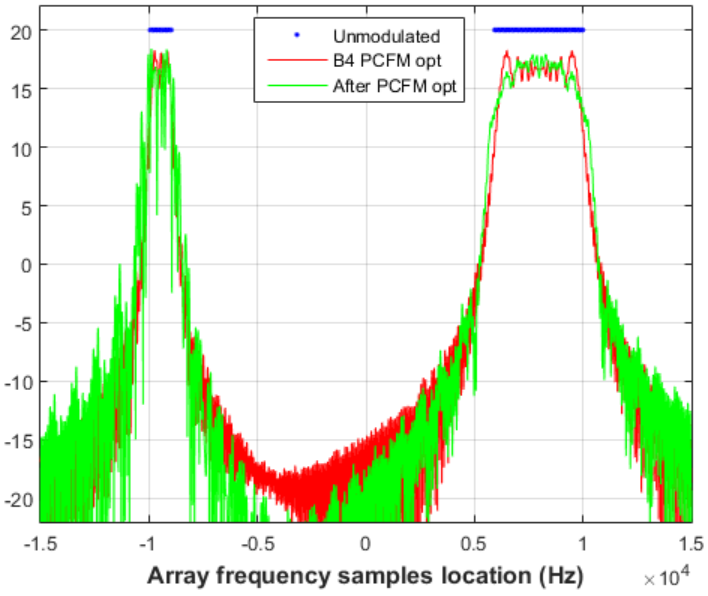

Figure 5.2: Comparison of spectrum usage between Unmodulated waveform versus PCFM waveform (before and after PCFM optimization)

From Fig. 5.2, it is observed that the spectrum usage of both pre-optimized and post-optimized PCFM waveforms match closely with the spectrum usage of the unmodulated waveform obtained

using the SSA scheme. For instance, within the region of spectrum that are meant to be assigned for reallocation to other systems, it is observed that the PCFM waveform do not contain transmit any significant amount of spectral power in this "forbidden" spectrum band. At the same time, within the two spectrum segments ("passbands" demarcated using the blue lines)that are assigned for the PCFM waveform, the transmit spectrum power is almost constant in these regions. Thus, the results of the spectrum shapes from the PCFM waveforms that are shown in Fig. 5.2 illustrates the viability of using the SSA results for generating physical realizable radar waveforms

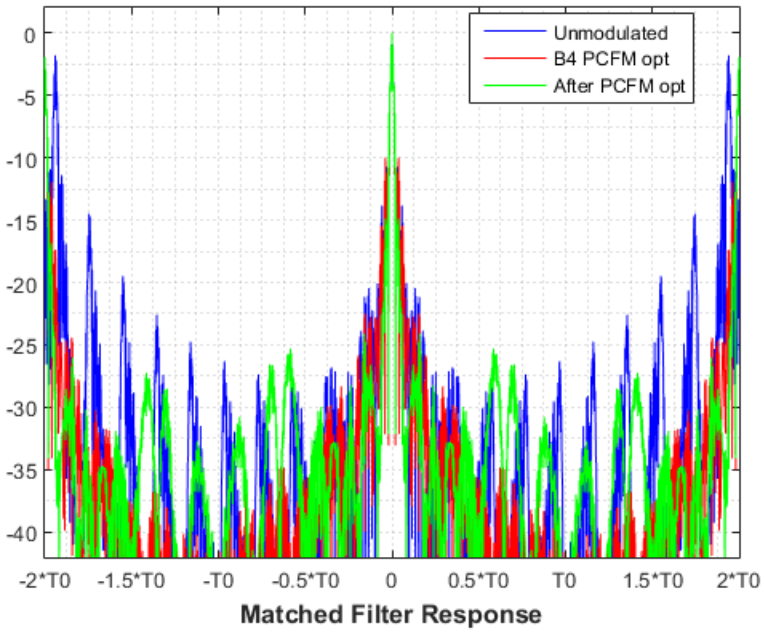

Figure 5.3: Matched Filter Response between Unmodulated waveform versus PCFM waveform (before and after PCFM optimization)

Next, by examining Fig. 5.3, it is observed that the post-optimized PCFM waveform does provide some improvements as compared to both unmodulated and pre-optimized PCFM waveforms in terms of lowering the sizelobe levels near to the mainlobe region at the expense of higher sidelobe levels further away from the mainlobe. Thus, there is some slight performance gain that can be obtained by performing the PCFM optimization process to the composite PCFM waveform generated from the two PCFM waveforms initialized using piece-wise LFM waveform.

5.1.3 PCFM waveform generation for Scenario Two - 40% usage of radar spectrum

For the second scenario, the results obtained from the SSA algorithm based on the spectrum usage of 40.0% as well as frequency block size of 2.50% will be used as the spectrum to generate the PCFM waveform in this second example. By examining Fig. 5.4 which shows the frequency sample location results with the x-axis extended beyond the highest frequencies in both ends of the full spectrum, it is observed that the allocated spectrum consists of four disjointed segments with these four segments occupying a spectrum of [2.50%, 7.50%, 25.00%, 5.00%] respectively with a small spectrum gap of 1.30% present between the third and fourth segment. Again, it will be possible to construct a PCFM waveform that correspond to each of the four disjointed spectrum segments.

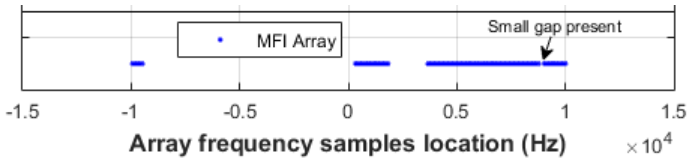

Figure 5.4: Frequency sample locations using blocksize of 2.50% for 40% spectrum usage (Unmodulated waveform)

Now, for the second example, the five variables N_f, N_1, N_2, N_3 and N_4 are related by equation (5.9).

$$N_f = \frac{1}{0.40} \times \left(N_1 + N_2 + N_3 + N_4\right) \tag{5.9}$$

Likewise, the corresponding first-order coded function, the first-order phase function for each of the four PCFM waveforms are defined in (5.10) to (5.17)

$$\chi_1(t) = \sum_{n=1}^{N_1} a_n g_1(t-(n-1)T_{p1}) \tag{5.10}$$

$$\chi_2(t) = \sum_{n=1}^{N_2} b_n g_1(t-(n-1)T_{p2}) \tag{5.11}$$

$$\chi_3(t) = \sum_{n=1}^{N_3} c_n g_1(t-(n-1)T_{p3}) \tag{5.12}$$

$$\chi_4(t) = \sum_{n=1}^{N_4} d_n g_1(t-(n-1)T_{p4}) \tag{5.13}$$

$$\phi_1(t) = \int_0^t \chi_1(t')dt' + \bar{\phi}_1. \tag{5.14}$$

$$\phi_2(t) = \int_0^t \chi_2(t')dt' + \bar{\phi}_2. \tag{5.15}$$

$$\phi_3(t) = \int_0^t \chi_3(t')dt' + \bar{\phi}_3. \tag{5.16}$$

$$\phi_4(t) = \int_0^t \chi_4(t')dt' + \bar{\phi}_4. \tag{5.17}$$

Finally, the equation for the composite PCFM waveform that is generated by the sum of the four PCFM waveforms is given as:

$$s_{composite}(t) = exp^{j\phi_1 t} + \sqrt{\frac{N_2}{N_1}} exp^{j\phi_2 t} + \sqrt{\frac{N_3}{N_1}} exp^{j\phi_3 t} + \sqrt{\frac{N_4}{N_1}} exp^{j\phi_4 t} \tag{5.18}$$

Next, by assigning the variables $N = 200$, $N_1 = 5$ and $N_2 = 15$, $N_3 = 50$ and $N_2 = 10$, the plots of both spectrum shape and matched filter response generated from the composite PCFM waveform $s_{composite}$ are compared to that generated from using the unmodulated waveform and these plots are as shown in Fig. 5.5 and Fig. 5.6 respectively.

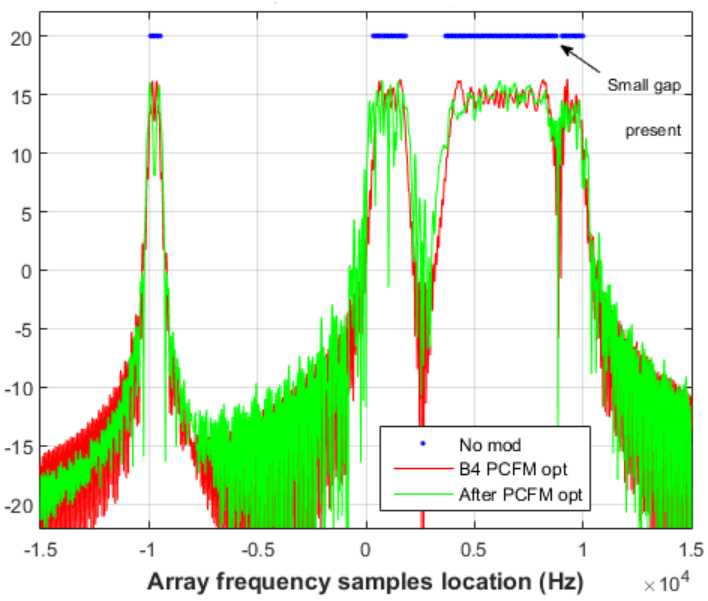

Figure 5.5: Comparison of spectrum usage between Unmodulated waveform versus PCFM waveform (before and after optimization)

From Fig. 5.5, it is observed that for the first two spectral segments covering 2.50% and 7.50% of spectrum usage by the radar system, the spectral energy from the corresponding pre-optimized PCFM waveforms are well contained within the assigned spectrum bands and thus it will be feasible to reallocate the spectral gap width of 49.0% between these two segments for another system's usage. Similarly, for the second significant spectral gap of around 9.00% between the second and third PCFM waveforms, there is also very minimal spectral leakage from the second and third pre-optimized PCFM waveforms into this second spectral gap. However, after undergoing PCFM waveform optimization, there are more spectral leakage from post-optimized PCFM waveforms into the two significant spectral gaps although the leakage is still very insignificant within the larger spectral gap of 49.0%. Thus, it is still feasible to reallocate the larger spectral gap for other system's usage even when the radar system is transmitting the post-optimized composite PCFM waveform.

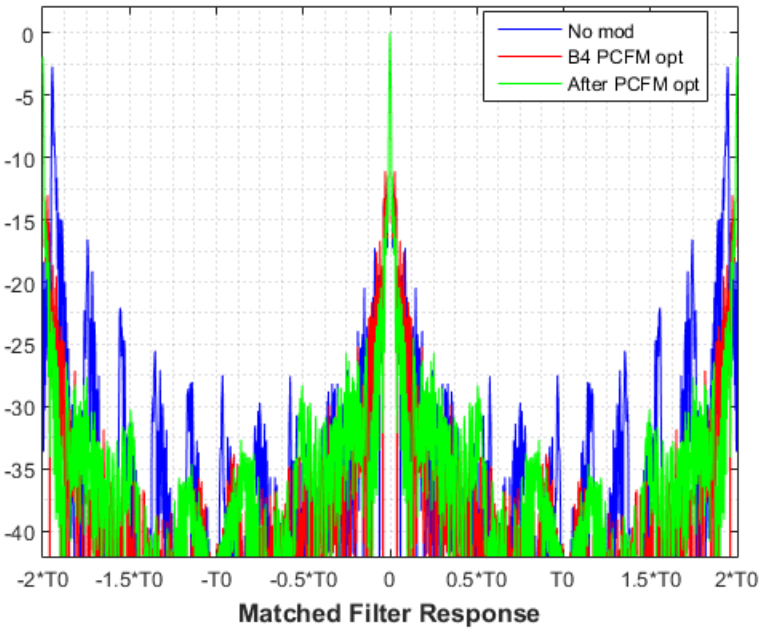

Figure 5.6: Matched Filter Response between Unmodulated waveform versus PCFM waveform (before and after optimization)

Finally, by examining Fig. 5.6, it can be seen again that the post-optimized PCFM waveform does provide some improvements as compared to both unmodulated and pre-optimized PCFM waveforms in terms of lowering the sizelobe levels near to the mainlobe region at the expense of higher sidelobe levels further away from the mainlobe. Therefore, this result again merits the additonal step of performing PCFM waveform optimization.

5.1.4 PCFM waveform generation for Scenario Three - 72.5% usage of radar spectrum

For the third scenario, the results obtained from the SSA algorithm based on the spectrum usage of 72.5% as well as frequency block size of 2.50% as shown in Fig. 5.7 is used as the spectrum to generate the PCFM waveform in this final example. From Fig. 5.7, it is observed that the radar allocated spectrum consists of four disjointed segments with these segments occupying a spectrum of [25.00%, 20.00%, 12.50%, 15.00%] respectively for a total spectrum usage of 72.50% and with

a small spectrum gap of 0.825% present between the first and second segment. As per the second example scenario, it is again possible to construct a PCFM waveform that correspond to each of the four disjointed spectrum segments.

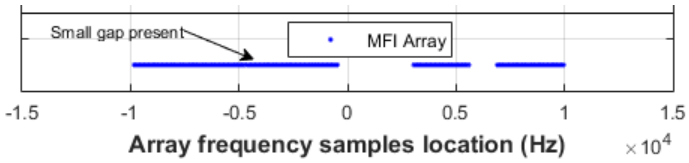

Figure 5.7: Frequency sample locations using blocksize of 2.50% for 72.5% spectrum usage (Unmodulated waveform)

As is the case for the second example, in this third example, the five variables N_f, N_1, N_2, N_3 and N_4 are related by equation (5.19) below.

$$N_f = \frac{1}{0.725} \times \left(N_1 + N_2 + N_3 + N_4\right) \tag{5.19}$$

Next, by assigning the variables $N = 200$, $N_1 = 50$ and $N_2 = 40$, $N_3 = 25$ and $N_2 = 30$, the plots of both spectrum shape and matched filter response generated from the composite PCFM waveform $s_{composite}(t)$ are compared to that generated from using the unmodulated waveform and these plots are as shown in Fig. 5.8 and Fig. 5.9 respectively on the following page.

Lastly, as per (5.18), the equation for the composite PCFM waveform that is generated by the sum of the four PCFM waveforms using the above values for N_f, N_1, N_2, N_3 and N_4 is given as:

$$s_{composite}(t) = exp^{j\phi_1 t} + \sqrt{\frac{N_2}{N_1}} exp^{j\phi_2 t} + \sqrt{\frac{N_3}{N_1}} exp^{j\phi_3 t} + \sqrt{\frac{N_4}{N_1}} exp^{j\phi_4 t} \tag{5.20}$$

where the equations to generate the four phase functions $\phi_1(t)$, $\phi_2(t)$, $\phi_3(t)$ and $\phi_4(t)$ are defined as per equations (5.10) to (5.17).

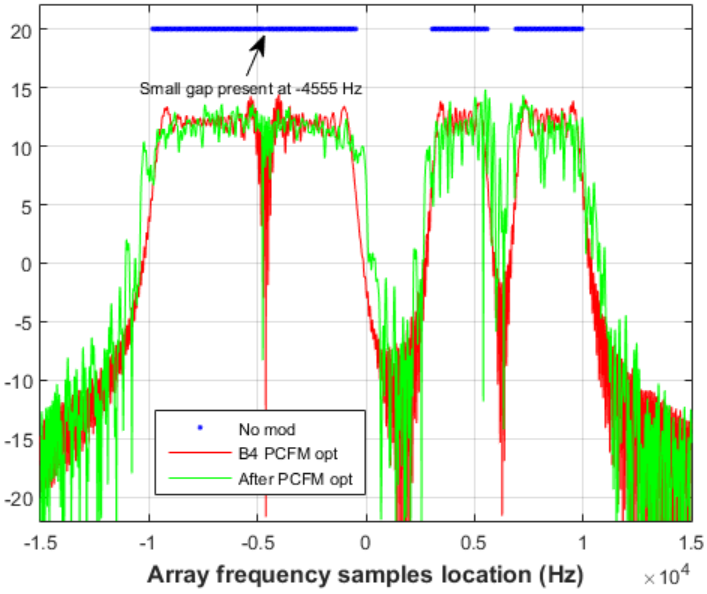

Figure 5.8: Comparison of spectrum usage between Unmodulated waveform versus PCFM waveform (before and after optimization)

From Fig. 5.8 as shown above, as per the previous two example scenarios, the spectral energy from the corresponding pre-optimized PCFM waveforms are well contained within the assigned spectrum bands and thus it is again feasible to reallocate the two largest spectral gap widths of 17.50% and 6.50% for another system's usage. However, after undergoing PCFM waveform optimization, there are more spectral leakage from the post-optimized PCFM waveforms into the second significant spectral gap of 6.50% although the leakage is still not insignificant within the larger spectral gap of 17.5%. Thus, it is still feasible to reallocate the larger spectral gap for other system's usage even when the radar system is transmitting the post-optimized composite PCFM waveform.

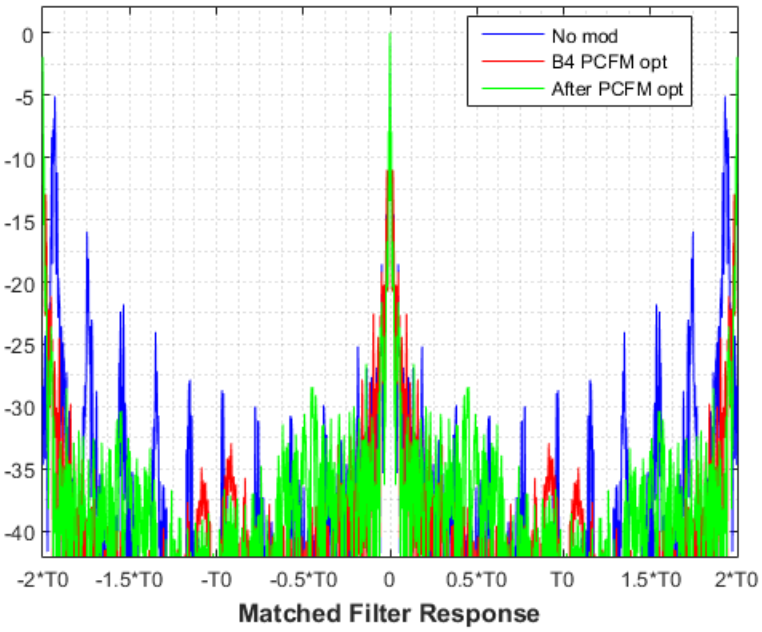

Figure 5.9: Matched Filter Response between Unmodulated waveform versus PCFM waveform (before and after optimization)

Finally, by examining Fig. 5.9, the same trend is observed in that the post-optimized PCFM waveform does provide some improvements as compared to both unmodulated and pre-optimized PCFM waveforms in terms of lowering the sizelobe levels near to the mainlobe region at the expense of higher sidelobe levels further away from the mainlobe. Once again, the results provides merits in performing PCFM waveform optimization to the composite waveform.

5.2 Applying SSA results to estimation of Radar Range Profile γ

In this section, results obtained from the SSA algorithm corresponding to three scenarios of sparse spectrum usage by the radar system will be used in defining a radar target estimation application. The objective is to demonstrate the feasibility of applying the SSA results to common radar applications such as the unambiguous radar range profile estimation.

5.2.1 Definition of Spectrum Usage Scenarios and Target setup for Radar Range Profile Estimation

As a start, the three scenarios of sparse spectrum usage that are defined under this subsection are as follows:

- Scenario one of spectrum usage in which the radar system uses 25.00% (K_1) of the available spectrum content.
- Scenario two of spectrum usage in which the radar system uses 50.00% (K_2) of the available spectrum content.
- Scenario three of spectrum usage in which the radar system uses 75.00% (K_3) of the available spectrum content.

Following the definition of the scenarios of sparse spectrum usage above, the next step is to define the number of strong and weak target scatterers present within the radar range profile (Target delay spectrum) for each of these spectrum usage scenarios. Again, three target scenarios are defined as follows:

- Target scenario one in which the number of strong and weak target scatterers occupy 6.25% (L_1) of the full unambiguous radar range profile (M) with the target locations within the

range profile determined via a random permutation. Also, the power of the largest strong target scattering coefficient is almost 40.00 dB and the power of the weakest target scattering coefficient is close to -50.00 dB

- Target scenario two in which the number of dominant and weak target scatterers occupy 3.25% (L_2) of the full unambiguous radar range profile with the locations being a subset of those locations from the first target scenario. Also, the power of both strong and weak target scatterers falls within the limits specified in the first target scenario.

- Target scenario three in which the number of dominant and weak target scatterers occupy 1.75% (L_3) of the full unambiguous radar range profile with the locations being a subset of those locations from the first target scenario. Also, the power of both strong and weak target scatterers falls within the limits specified in the first target scenario.

Next, the magnitude of all strong and weak target scattering coefficients are generated by using a log uniform distribution that spans the wide range of values between the strong and weak targets. At the same time, the phase of each target is also generated using a Gaussian distirbution that spans $[0, 2\pi]$. In addition, the locations within the radar range profile that do not contain either strong or weak target scatterer, i.e. clutter locations, are also filled using very small complex values in the order of -30.0 dB in magnitude. Also, the equations to generate the magnitude and phase of the target vector γ_{L_i} of size L_i and the clutter vector clu of size $(M - L_i)$ are given below:

$$exponent - tgt = -3.00 + 5.00 \times (rand_{uniform}(L_i)) \tag{5.21}$$

$$mag - tgt = 10^{exponent - tgt} \tag{5.22}$$

$$phase - tgt = 2\pi \times (rand_{uniform}(L_i)) \tag{5.23}$$

$$\gamma_{L_i} = (mag - tgt) \times exp^{j(phase-tgt)} \tag{5.24}$$

$$clu = \frac{1}{10^3} \times (rand_{normal}(M - Li) + jrand_{normal}(M - Li)) \tag{5.25}$$

where $rand_{uniform}$ is the uniform distribution function over the open interval $(0,1)$ and $rand_{normal}$ is the Gaussina distribution function with mean of zero and variance of one.

Finally, the resultant target vector γ that will be used to form the frequency measurement vector **v** as given in (3.3) and repeated below as (5.26) will be equal to the concantenation of the two vectors γ_{L_i} and clu so that the length of γ will be equal to M.

$$\mathbf{v} = \mathbf{H}\gamma + \mathbf{n} \tag{5.26}$$

Also, a summary of all the various radar's sparse spectrum usage as well as the target parameters for each of the nine scenarios that are defined above is provided in Table 5.1 below.

Table 5.1: Specifications of Spectrum Usage and Target Parameters

	Sc. 1	**Sc. 2**	**Sc. 3**	**Sc. 4**	**Sc. 5**	**Sc. 6**	**Sc. 7**	**Sc. 8**	**Sc. 9**
Spectrum (%)	25.0	25.0	25.0	50.0	50.0	50.0	75.0	75.0	75.0
# Tgts (%)	6.25	3.25	1.75	6.25	3.25	1.75	6.25	3.25	1.75
$\lvert\gamma_{max}\rvert^2$ (dB)	39.8	39.8	39.8	39.8	39.8	39.8	39.4	39.8	39.8
$\lvert\gamma_{min}\rvert^2$ (dB)	-48.7	-48.3	-48.3	-48.7	-48.3	-48.3	-48.7	-48.3	-48.3

Besides defining both spectrum usage and target scenarios, to ensure that the simulation scenario setup is representing a realistic radar operational scenario, a complex gaussian noise vector **n** with average power of -50.00 dB is being added to the frequency measurement vector **v** as shown in (5.26) above.

5.2.2 Iterative MMSE Estimator for Radar Range Profile Estimation

In this subsection, the detailed description for the MMSE estimator that will be applied to the frequency measurement vector **v** to extract the estimated radar range profile (target delay spectrum) $\tilde{\gamma}$ will be provided in the following paragraphs. As a start, the equations for defining the MMSE estimator as well as the computation of the estimated $\tilde{\gamma}$ and error covariance matrix $\mathbf{K}_{\varepsilon}$ are given in (5.27), (5.28) and (5.29) below:

$$\mathbf{W}_{MMSE} = \mathbf{K}_{\gamma}\mathbf{H}'(\mathbf{H}\mathbf{K}_{\gamma}\mathbf{H}' + \mathbf{K}_{n})^{-1} \tag{5.27}$$

$$\tilde{\gamma} = \mathbf{W}_{MMSE}\mathbf{v} \tag{5.28}$$

$$\mathbf{K}_{\varepsilon} = (\mathbf{H}'\mathbf{K}_{n}^{-1}\mathbf{H} + \mathbf{K}_{\gamma}^{-1})^{-1} \tag{5.29}$$

Now, as shown from (5.28), it is possible to obtain an estimate of the full radar range profile γ by using the one-step procedure defined by this equation. However, in situations at which the size of the full (target+clutter) dimension (equal to M) is much greater than that of the size (K_i) of the measurement vector, this one-step procedure will generate many errors in estimating γ. Subsequently, this will result in either many false alarms or missed detections of the real targets of interest (including both strong and weak targets) among the clutter interference. For instance, in all three scenarios of sparse spectrum usage, the amount of measurements are equal to [25.0%, 50.0%, 75.0%] of the (target+clutter) dimension space.

To resolve the issues of false alarms as well as missed detections, a iterative form of the MMSE estimator is proposed in this subsection for estimating the full radar range profile. Essentially, the steps of the iterative MMSE estimator are as follows:

- Step One of this iterative MMSE estimator is by applying the MMSE estimator to the mea-

surements as shown in (5.28). Following that, the task within this step is to identify the target scattering coefficient γ_i among all M targets in the range profile that has the largest magnitude. For tracking purpose, this target location is termed t_1 and the value of the target scattering coefficient γ_{t_i} is assumed to hold the true value of the target at this location. Finally, the a priori target covariance matrix $\mathbf{K}_\gamma$ for all M locations in the radar range profile is updated by using the equation defined in (5.30) below.

$$\mathbf{K}_\gamma = \mathbf{I} \odot \{\tilde{\gamma}\tilde{\gamma}'\} + \mathbf{I} \odot \mathbf{K}_\varepsilon \tag{5.30}$$

where I is the identity matrix and $\odot$ is the Hadamard product

- Step Two of this iterative MMSE estimator will be to apply the MMSE estimator to just estimate the set of all combinations of two target scattering coefficients with each two-target combination consisting of the tracked target location t_1 along with a second target location i where $i \in [1, M]$. From the set of M combinations of the estimated two-element $\tilde{\gamma}_2$, the second target location to be identified is the location that has the largest magnitude among all the M locations excluding t_1. For tracking purpose, this target location is termed t_2 and the estimated values of the target scattering coefficients $[\gamma_{t_2}, \gamma_{t_2}]$ are assumed to hold the true values of the targets at the locations $[t_1, t_2]$. Finally, the a priori target covariance matrix $\mathbf{K}_\gamma$ for all M locations in the radar range profile is updated by using the equation defined in (5.30).

- Going further, Step P of this iterative MMSE estimator will be to apply the MMSE estimator to just estimate the set of all combinations of P target scattering coefficients with each P-target combination consisting of the tracked target locations $[t_1, t_2, ..., t_{P-1}]$ along with the p^{th} target location i where $i \in [1, M]$. From the set of M combinations of the estimated P-element $\tilde{\gamma}_P$, the p^{th} target location to be identified is the location that has the largest magnitude among all the M locations excluding $[t_1, t_2, ..., t_{P-1)}]$. For tracking purpose, this target location is termed t_P and the estimated values of the target scattering coefficients $[\gamma_{t_1}, \gamma_{t_2}, ..., \gamma_{t_P}]$ are

assumed to hold the true values of the targets at these locations. Finally, the a priori target covariance matrix $\mathbf{K}_\gamma$ for all M locations in the radar range profile is updated by using the equation defined in (5.30).

- Finally, the iteration can stop any time depending on the convergence status of the average MSE of all M targets in the error covariance matrix $\mathbf{K}_\varepsilon$

In the next subsection, the iterative MMSE estimator will be applied to each of the nine scenarios listed in Table 5.1 so as to compare the results of the $\tilde{\gamma}$ obtained from these scenarios with the actual values of γ that are used to form v.

5.2.3 Results of Radar Range Profile Estimations for all scenarios

In this subsection, the results obtained from estimating γ by using the iterative MMSE estimators will be analysed for the performance obtained in each scenario. In order to perform an quantatative analysis, for each of the nine spectrum usage and target scenarios, three different plots will be generated to evaluate the performance of the results obtained for both the dominant and weak target scatterers present in the radar range profile. The three plots to be generated are as follows:

- Plot of estimated power of strong targets, weak targets and clutter objects versus the actual values of these entities

- Plot of the error covariance computed for each element within $\tilde{\gamma}$ after the final iteration. These values are obtained from the diagonal of the error covariance matrix $\mathbf{K}_\varepsilon$

- Plot of the average MSE computed as the mean of the diagonal of the error covariance matrix $\mathbf{K}_\varepsilon$ versus the average MSE computed from the difference between $\tilde{\gamma}$ and actual values of γ. The equations for computing these two parameters are provided in (5.31) and (5.32) below.

$$MSE_{K_\varepsilon} = \frac{1}{M} \times Tr\left(\mathbf{K}_\varepsilon\right) \tag{5.31}$$

$$MSE_{gnd-truth} = \frac{1}{M} \times \left[(\gamma - \tilde{\gamma})'(\gamma - \tilde{\gamma}) \right] \tag{5.32}$$

In the next few subsections, the results from each scenario will be discussed in the numerical order as specified in Table 5.1.

5.2.3.1 Results from Scenario One to Scenario Three with 25.0% of Spectrum usage

Under this subsection, the same amount of spectrum usage of 25.0% is applied to three different target scenarios, namely, from average (6.25%) to very low target density (1.75%) within the radar range profile for the radar range profile estimation application. Also, the iterative MMSE estimator is programmed to run up to M iterations such that the estimated scattering coefficents of all the locations within the radar range profile are assumed to hold the true value of the target scatterers in these locations. As a start, the three plots for the first target scenario of target density of 6.25% present in the radar range profile are shown in Fig. 5.10 - 5.12 in the following pages.

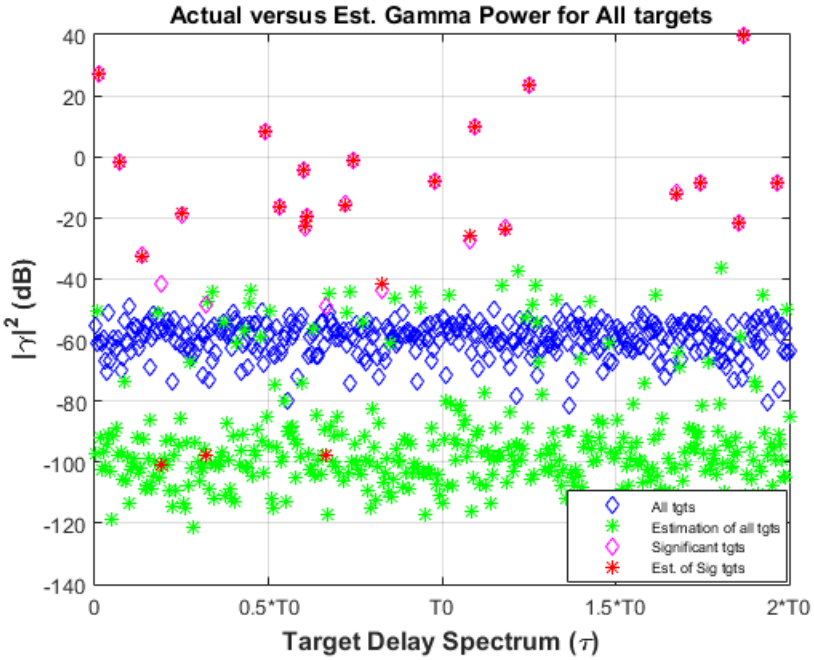

Figure 5.10: Actual versus Est. γ for All targets (tgt density of 6.25%)

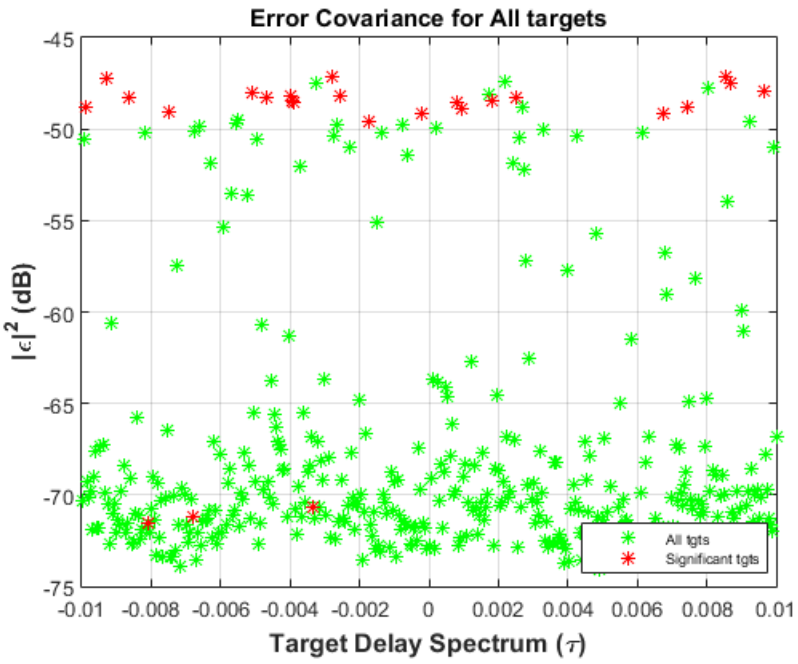

Figure 5.11: Error Covariance for All targets (tgt density of 6.25%)

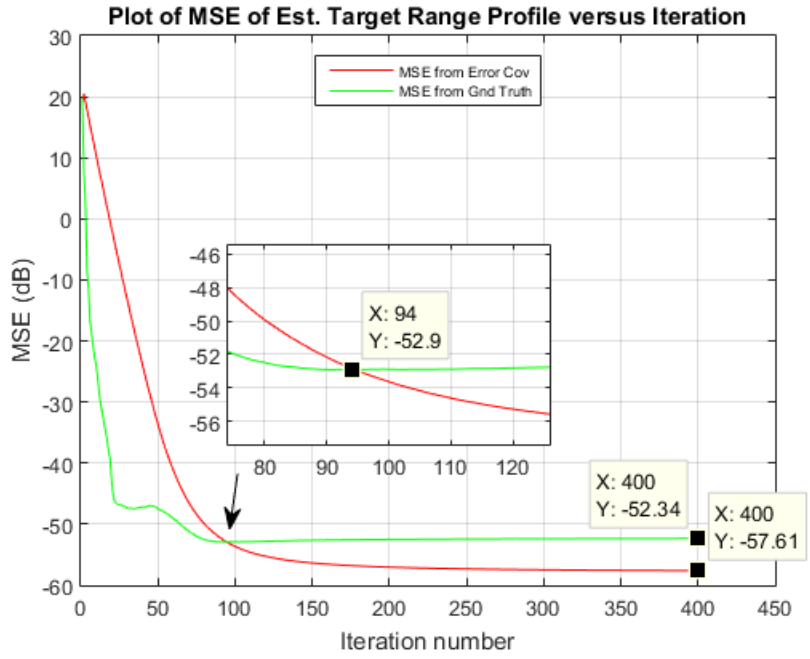

Figure 5.12: Plot of MSE of Est Radar Range Profile versus MMSE Iteration (tgt density of 6.25%)

As a start, by examining Fig. 5.10, it is seen that out of 25 strong and weak target scatterers indicated by the magneta "diamond" symbol, the estimated γ values (red "asterisk" symbol) from 3 out of the four weakest target scatterers with power below -41.0 dB are erroneous and only one of these four weak target scatterer (-43-8 dB) has an estimated scattering coefficent value that is almost the same as the actual value. Thus, these three weakest targets will end up as missed targets when the estimated $\tilde{\gamma}$ is passed through a Constant False Alarm Rate (CFAR) detector. In addition, there are also some clutter locations that possess estimated γ values)green "asterisk" symbol) above -40 dB and these clutter locations may also result in false alarms after a CFAR detector is applied to the estimated results of the radar range profile.

Next, by examining Fig. 5.11, it can be seen that the iterative MMSE estimator has performed very well in estimating the values of γ for both strong and weak targets such that the final values of the error variance for each of these targets are below -47.0 dB. Thus, although the amount of spectrum usage is only 25.0% for this example, it is seen that the application of iterative MMSE estimator is still able to correctly estimate almost 90.0% of all the targets that are present in the radar range profile.

Thirdly, by examining Fig. 5.12, it is observed that the iterative MMSE estimator has obtained convergence of the results at around iteration number 200 as shown by the red line plot in the figure and thus the Δ change of the MSE_{K_ε} from one iteration to the next iteration can serve as a stopping criteria for the iterations of the MMSE estimator.

Next, the results obtained from the iterative MMSE estimator when it is applied to the second and third target scenario of low to very low target density within the radar range profiles while still using the same spectrum usage of 25.0% are shown in Fig. 5.13 - 5.18 as follows.

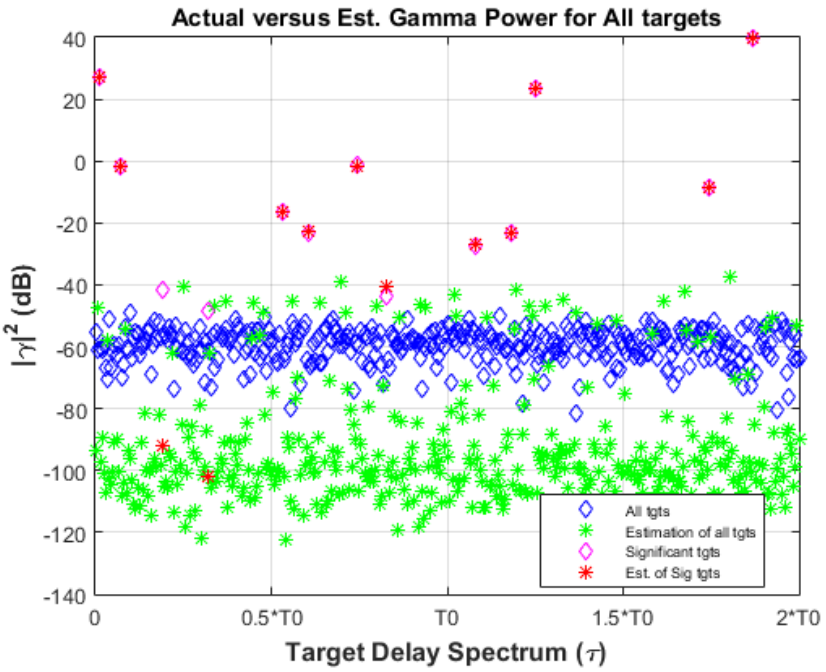

Figure 5.13: Actual versus Est. γ for All targets (tgt density of 3.25%)

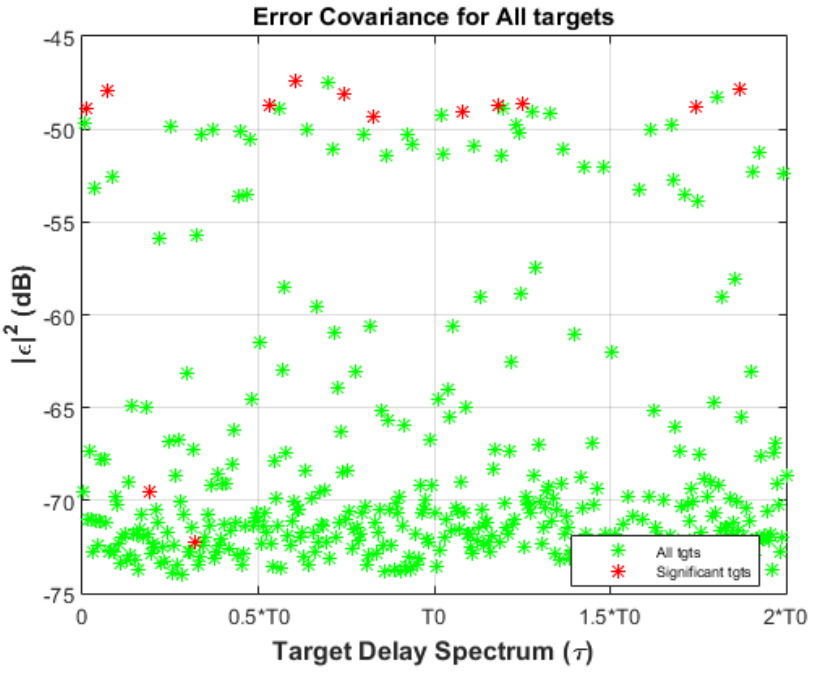

Figure 5.14: Error Covariance for All targets (tgt density of 3.25%)

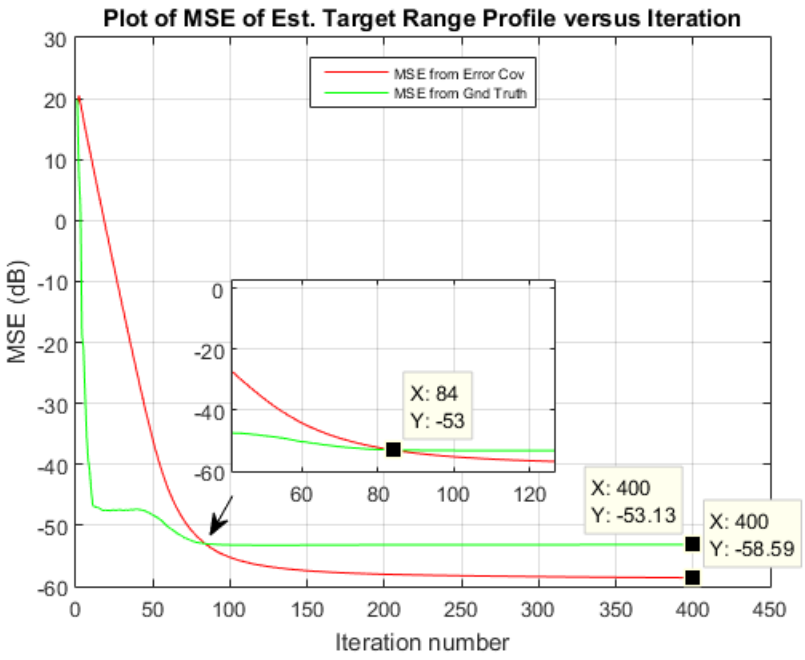

Figure 5.15: Plot of MSE of Est Radar Range Profile versus MMSE Iteration (tgt density of 3.25%)

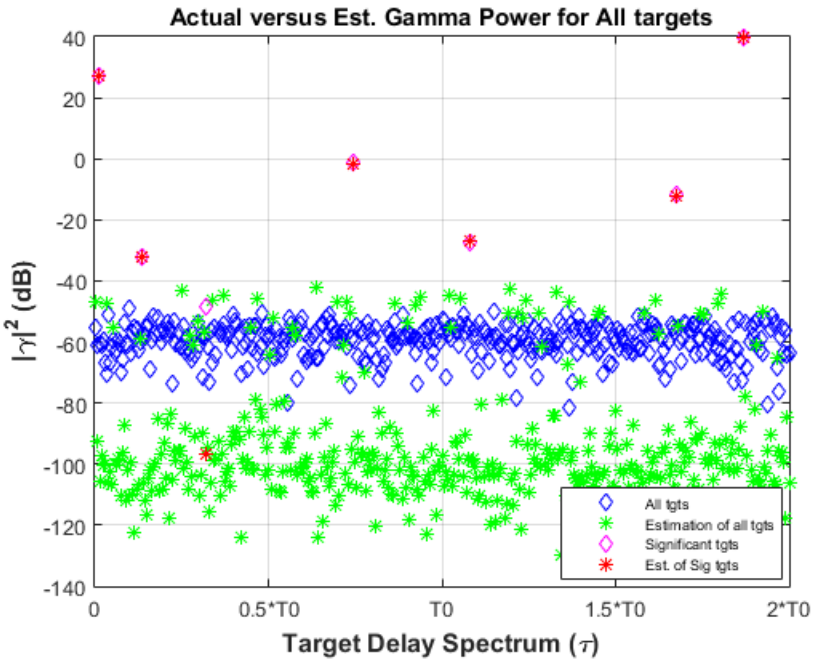

Figure 5.16: Actual versus Est. γ for All targets (tgt density of 1.75%)

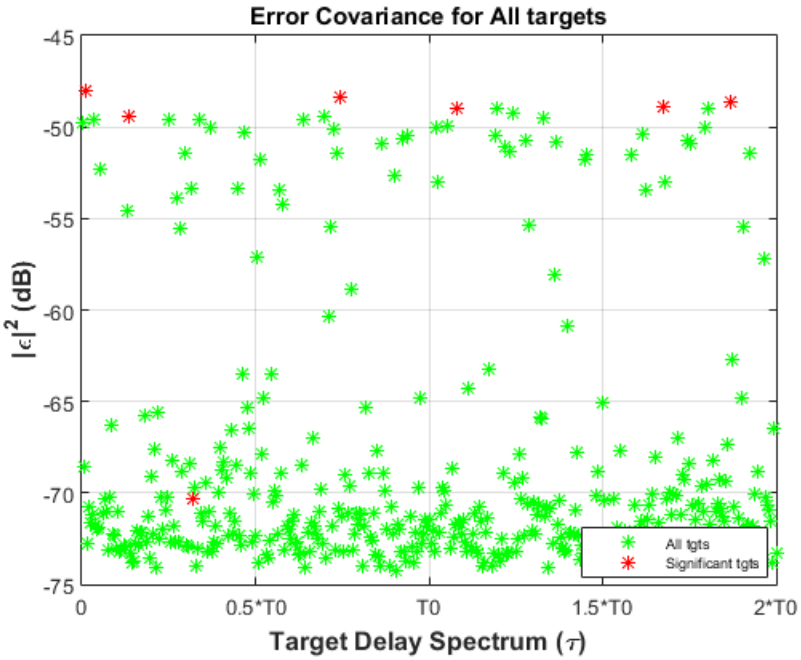

Figure 5.17: Error Covariance for All targets (tgt density of 1.75%)

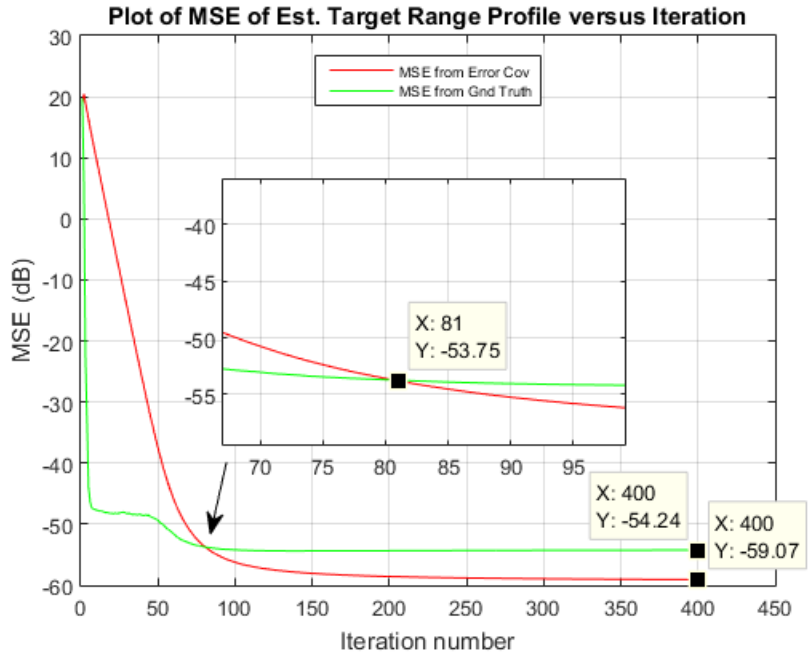

Figure 5.18: Plot of MSE of Est Radar Range Profile versus MMSE Iteration (tgt density of 1.75%)

Now, by examining both Fig. 5.13 and Fig. 5.16, it is seen that although the target density has decreased by almost one-half (3.25%) and one-quarter (1.75%) from the original value of 6.25% in scenario one, the iterative MMSE estimator is still unable to correctly estimate the γ values (red "asterisk" symbol) of the three weakest target scatterer that have erroneous estimated scattering coefficent values in the first scenario when one or more of these three targets are inserted in scenario two and three. Thus, these targets will still end up as missed targets when the estimated $\tilde{\gamma}$ is passed through a CFAR detector. This is also an indication that there is a limitation to the performance of the MMSE estimator when both the spectrum usage is low and the power of the weakest target scatterers are barely above the noise power.

Next, from further examination of the same two figures, it is also observed that there are still some clutter locations that possess estimated γ values (green "asterisk" symbol) above -40 dB when the target density is at 3.25% but the number drops to zero when the target density drops to 1.75% in the radar range profile.

Finally, by examining both Fig. 5.15 and Fig. 5.18, it is observed that the iterative MMSE estimator has again obtained convergence of the results at around iteration number 200 as shown by the red line plot in these figures and thus the same stopping criteria developed for the first scenarios is equally robust to be applied to both the second and third scenarios.

5.2.3.2 Results from Scenario Four - Scenario Six with 50.0% of Spectrum usage

Under this subsection, for scenario four to six of the radar range profile estimation application, the same amount of spectrum usage of 50.0% is applied to three target scenarios as used in the previous subsection. Again, the three plots for the first target scenario of target density of 6.25% present in the radar range profile as shown in Fig. 5.19 - 5.21 will first be examined for its performance.

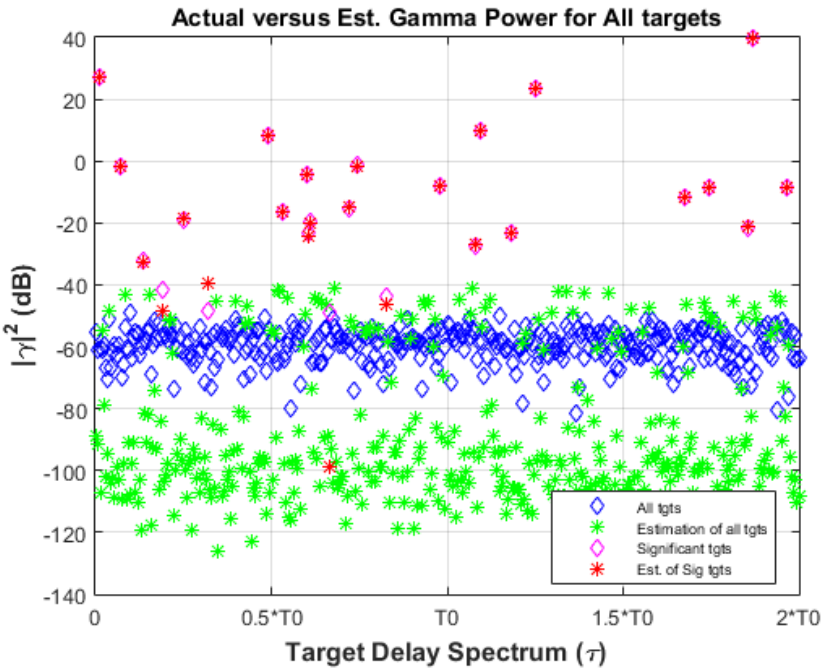

Figure 5.19: Actual versus Est. γ for All targets (tgt density of 6.25%)

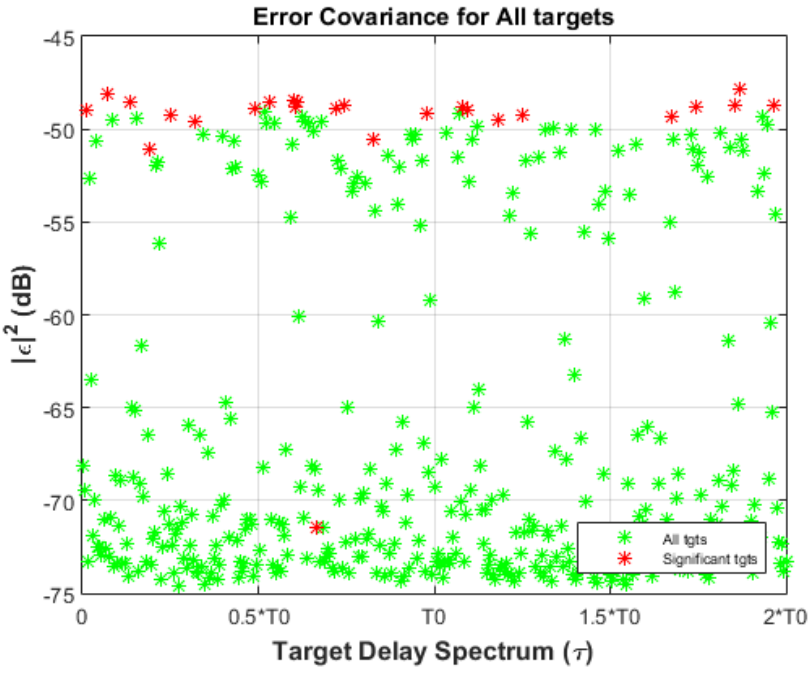

Figure 5.20: Error Covariance for All targets (tgt density of 6.25%)

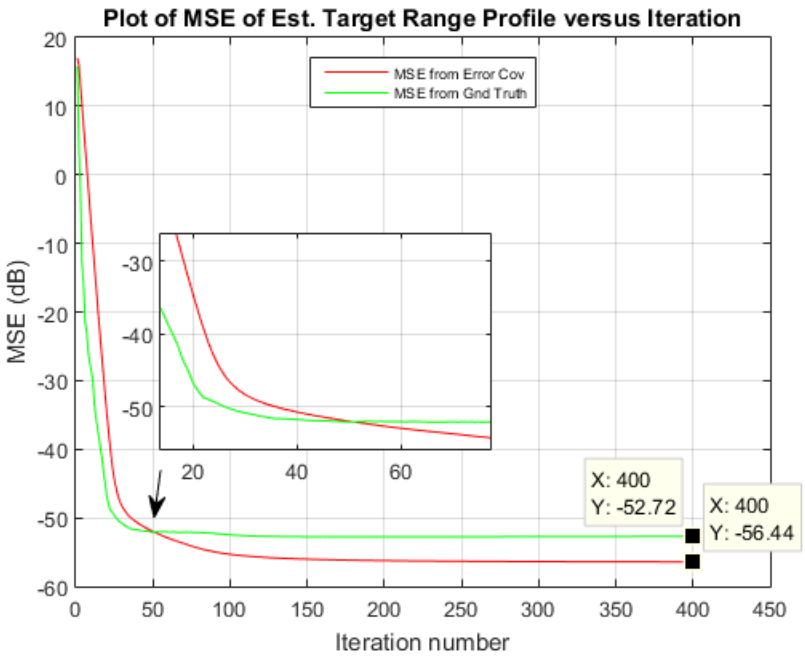

Figure 5.21: Plot of MSE of Est Radar Range Profile versus MMSE Iteration (tgt density of 6.25%)

As a start, by examining Fig. 5.19, it is now observed that out of 25 strong and weak target scatterers indicated by the magneta "diamond" symbol, only the estimated γ value (red "asterisk" symbol) of the weakest target scatterer with power of -48.7 dB is erroneous. This is an improvement of a factor of three from the previous scenario of spectrum usage of 25.0%. Thus, only this weakest target will end up as a missed target when the estimated $\tilde{\gamma}$ is passed through a CFAR detector. Furthermore, there are hardly any clutter locations that possess estimated γ values (green "asterisk" symbol) above -40 dB which indicate that there may be no false alarms after a CFAR detector is applied to the estimated results of the radar range profile.

Next, by examining Fig. 5.20, it is also observed that the iterative MMSE estimator has performed very well in estimating the values of γ for both strong and weak targets (with the exception of the weakest target) such that the final values of the error variance for each of these targets are below -47.0 dB.

Thirdly, by examining Fig. 5.21, it is observed that the iterative MMSE estimator has obtained convergence of the results at around iteration number 140 as shown by the red line plot in the figure. Thus, this is an indication that when the spectrum usage is increased, the convergence rate will also increase linearly as well.

Next, the results obtained from the iterative MMSE estimator when it is applied to the second and third target scenario of low to very low target density within the radar range profiles while still using the same spectrum usage of 50.0% are shown in Fig. 5.22 - 5.27 as follows.

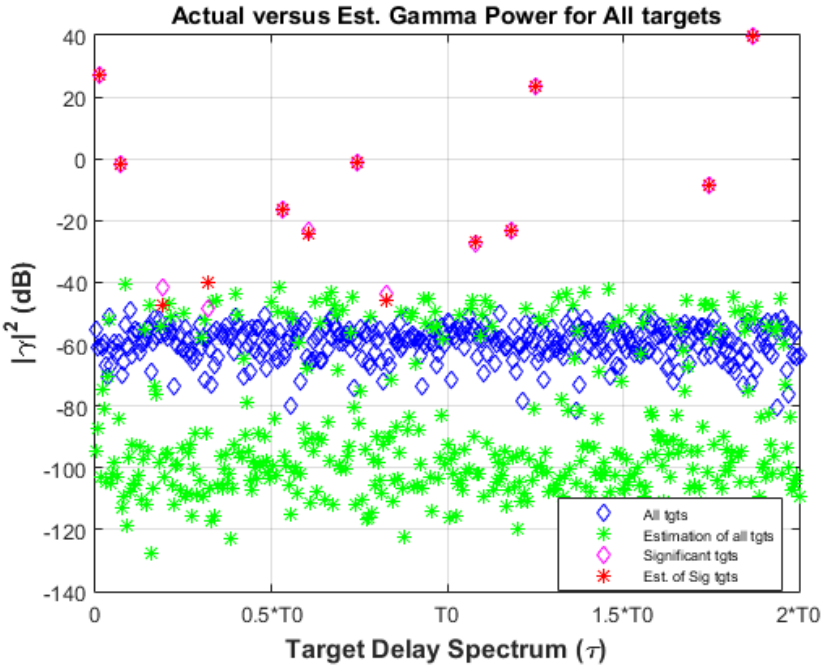

Figure 5.22: Actual versus Est. γ for All targets (tgt density of 3.25%)

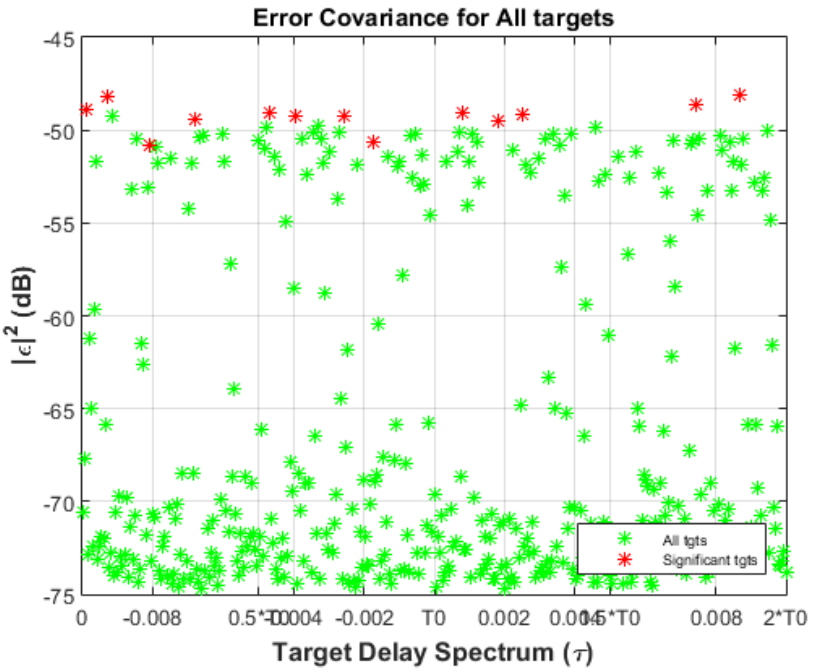

Figure 5.23: Error Covariance for All targets (tgt density of 3.25%)

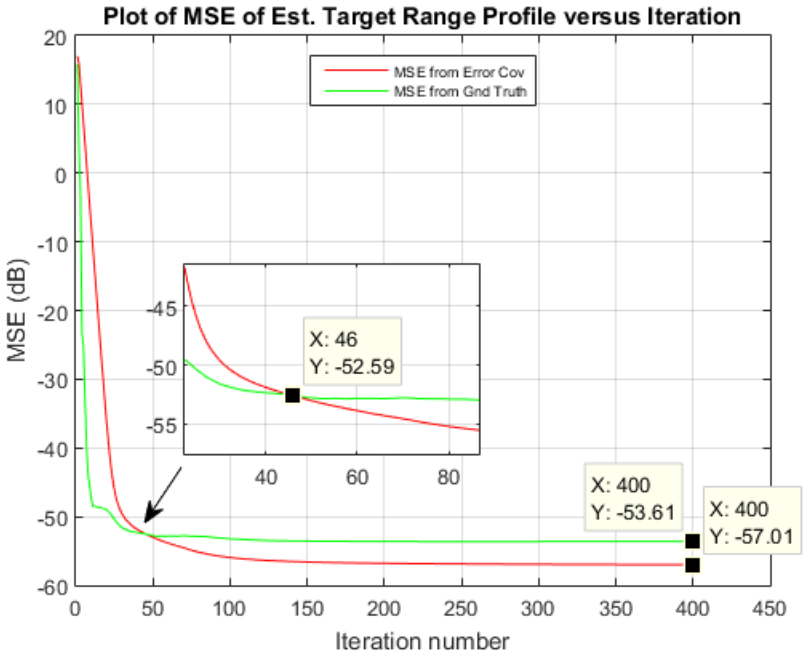

Figure 5.24: Plot of MSE of Est Radar Range Profile versus MMSE Iteration (tgt density of 3.25%)

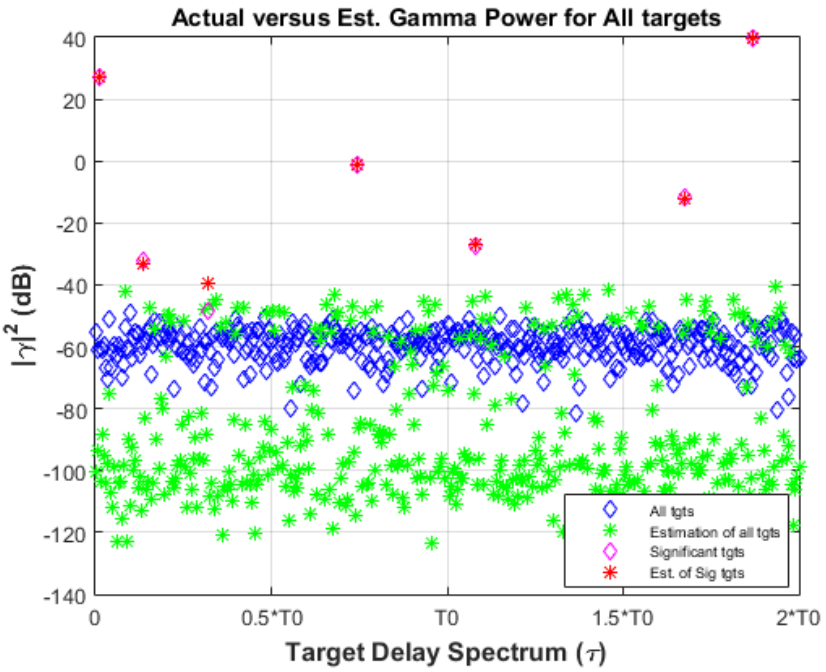

Figure 5.25: Actual versus Est. γ for All targets (tgt density of 1.75%)

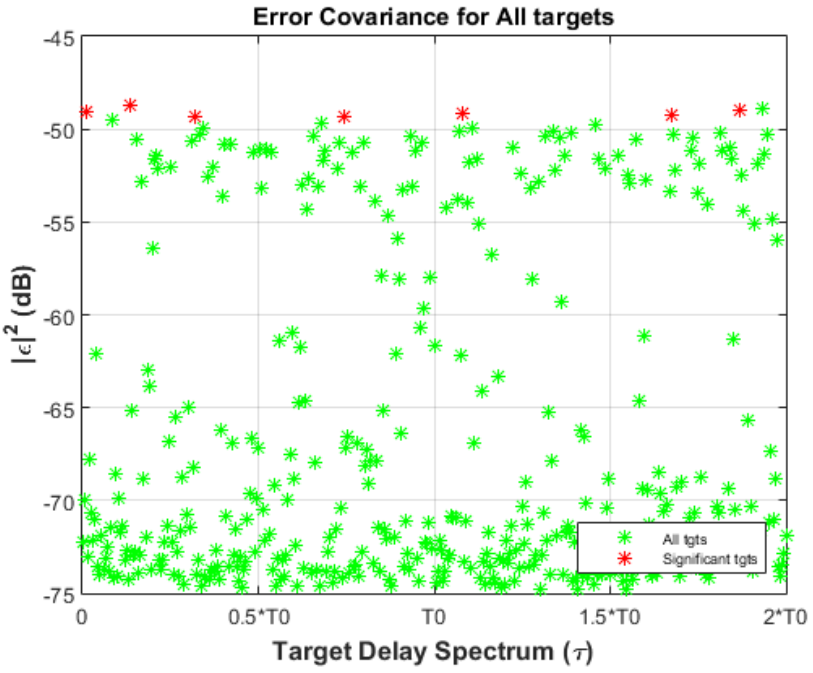

Figure 5.26: Error Covariance for All targets (tgt density of 1.75%)

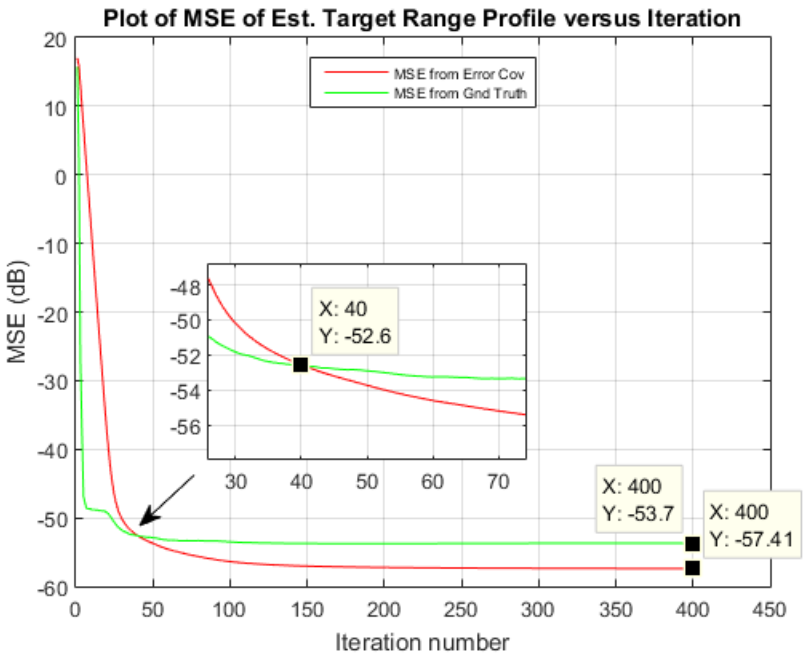

Figure 5.27: Plot of MSE of Est Radar Range Profile versus MMSE Iteration (tgt density of 1.75%)

Now, for the second and third target scenario when the spectrum usage is still 50.0%, it is determined that a reduction of the target density will not help to eradicate the error in estimating the scattering coefficent of the weakest target that has a power of -48.7 dB. As such, this target is not inserted into the second and third target scenarios. Thus, for the results shown in Fig. 5.22 to Fig. 5.27, all targets' scattering coefficents are correctly determined by the MMSE estimator. Again, the inability to resolve the erroneous performance in estimating the γ value of the weakest target shows that that there is a limitation to the performance of the MMSE estimator when both the spectrum usage is not high and the power of the weakest target scatterer is barely above the noise power.

Next, from further examination of Fig. 5.22 and Fig. 5.25, it is also observed that there are no clutter locations that possess estimated γ values (green "asterisk" symbol) above -40 dB when the target density is either at 3.25% or 1.75% of the radar range profile.

Finally, by examining both Fig. 5.24 and Fig. 5.27, it is observed that the iterative MMSE estimator has again obtained convergence of the results at around iteration number 140 as shown by the red line plot in these figures and this again verifies the trend that the convergence rate of the MMSE estimator is linearly dependent on the amount of spectrum usage.

5.2.3.3 Results from Scenario Seven - Scenario Nine with 75.0% of Spectrum usage

Under this subsection, for scenario seven to nine of the radar range profile estimation application, the same amount of spectrum usage of 75.0% is applied to three target scenarios as used in the previous subsection. Again, the three plots for the first target scenario of target density of 6.25% present in the radar range profile as shown in Fig. 5.28 - 5.30 will first be examined for its performance.

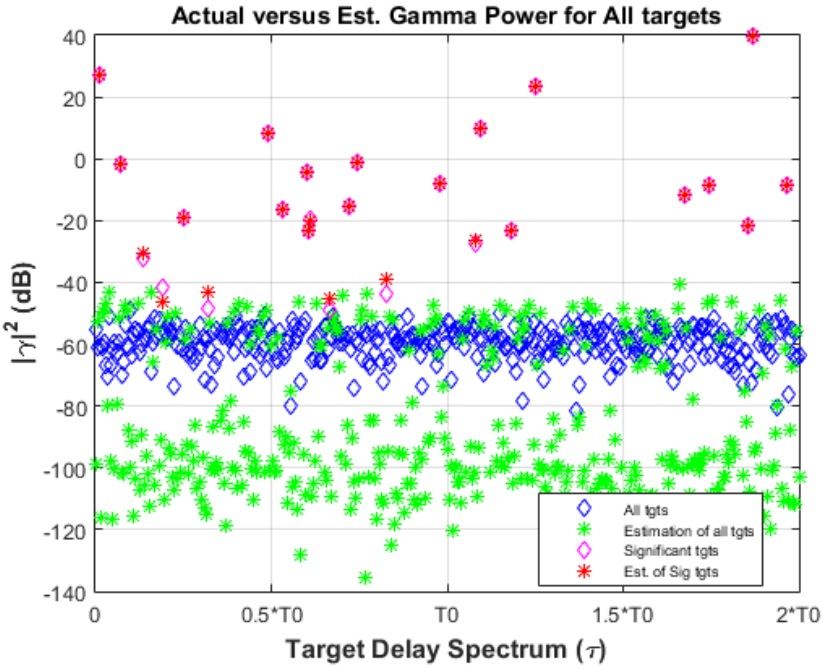

Figure 5.28: Actual versus Est. γ for All targets (tgt density of 6.25%)

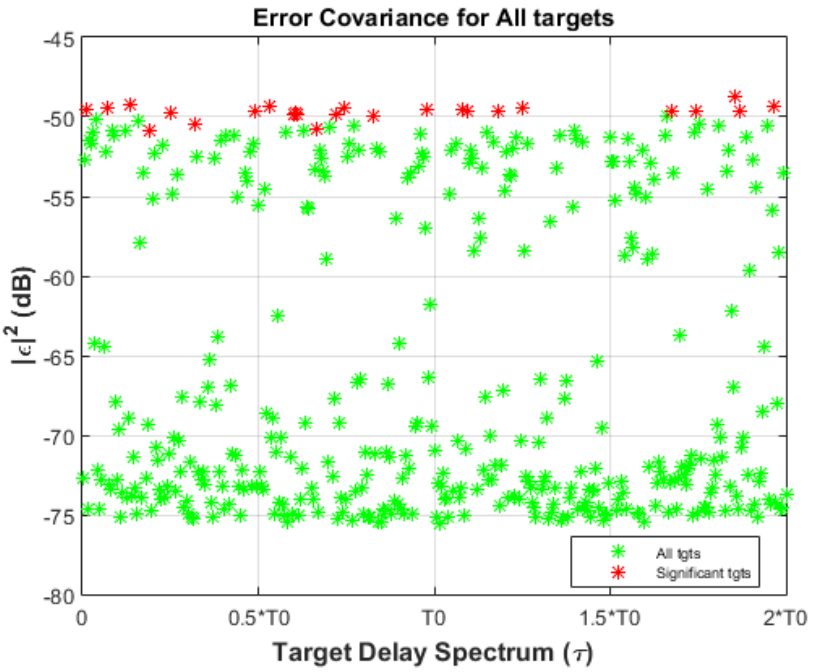

Figure 5.29: Error Covariance for All targets (tgt density of 6.25%)

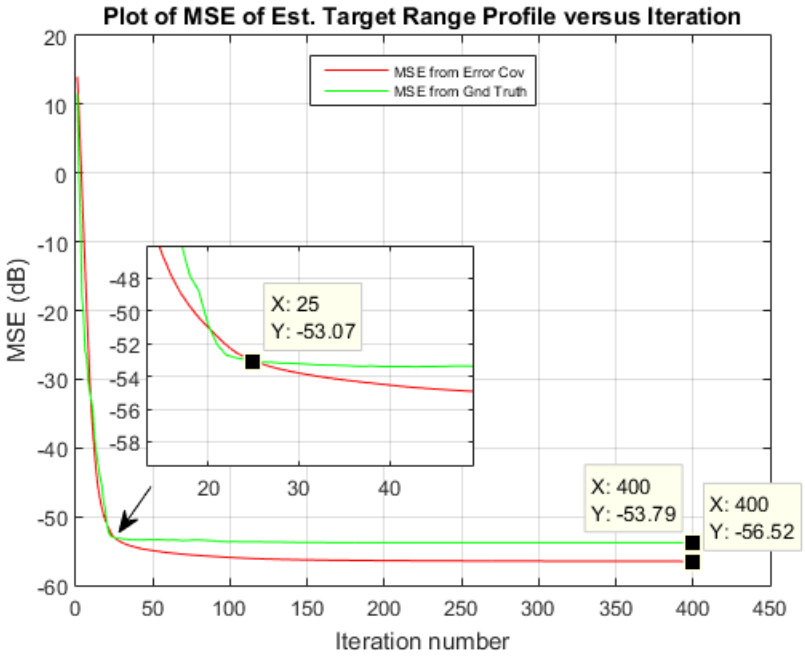

Figure 5.30: Plot of MSE of Est Radar Range Profile versus MMSE Iteration (tgt density of 6.25%)

As a start, by examining Fig. 5.28, it is seen that out of 25 strong and weak target scatterers indicated by the magneta "diamond" symbol, there is no error produce in the estimated $\tilde{\gamma}$ of these 25 targets. This is the best possible scenarios as compared to the previous scenarios of spectrum usage of 25.0% or 50.0%. Thus, there will be no missed target when the estimated $\tilde{\gamma}$ is passed through a CFAR detector. This shows yjay when there is sufficient spectrum usage of the radar application, the limitation to resolve the erroneous performance in estimating the γ value of weak target will be removed. However, there is one clutter location that possess estimated γ values (green "asterisk" symbol) around -40 dB which indicate that this clutter location may generate a false alarm after a CFAR detector is applied to the estimated results of the radar range profile.

Next, by examining Fig. 5.29, it is also observed that the iterative MMSE estimator has performed very well in estimating the values of γ for both strong and weak targets such that the final values of the error variance for each of these targets are around -50.0 dB which is an improvement of -3.00 dB from the previous spectrum usage scenarios.

Thirdly, by examining Fig. 5.30, it is observed that the iterative MMSE estimator has obtained convergence of the results at around iteration number 100 as shown by the red line plot in the figure. Thus, this is a third confirmation of the characteristic of the iterative MMSE estimator such that when the spectrum usage is increased, the convergence rate will also increase linearly as well.

Next, the results obtained from the iterative MMSE estimator when it is applied to the second and third target scenario of low to very low target density within the radar range profiles while still using the same spectrum usage of 75.0% are shown in Fig. 5.31 - 5.36 as follows.

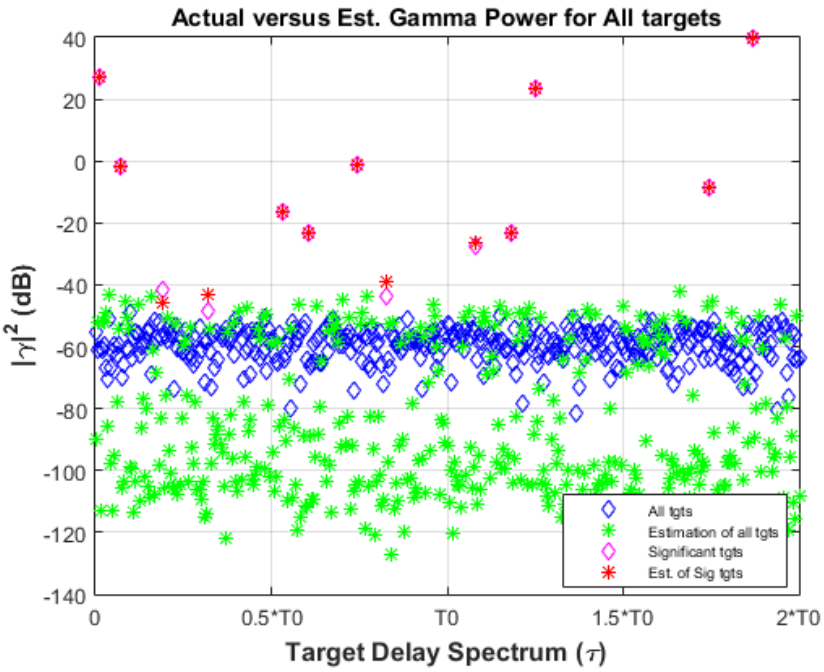

Figure 5.31: Actual versus Est. γ for All targets (tgt density of 3.25%)

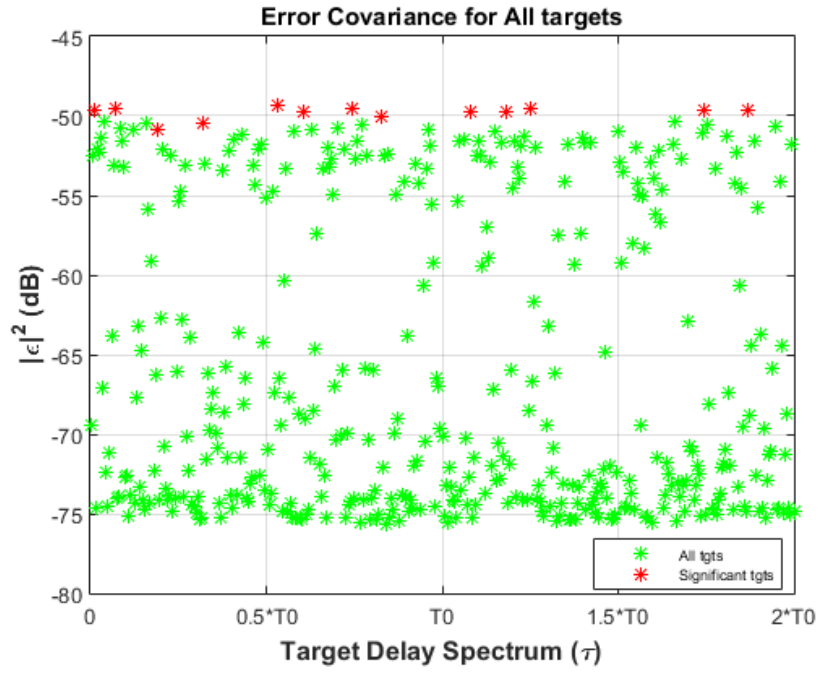

Figure 5.32: Error Covariance for All targets (tgt density of 3.25%)

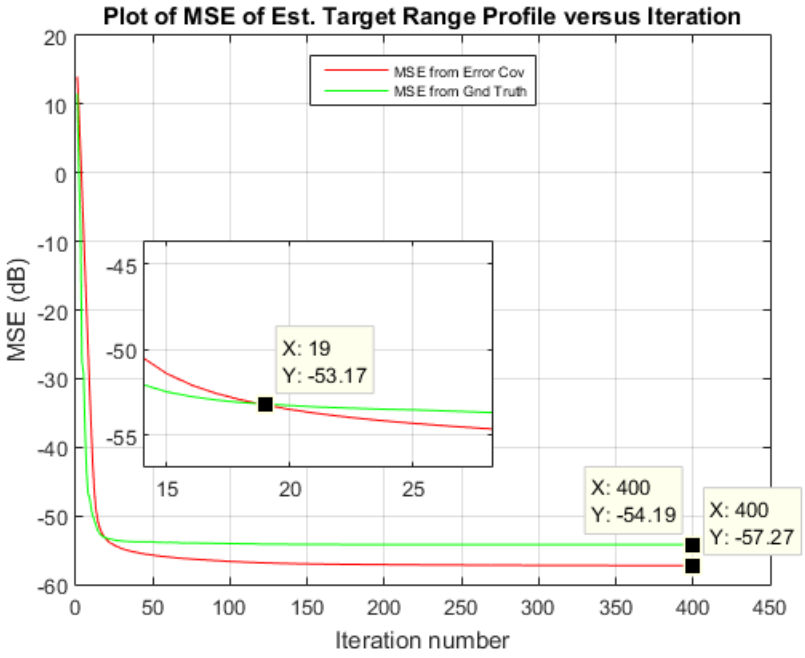

Figure 5.33: Plot of MSE of Est Radar Range Profile versus MMSE Iteration (tgt density of 3.25%)

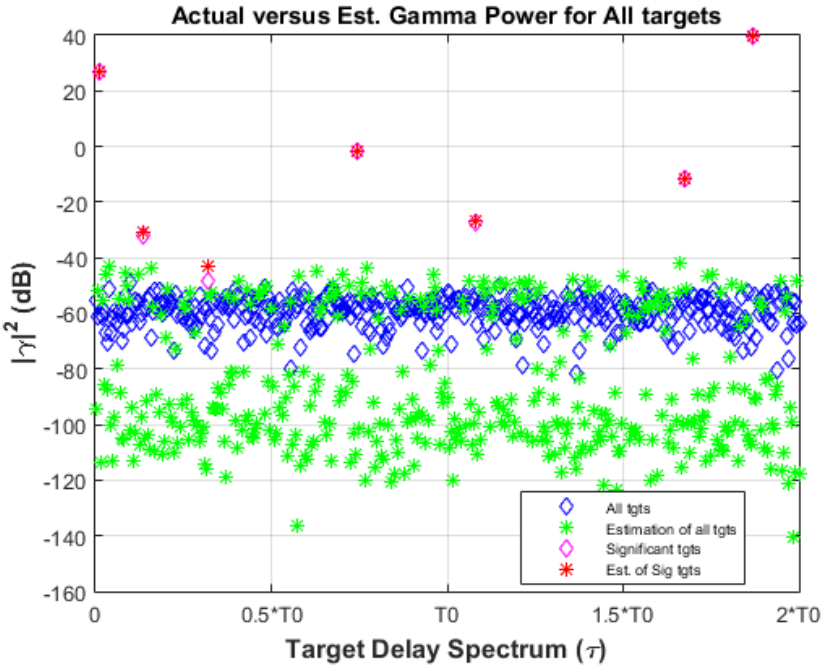

Figure 5.34: Actual versus Est. γ for All targets (tgt density of 1.75%)

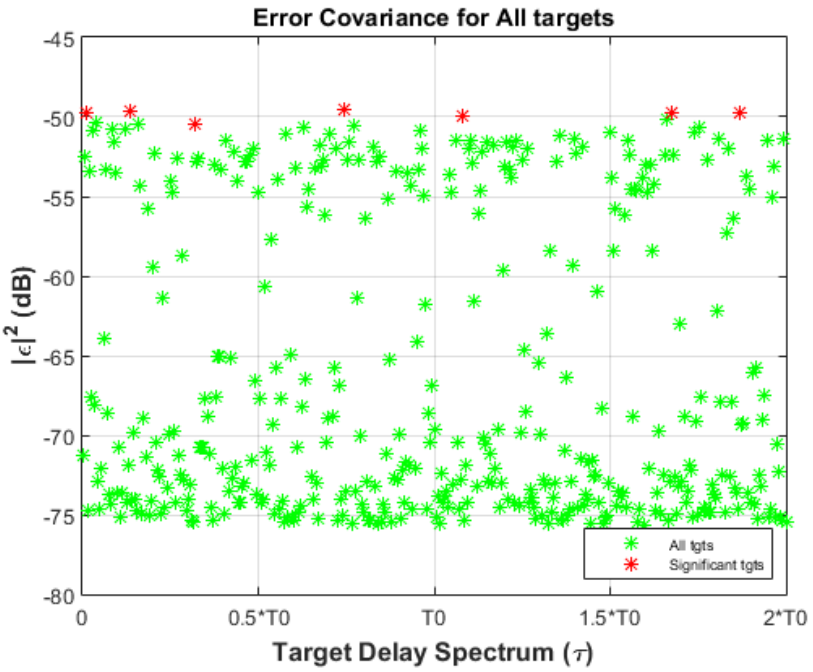

Figure 5.35: Error Covariance for All targets (tgt density of 1.75%)

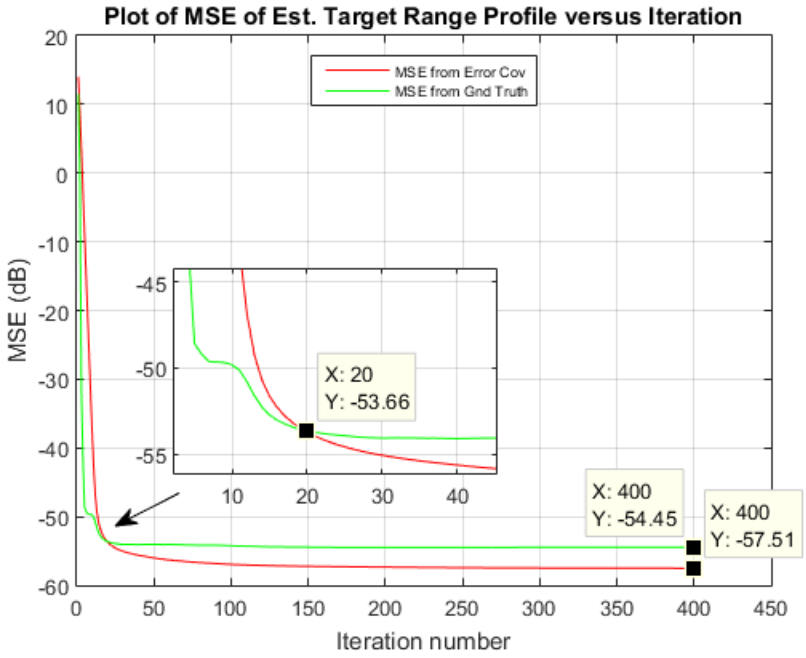

Figure 5.36: Plot of MSE of Est Radar Range Profile versus MMSE Iteration (tgt density of 1.75%)

Now, for the second and third target scenario when the spectrum usage is still 75.0%, from the results shown in Fig. 5.31 and Fig. 5.34, it is seen that all targets' scattering coefficents are correctly determined by the MMSE estimator.

Next, from further examination of Fig. 5.31 and Fig. 5.34, it is also observed that there are no clutter locations that possess estimated γ values (green "asterisk" symbol) above -40 dB when the target density is either at 3.25% or 1.75% of the radar range profile.

Finally, by examining both Fig. 5.33 and Fig. 5.36, it is observed that the iterative MMSE estimator has again obtained convergence of the results at around iteration number 100 as shown by the red line plot in these figures and this again verifies the trend that the convergence rate of the MMSE estimator is linearly dependent on the amount of spectrum usage.

Chapter 6

Conclusion

As this stage, good results have been obtained and demonstrated from both the design and implementation of both Part 1 and 2 of the two-step approach described in this dissertation for mitigating the issues of spectrum congestion and spectrum sharing. In the following sections of this chapter, detailed summaries of the results from these two parts as well as the joint implementation of their results and the performance obtained from the application of the various SSA derived spectrum results on a radar estimation problem will be provided. Finally, a short proposal of the future phases of research work for both parts following the results presented in this dissertation is provided to conclude this Chapter.

6.1 Summary of Sparse Spectrum Allocation Scheme

In the first few sections of Chapter three, a detailed description of the theoretical concept of Marginal Fisher Information (MFI), which forms the basis for developing the Sparse Spectrum Allocation (SSA) algorithm, is provided to allow the readers to understand the mechanism of this algorithm. It is followed by the description of the two perspectives of designing the SSA algorithm which consists of the Sparse Array Design Perspective and the Array Thinning Design Perspective. Following that, under each perspective, various implementations/adaptations of the SSA algorithm corresponding to spectrum usage from the selection of 25.0%, 50.0%, 60.0% and 85.0% are pro-

vided along with the simulation results obtained from each of these adaptations.

From the results obtained under these various adaptations when using the first perspective of Sparse Array Design, it can be seen that that the SSA algorithm is able to generate sparse frequency arrays whose coarray structures resembles that of a Low Redundancy Linear Array (LRLA) which is an indication of low redundancies of frequency measurements within each sparse frequency array. At the same time, many of these sparse frequency arrays do nor suffer from any 3-dB range resolution degradation or only minimal degradation when correspond to the spectrum that is utilized. Thus, this achieves the objective of Part 1 of the two-step approach for addressing the issues of Spectrum Congestion and Spectrum Sharing.

Likewise, from the results obtained under these various adaptations when using the second perspective of Array Thinning Design, it is still observed that that the SSA algorithm is able to generate sparse frequency arrays whose coarray structures bear more resemblances to a LRLA as compared to an uniformly-spaced frequency array. However, due to the conscious effects of ensuring that the minimum inserted gap size is at least equal to 2.50% of the full spectrum, this approach will more likely result in some degradation of the 3-dB range resolution (can be as big as a factor of 1.40) as compared to the approach based on the first perspective.

6.2 Summary of Higher-order PCFM waveforms

In the first few sections of Chapter four, the theoretical concept for extending the PCFM framework of designing radar waveforms based on "first-order" hold to higher-order hold representations are discussed in great details. Susbequently, the discussion delves into the insights about the relationships between these various order representations as well as the limits of the code values within each order representation. The framework for multi-order PCFM waveform implementation is then introduced along with the steps of the optimization process of both single order and mixed-order PCFM waveforms.

From the simulation results obtained from these higher order representations of PCFM waveforms when they are generated via the mixed-order representation, it is shown that it is possible to obtain good improvement in terms of sidelobe performance while maintaining good spectral containment as compared to when the PCFM waveform is generated from a single order representation. In addition, the introduction of mixed-order representation also provides the option of either performing sequential optimization on these representations on an order by order rbasis or the joint optimization of these representations depending on the computational resources of the machine that is used to perform the optimization.

6.3 Summary of combination of both parts for Spectrally-Cooperative Radar implementation

In this Chapter, the results obtained from the SSA algorithm that is based on the first perspective are being used to demonstrate the viability of generating PCFM waveforms based on the spectrum usage derived from the SSA algorithm. By using several example spectrum usage scenarios from the SSA algorithm, the resultant spectrum and matched filter response obtained from the composite PCFM waveform formed from the summation of several PCFM waveforms corresponding to the number of disjointed spectrum segments within the SSA algorithm are then plotted for discussions.

From the plots obtained for the resultant spectrum usage and matched filter response, they indicate the practicality of creating physical realizable waveforms based on the results from the SSA algorithm. As such, this Chapter bridges the transition from Part 1 to Part 2 of the two-step approach that is presented in this dissertation.

6.4 Summary of Radar Range Profile Estimation Application

In this Chapter, the results obtained from the SSA algorithm are applied to the Radar Range Profile Estimation application. For this investigation, several different scenarios of spectrum usage as well as target density within the radar range profiles consisting of both strong and weak targets are explored in order to demonstrate the viability of using the SSA results in such an application. In total, nine different scenarios are explored for the radar range profile estimation. In addition, an iterative MMSE estimator is also introduced in this Chapter for performing the estimation of the radar range profile.

From the results obtained from all nine scenarios, it is shown that when the magnitude of the targets' scattering coefficient is higher than the noise power or clutter power, it is possible to use as little as 25.0% of the full spectrum to obtain a very accurate estimation of the radar range profile without suffering from missed detections or false alarms. However, for any target whose magnitude is at the level of the noise power or clutter power, more spectrum usage is required to avoid the performance degradation of missed detections and higher false alarms.

6.5 Future extensions of this research

For the next phase of the research that are reported in this dissertation, the discussian will first focus on Part 1 of the two-step approach described in the dissertation. As a start, the next step will be to apply the SSA algorithm to the specifications of spectrum usage and Pulse Repetition Frequency of a real-life example of a radar system so as to derive a sparse spectrum usage solution for this system to operate in a co-sharing mode with other RF systems. Subsequently, the results obtained from the SSA algorithm can then be used to determine the feasibility of applying these results to the radar system under study taking into account the 3-dB range resolution and sidelobe degradation performance.

Next, with regards to Part 2 of the two-step approach, the next step that comes to mind will be to

construct the optimized second-order and mixed-order PCFM radar waveforms using an Arbitrary Waveform Generator (AWG) as well as selecting a suitable transmit frequency and bandwidth and then performs a transmit-receive operation of this waveform via loopback mechanism in the lab so as to examine the characteristics of the received signal return from these higher-order PCFM waveforms via spectrum analyzer etc.

Once the indoor loop-back test and evaluation has been completed, the second step will then be to perform an outdoor transmit-receive exercise of the higher-order PCFM waveforms so as to obtain the matched filter response of these higher-order PCFM waveforms to real objects and clutter that are readily available outdoors.

Finally, the third step will then be to repeat both steps of constructing the PCFM waveform by using the disjointed spectrum segments that are described in Chapter five so as to examine the matched filter response of the composite PCFM waveform in the presence of real objects and clutter.

Bibliography

[1] M.R. bell, N. Devroye, D. Erricolo, T. Koduri, S. Rao and D. Tuninetti, "Results on spectrum sharing between a radar and a communications system," *International Conference on Electronic Advanced Application*, pp. 826-829, Aug 2014.

[2] H. Wang, J. Johnson, C. Baker, L. Ye and C. Zhang "On spectrum sharing between communications and air traffic control radar systems," *IEEE Radar Conference*, pp. 1545-1550, May 2015.

[3] J. de Graff, H. Faust, J. Alatishe, and S. Talapatra, "Generation of spectrally confined transmitted radar waveforms: experimental results," *IEEE Radar Conference*, pp. 76-83, May 2006.

[4] S. Blunt, M. Cook, J. Jakabosky, E. Perrins and J. de Graaf, "Polyphase-coded FM (PCFM) waveforms, part I: implementation," *IEEE Transactions on Aerospace and Electronic Systems*, vol. 50, no. 3, pp. 2218-2229, July 2014.

[5] H. T. Hayvaci and B. Tavli, "Spectrum Sharing in Radar and Wireless Communication Systems: A Review," *International Conference on Electromagnetics in Advanced Applications*, pp. 810-813, Aug. 2014.

[6] M.A. Richards, J.A. Scheer and W.A. Holm, *Principles of Modern Radar: Basic Principles*, SciTech Publishing, 2014.

[7] A. L. Maffett, "Array Factors with Nonuniform Spacing Parameter," *IRE Transactions on Antennas and Propagation*, vol. 10, no. 2, pp. 131-136, 1962.

[8] S. M. Kay, *Fundamentals of Statistical Signal Processing: Estimation Theory*, 1st ed., vol. 1, Prentice Hall, New Jersey, 1993, ch. 3-4.

[9] J. B. Anderson, T. Aulin and C.-E. Sundberg, *Digital Phase Modulation*, Plenum Press, New York, NY, 1986, ch 11.

[10] S. Blunt, M. Cook, E. Perrins and J. de Graaf, "CPM-based radar waveforms for efficiently bandlimiting a transmitted spectrum," *IEEE Radar Conference*, pp. 1-6, May 2009.

[11] J. Jakabosky, P. Anglin, M. Cook, S.D. Blunt, and J. Stiles, "Non-Linear FM Waveform Design using Marginal Fisher's Information within the CPM Framework," *IEEE Radar Conference*, Kansas City, MO, 23-27 May 2011

[12] P.S. Tan, J. Jakabosky, J. M. Stiles, and S.D. Blunt, "On higher-order representations of polyphase-coded FM radar waveforms," *IEEE International Radar Conference*, pp. 467-472, May 2015.

[13] A. W. Doerry, "Generating nonlinear FM chirp waveforms for radar," *Sandia Report*, SAND2006-5856, Sept. 2006.

[14] A.W. Doerry, 'Generating precision nonlinear FM chirp waveforms," *SPIE Conference on Defense, Security and Sensing*, vol. 6547, pp. 1-12, April 2007.

[15] S.D. Blunt, J. Jakabosky, M. Cook, J. Stiles, S. Seguin, and E.L. Mokole, "Polyphase-coded FM (PCFM) waveforms, part II: optimization," *IEEE Transactions on Aerospace and Electronic Systems*, vol. 50, no. 3, pp. 2230-2241, July 2014.

[16] R. Saruthirathanaworakun, J. Peha and L. Correia, "Opportunistic sharing between rotating radar and cellular," *IEEE Journal on Selected Areas in Communications*, vol. 30, no. 10, pp. 1900-1910, Nov. 2012.

[17] Y. Nijsure, Y. Chen, C. Yuen and Y. H. Chew, "Location-aware spectrum and power allocation in joint cognitive communication-radar networks," *Sixth International ICST Conference on Cognitive Radio Oriented Wireless Networks and Communications*, pp. 171-175, June 2011.

[18] S. Sen, G. Tang and . Nehorai, "Multiobjective Optimization of OFDM Radar Waveform for Target Detection," *IEEE Transactions on Signal Processing*, vol. 59, no. 2, pp. 639-652, Feb. 2011.

[19] S. Amuru, R. M. Buehrere, R. Tandon and S. Sodagari, "MIMO Radar Waveform Design to support Spectrum Sharing," *IEEE Military Communications Conference*, pp. 1535-1540, Sept. 2013.

[20] A. Aubry, A. DE MAIO, Y. Huang, M. Piezzo and A. Farina, "A New Radar Waveform Design Algorithm With Improved Feasibility for Spectral Coexistence," *IEEE Transactions on Aerospace and Electronic Systems*, vol. 51, no. 2, pp. 1030-1038, April 2015.

[21] K.W. Huang, M. Bica, U. Mitra and V. Kovivunen, "Radar Waveform Design in Spectrum Sharing Environment: Coexistence and Cognition," *IEEE Radar Conference*, pp. 1698-1703, May 2015.

[22] F. Hessar and S. Roy, "Spectrum Sharing Between a Surveillance Radar and Secondary Wi-Fi Networks," *IEEE Transactions on Aerospace and Electronic Systems*, vol. 52, no. 3, pp. 1434-1448, June 2016.

[23] I.W. Selesnick, S.U. Pillai and R. Zheng "An Iterative Algorithm for the Construction of Notched Chirp Signals," *IEEE Radar Conference*, pp. 200-203, May 2010.

[24] K. Gerlach, M.R. Frey, M.J. Steiner and A. Shackelford, "Spectral Nulling on Transmit via Nonlinear FM Radar Waveforms," *IEEE Transactions on Aerospace and Electronic Systems*, vol. 47, no. 2, pp. 1507-1515, April 2011.

[25] W. Liu, Y. Lu, and M. Lesturgie, “Optimal sparse waveform design for HFSWR system,” *International Waveform Diversity and Design Conference*, pp. 127-130, June 2007.

[26] M. R. Cook, T. Higgins, and A. K. Shackelford, “Thinned spectrum radar waveforms,” *International Waveform Diversity and Design Conference*, pp. 238-243, Aug 2010.

[27] I.W. Selesnick and S.U. Pillai, “Chirp-Like Transmit Waveforms with Multiple Frequency-Notches,” *IEEE Radar Conference*, pp. 1106-1110, May 2011.

[28] J. Jakabosky, S.D. Blunt, and B. Himed, "Waveform Design and Receive Processing for Nonrecurrent Nonlinear FMCW Radar," IEEE Intl. Radar Conf., Washington, DC, 11-15 May 2015.

[29] J. Jakabosky, S.D. Blunt, and A. Martone, "Incorporating Hopped Spectral Gaps into Non-recurrent Nonlinear FMCW Radar Emissions," *IEEE Intl. Workshop on Computational Advances in Multi-Sensor Adaptive Processing*, Cancun, Mexico, 13-16 Dec. 2015

[30] J. Jakabosky, B. Ravenscroft, S.D. Blunt and A. Martone, “Gapped Spectrum Shaping for Tandem-Hopped Radar/Communications & Cognitive Sensing,” *IEEE Radar Conference*, pp. 1-6, May 2016.

[31] C. Shahriar, A. Abdelhadi and T.C. Clancy, “Overlapped-MIMO Radar Waveform Design for Coexistence With Communication Systems,” *IEEE International Communications and Networking Conference*, pp. 223-228, April 2015.

[32] E.H.G. Yousif, M.C. Filippou, F. Khan, T. Ratnarajah and M. Sellathurai, ‘A New LSA-based Approach for Spectral Coexistence of MIMO Radar and Wireless Communications Systems,” *IEEE International Conference on Communications*, pp. 1-6, 2016.

[33] B. Li, H. Kumar and A. Petropulu, “A Joint Design Approach for Spectrum Sharing Between Radar and Communication Systems,” *IEEE International Conference on Acoustic, Speech and Signal Processing*, pp. 3306-3310, 2016

[34] S. Gogineni, M. Rangaswamy and A. Nehorai, "Multi-modal OFDM waveform design," *IEEE Radar Conference*, pp. 1-5, April 2013.

[35] L. Han and K. Wu, "Joint wireless communication and radar sensing systems - state of the art and future prospects," *IET on Microwaves, Antennas & Propagation*, vol. 7, no. 11, pp. 876-885, May 2013.

[36] B. Li and A. Petropulu, "Spectrum Sharing between Matrix Completeion Based MIMO Radars and a MIMO Communication System," *International Conference on Acoustic, Speech and Signal Processing*, pp. 2444-2448, 2015.

[37] O. Bar-Ilan and Y.C. Eldar, 'Sub-Nyquist Radar," *International ITG Conference on Systems, Communications and Coding*, pp. 1-6, Jan 2013.

[38] H. Stahl, J Mietzner and R. F.H. Fischer, "A Sub-Nyquist Radar System Based on Optimized Sensing Matrices Derived via Sparse Rulers," *International Workshop on Compressive Sensing Theory and its Applications to Radar, Sonar and Remote Sensing*, pp. 36-40, June 2015.

[39] M. J. Lindenfeld, "Sparse Frequency Transmit and Receive Waveform Design," *IEEE Transactions on Aerospace and Electronic Systems*, vol. 40, no. 3, pp. 851-861, July 2004.

[40] G. Wang and Y. Lu, "Designing Sparse Frequency Waveform Using Iterative Algorithm," *11th International Radar Symposium*, pp. 1-4, 2010.

[41] G. Wang and Y. Lu, "Designing single/multiple sparse frequency waveforms with sidelobe constraint," *IET on Radar, Sonar Navigation*, vol. 5, no. 1, pp. 32-38, 2011.

[42] S. Frost and B. Rigling, "Performance comparisoin for constrained radar waveform design," *IEEE Radar Conference*, pp. 724-728, May 2011.

[43] L. K. Patton, C. A. Bryant and B. Himed, "Radar-Centric Design of Waveforms with Disjoint Spectral Support," *IEEE Radar Conference*, pp. 269-274, 2012.

[44] A. Aubry, A. De Maio, M. Piezzo and A. Farina, "Radar waveform design in a spectrally crowded environment via nonconvex quadratic optimization," *IEEE Transactions on Aerospace and Electronic Systems*, vol. 50, no. 2, pp. 1138-1152, April 2014.

[45] W. Rowe, P. Stoica and J. Li, "Spectrally Constrained Waveform Design [sp Tips&Tricks]," *IEEE Signal Processing Magazine*, vol. 31, no. 2, pp. 157-162, May 2014.

[46] J. Leech, "On the representation of 1,2,...n by differences," *Journal of London Mathematical Society*, vol.31, pp. 160-169, 1956.

[47] A. T. Moffet, "Minimum-Redundancy Linear Arrays," *IEEE Transactions on Antennas and Propagation*, vol. 16, no. 2, pp. 172-175, 1968.

[48] M. Ishiguro, "Minimum redundancy linear arrays for a large number of antennas," *Radio Science*, vol. 15, no. 6, pp. 1163-1170, 1980.

[49] E. Vertatschitsch and S. Haykin, "Nonredundant Arrays," *IEEE Proceedings*, vol. 74, no. 1, pp. 217, Jan. 1986.

[50] K. A. Blanton and J. H. McClellan, "New Search Algorithm for Minimum Redundancy Linear Arrays," *International Conference on Acoustic, Speech and Signal Processing*, pp. 1361-1364, 1991.

[51] D.A. Linebarger, I.H. Sudborough and I.G. Tollis, "Difference bases and sparse sensor arrays," *IEEE Transactions on Information Theory*, vol. 39, no. 2, pp. 716-721, Mar. 1993.

[52] M. J. Rossouw, J. Joubert and D. A. McNamara,"Thinned arrays using a modified minimum redundancy synthesis technique," *Electronics Letters*, vol. 33, no. 10, pp. 826-827, May 1997.

[53] A. Camps, A. Cardama and D. Infantes, "Synthesis of Large Low-Redundancy Linear Arrays," *IEEE Transactions on Antennas and Propagation*, vol. 49, no. 12, pp. 1881-1883, Dec. 2002.

[54] V. Murino, A. Trucco and C.S. Regazzoni, "Synthesis of unequally spaced arrays by simulated annealing," *IEEE Transactions on Signal Processing*, vol. 44, no. 1, pp. 119-122, 1996.

[55] A. Rezavi and K. Forooraghi, "Thinned arrays using pattern search algorithms," *Progress in Electromagnetic Research*, vol. 78, pp. 61-71, 2008.

[56] M. Donelli, A. Martini, and A. Massa, "Square array based on Hadamard difference sets," *IEEE Transactions on Antennas and Propagation*, vol. 57, no. 8, pp. 2491-2495, Aug. 2009.

[57] J. Corcoles and M. A. Gonzalez, "Efficient combined array thinning and weighting for pattern synthesis with a nested optimization scheme," *IEEE Transactions on Antennas and Propagation*, vol. 60, no. 11, pp. 5107-5117, Nov. 2012.

[58] J. Stiles and J. Jenshak, "Sparse Array Construction using Marginal Fisher's Information," *IEEE Waveform Diversity and Design Conference*, pp. 202-207, Feb. 2009.

[59] H. Griffiths, L. Cohen, S. Watts, E. Mokole, C. Baker, M. Wicks, and S. Blunt, "Radar spectrum engineering and management: technical and regulatory issue," *Proceedings of IEEE*, vol. 103, no. 1, pp. 85-102, Jan 2015.

[60] H. Griffiths, S. Blunt, L. Cohen, and L. Savy, "Challenge problems in spectrum engineering and waveform diversity," *IEEE Radar Conference*, pp. 1-5, May 2013.

[61] M. Wicks, E. Mokole, S.D. Blunt, V. Amuso, and R. Schneible, *Principles of Waveform Diversity & Design*, SciTech Publishing, 2010.

[62] S. Pillai, K.Y. Li, I. Selesnick, and B. Himed, *Waveform Diversity: Theory and Applications*, McGraw-Hill, 2011.

[63] F. Gini, A. De Maio, and L.K. Patton, *Waveform Design & Diversity for Advanced Radar Systems*, IET, 2012.

[64] N. Levanon and E. Mozeson, *Radar Signals*, Wiley-IEEE Press, 2004.

[65] J.R. Klauder, A.C. Price, S. Darlington, W.J. Albersheim, "The theory and design of chirp radars," *The Bell System Technical Journal*, vol. XXXIX, no. 4, pp. 745-808, July 1960.

[66] E. Fowle, "The design of FM pulse compression signals," *IEEE Transactions on Information Theory*, vol. 10, no. 1, pp. 61-67, Jan 1964.

[67] C.E. Cook, "A class of nonlinear FM pulse compression signals," *Proceedings of IEEE*, vol. 52, no. 11, pp. 1369-1371, Nov 1964.

[68] J.A. Johnston and A.C. Fairhead, "Waveform design and Doppler sensitivity analysis for non-linear FM chirp pulses," *IEEE Proceedings for Communications, Radar & Signal Processing*, vol. 1333, no. 2, pp. 163-175 , April 1986.

[69] T. Collins and P. Atkins, "Nonlinear frequency modulation chirps for active sonar," *IEEE Proceedings on Radar, Sonar & Navigation*, vol. 146, no. 6, pp. 312-316, Dec. 1999.

[70] M. Labitt, "Obtaining low sidelobes using non-linear FM pulse compression," *MIT Lincoln Lab Project report*, ATC-223, Nov 1994.

[71] I. Gladkova, "Design of frequency modulated waveforms via the Zak transform," *IEEE Transactions on Aerospace and Electronic Systems*, vol. 40, no. 1, pp. 355-359, Jan 2004.

[72] E. De Witte and H. D. Griffiths, "Improved ultra-low range sidelobe pulse compression waveform design," *Electronics Letters*, vol. 40, no. 22, pp. 1448-1450, Oct. 2004.

[73] J. Kurdzo, B.L. Cheong, R. Palmer, and G. Zhang, "Optimized NLFM pulse compression waveforms for high-sensitivity radar observation," *International Radar Conference*, pp. 1-6, Oct 2014.

[74] S.D. Blunt and E.L. Mokole, "An overview of radar waveform diversity," *IEEE Aerospace and Electronic Systems Magazine*, vol. 31, no. 11, pp. 2-42, Nov. 2016.

[75] W.J. Caputi, "Stretch: a time-transformation technique," *IEEE Transactions on Aerospace and Electronic Systems*, vol. 7, no. 2, pp. 269-278, mar 1971.

[76] R.L. Frank, “Polyphase codes with good non-periodic correlation properties,” *IEEE Transactions on Information Theory*, vol. 9, no. 1, pp. 43-45, Jan 1963.

[77] B.L. Lewis and F.F. Kretschmer, “A new class of polyphase pulse compression codes and techniques, ” *IEEE Transactions on Aerospace and Electronic Systems*, vol. 17, no. 3, pp. 364-372, May 1981.

[78] M.N. Cohen, M.N., M.R. Fox, J.M. Baden, “Minimum peak sidelobe pulse compression codes, ” *IEEE International Radar Conference*, Arlington, V.A., May 1990.

[79] C.J. Nunn and G.E. Coxson, ‘Polyphase pulse compression codes with optimal peak and integrated sidelobes, ” *IEEE Transactions on Aerospace and Electronic Systems*, vol. 45, no. 2, pp. 775-781, April 2009.

[80] J. Jakabosky, S.D. Blunt, M.R. Cook, J. Stiles, and S.A. Seguin, “Transmitter-in-the-Loop Optimization of Physical Radar Emissions,” *IEEE Radar Conference*, Atlanta, GA, 7-11 May 2012

[81] L. Ryan, J. Jakabosky, S.D. Blunt, C. Allen and L. Cohen, “Optimizing polyphase-coded FM waveforms within a LINC transmit architecture,” *IEEE Radar Conference*, Cincinnati, OH, 19-23 May 2014.

[82] S.D. Blunt, P. McCormick, T. Higgins, and M. Rangaswamy, "Spatially-Modulated Radar Waveforms Inspired by Fixational Eye Movement," *IEEE Radar Conference*, Cincinnati, OH, 19-23 May 2014

[83] P. McCormick and S.D. Blunt, "Fast-Time 2-D Spatial Modulation of Physical Radar Emissions," *Intl. Radar Symp*, Dresden, Germany, 24-26 June 2015

[84] S.D. Blunt, P. McCormick, T. Higgins and M. Rangaswamy, “Physical emission of spatially-modulated radar,” *IET Radar, Sonar & Navigation*, vol. 8, no. 12, pp. 1234-1246, Dec. 2014.

[85] P. McCormick, J. Jakabosky, S.D. Blunt, C. Allen and B. Himed, 'Joint polarization/waveform design and adaptive receive processing, " *IEEE International Radar Conference*, DC, May 2015.

[86] J. Jakabosky, P. McCormick and S.D. Blunt, "Implementation & design of physical radar waveform diversity," *IEEE Aerospace and Electronic Systems Magazine*, vol. 31, no. 12, pp. 26-33, Dec. 2016.

[87] C. Sahin, J. Jakabosky, P. McCormick, J. Metcalf and S.D. Blunt, "A novel approach for embedding communication symbols into physical radar waveforms, " *IEEE Radar Conference*, Seattle, WA, May 2017.

[88] P. McCormick and S.D. Blunt, "Nonlinear conjugate gradient optimization of polyphase-coded FM radar waveforms, " *IEEE Radar Conference*, Seattle, WA, May 2017.

[89] J. Jakabosky, S.D. Blunt, and Braham Himed, "Optimization of 'over-coded' radar waveform," *IEEE Radar Conference*, pp. 19-23, May 2014.

[90] L. Jackson, S. Kay and N. Vankayalapati, "Iterative method for nonlinear FM synthesis of radar signals," *IEEE Transactions on Aerospace and Electronic Systems*, vol. 46, no. 2, pp. 910-917, April 2010.

[91] S. Boukeffa, Y. Jiang and T. Jiang, "Sidelobes reduction with nonlinear frequency modulated waveforms," *IEEE 7th International Colloquium on Signal Processing and its Applications*, Mar 2011.

[92] I.C. Vizitiu, "Sidelobe reduction in the pulse-compression radar using synthesis of NLFM laws," *Hindawi International Journal of Antennas and Propagation*, 2013.

[93] I.C. Vizitiu, "Some aspects of sidelobe reuction in pulse compression radars using NLFM signal processing," *Progress in Electromagnetics Research C,*, vol. 47, pp. 119-129, 2014.

[94] H.V. Trees, *Detection, estimation, and Modulation Theory*, vol. 1, John Riley & Sons, 2001.

[95] J.F. Hopperstad and S. Holm, "The Co-array of Sparse Arrays with Minimum Sidelobe Level," *Third IEEE Nordic Sognal Processing*, pp. 137-140, 1998.

[96] P.S. Tan, J.M. Stiles and S.D. Blunt, "Optimizing Sparse Allocation for Radar Spectrum Sharing," *IEEE Radar Conference*, pp. 1-6, May 2016.

[97] S.D. Blunt, J. Jakabosky, P. McCormick, P.S. Tan, and J.G. Metcalf, "Holistic Radar Waveform Diversity," *to appear in Academic Press Library in Signal Processing Volume 7 (SIGP): Array, Radar and Communications Engineering, eds. F. Gini, N.D. Sidiropoulos, M. Pesavento*, Elsevier, 2017.

[98] P.S. Tan, J. Jakabosky, J. M. Stiles, and S.D. Blunt, "Higher-order Implementations of Polyphase-Coded FM Radar Waveforms: Relationships between various orders," *to be submitted to IET Radar, Sonar & Navigation (after NRL release approval).*

Appendix A

Notation

A.1 Acronyms

CPM	Continuous Phase Modulation
CRLB	Cramer Rao Lower Bound
ISL	Integrated Sidelobe Level
LFM	Linear Frequency Modulation
LRLA	Low Redundancy Linear Array
MFI	Marginal Fisher Information
MIMO	Multiple-input Mulitple-output
MRLA	Minimum Redundancy Linear Array
MSE	Mean Squared Error
MMSE	Minimum Mean Squared Error

NLFM	Nonlinear Frequency Modulation
OFDM	Orthogonal Frequency-division Multiplexing
PSL	Peak Sidelobe Level
RF	Radio Frequency
SSA	Sparse Spectrum Allocation
ULA	Uniformly-spaced Linear Array
USFA	Uniformly-spaced Frequency Array

A.2 Symbols

BT	Time Bandwidth Product
N	Number of samples for Nyquist frequency sampling
K	Number of samples corresponding to spectrum usage
M	Number of range cells in unambiguous range profile
γ_i	Target scattering coefficient
$\mathbf{H}$	Observation matrix
$\mathbf{J}$	Fisher Information matrix